Flux Crystal Growth, Crystal Structures and Optical Properties of Ga/Ge-Based Oxides and Oxysulfides

A Thesis

Submitted by

Hong YAN

In fulfillment for the award of the degree of

Doctor of Science

Graduate School of Chemical Sciences and Engineering,

Hokkaido University

2022

Abstract

Mixed-anion compounds, which have two or more different anions in a structure, have drawn a considerable attention in the inorganic solid-state science field because the coexistence of the different anionic characteristics such as oxidation numbers, electronegativity, ionic radii, and polarizability can induce unprecedented structures and chemical/physical properties inaccessible in traditional single-anion compounds. However, it is usually very difficult to stabilize mixed-anion compounds by using conventional solid-state reactions, and even if new phases could be obtained, the crystal structures, most of which are complex compared with those of single-anion compounds, could not be solved easily. Flux crystal growth method is a transitional but useful approach to obtain mixed-anion compounds including oxychalcogenide, oxyhalide, and chalcohalide phases. In addition, single crystals grown out of flux can readily allows access to the strcture determination. Although there have been many reports on flux crystal growth of mixed-anion compounds, such examples are very few tcompared with those of single-anion compounds. Therefore, further studies using the flux method are needed to deepen our understanding of mixed-anion compounds.

It is well known that Ga/Ge-based compounds with d^{10} electronic configuration possess wide optical band gaps between the valence band maximum and conduction band minimum, which afford interesting optical properties including photoluminescence, photocatalytic activity, and nonlinear optical responses. Mixing multiple anions in these wide-gap semiconductors can alter the band structure, especially the valence band mamixum composed of anions. Therefore, the anion-directed band gap engineering can be expected to greatly modify the optical properties of the trandisional single-anion compounds. This study has explored new Ga/Ge-based oxysulfide compounds using molten halide salts, resulting in the discoveries of two oxysulfides and an oxide, namely, $La_3Ga_3Ge_2S_3O_{10}$, $La_4(GaS_2O_2)_3$, and $Ce_2CaMg_2Ge_3O_{12}$. The syntheses, crystal structures, and optical properties have been discussed.

Chapter 1 introduces the general background including the mixed-anion and Ga/Ge-based compounds, their structures, and physical properties.

Chapter 2 mainly presents the experimental techniques used in this research.

Chapter 3 illustrates the mixed-anion compound of $La_3Ga_3Ge_2S_3O_{10}$, which crystallized in the hexagonal non-centrosymmetric space group *P*-62*c* with lattice constants of $a = b =$ 10.1406(5) Å and c = 18.1645(9) Å. Non-centrosymmetric chalcogenide-based compounds usually have been exploited as infrared nonlinear optical materials but never been studied for the ultraviolet application due to the high energy level of chalcogen anions leading to band gap narrowing. However, the large polarizability of chalcogenide ions is beneficial to conversion efficiency of second harmonic generation (SHG), and thus mixing chalcogenide ions with the large polarizabilities and oxide ion with short abosorption cutoff edges in a structure can be a useful approach for making chalcogenide-based compunds ultraviolet nonliniear optical materials with strong SHG response. $La_3Ga_3Ge_2S_3O_{10}$ exhibits an exceptionally wide band gap of 4.70 eV, compared with those of early reported oxychalcogenide compounds. This mainly results from the the unique anion-ordered frameworks comprising 1D $^1_\infty[(Ga_{3/5}Ge_{2/5})_3S_3O_3]$ triangular tubes and 0D $(Ga_{3/5}Ge_{2/5})_2O_7$ dimers of corner-sharing $(Ga/Ge)S_2O_2$ and $(Ga/Ge)O_4$ tetrahedra, respectively. SHG measurements revealed that $La_3Ga_3Ge_2S_3O_{10}$ was phase matchable with twice the SHG response of KH_2PO_4 benchmark compund. The results of theoretical calculations suggest that the strong SHG response is mainly attributable to the S-3*p* and O-2*p* orbitals in the occupied states. The anion-directed band-gap engineering may give insights into the application of nonlinear optical oxychalcogenides in the ultraviolet regions.

Chapter 4 presents a new germanium based oxysulfide single crystal $La_4(GeS_2O_2)_3$, which could be obtained by the flux growth method using a $BaCl_2$-$CaCl_2$ eutectic mixture. The crystal structure was determined by the single-crystal X-ray diffraction analysis. $La_4(GeS_2O_2)_3$ crystallizes in the centrosymmetric space group *R*-3 with lattice constants of $a = b =$ 16.8283(3) Å and c = 8.4140(2) Å. The structure of $La_4(GeS_2O_2)_3$ is featured with a complex three-

dimensional anion order and composed of unusual GeS_2O_2 tetrahedra and three types of La-centered polyhedra. The GeS_2O_2 tetrahedra form a triangular arrangement around a columnar structure of alternating face-sharing LaO_{12} and LaS_6O_6 polyhedra. The structure of $La_4(GeS_2O_2)_3$ is like that of the apatite germanate $La_{9.33}(GeO_4)_6O_2$, which features face-sharing LaO_9 columns surrounded by GeO_4 tetrahedra. The combination of UV−vis absorption measurements and first-principles calculations revealed the existence of an indirect optical band gap (Eg = 3.67 eV) between the valence band maximum composed of S 3*p* orbitals and the conduction band minimum composed of La-3*d*, La-4*f*, S-3*p*, and Ge-4*s* orbitals.

Chapter 5 shows a new germanate garnet single crystal $Ce_2CaMg_2Ge_3O_{12}$, which was synthesized via flux growth method using a $BaCl_2$-$CaCl_2$ eutectic mixture. The initial target phase was a Ge-based oxysulfide with Ce atoms, but the new garnet phase was obtained by reaction with a MgO crucible. Single-crystal X-ray diffraction analysis revealed that $Ce_2CaMg_2Ge_3O_{12}$ crystallized in a cubic garnet-type structure with lattice parameters of a = 12.5487(3) Å in the space group *Ia*-3*d*. The chemical formula can be expressed as the common garnet formula of $A_3B_2C_3O_{12}$, where Ce/Ca, Mg, and Ge occupy the A, B, and C sites, respectively. A UV–Vis spectroscopy measurement on the germanate garnet exhibited a clear absorption edge corresponding to a band gap of 2.21 eV (λ = 561 nm). First-principles calculations indicated that the valence band maximum was composed of Ce 4*f* bands, whereas the conduction band minimum mainly consisted of Ce 5*d* bands. These findings explain the observed absorption edge through the Ce 4*f* to 5*d* absorption. Photoluminescence emission spectra exhibited a very broad peak centered at 600 nm, corresponding to transition from the lowest energy *d* level to the 4*f* levels.

Chapter 6 presents the general conclusion and future prospects based on this work.

Keywords: Mixed-anion, Ga/Ga-based compound, Flux growth method, Optical property.

List of Abbreviations

NLO	Non-linear optics
SHG	Second harmonic generation
XRPD	X-ray powder diffraction
SXRD	Synchrotron X-ray diffraction
BVS	Bond valance sum
VBM	Valence band maximum
CBM	Conduction band minimum
NIMS	National Institute for Materials Science
E_g	Energy gap
HSAB	Hard-Soft-Acid-Base theory
PL	Photoluminescence
PLE	Photoluminescence excitation
UV-Vis-NIR	Ultraviolet-visible-Near Infrared
TG	Thermal Gravimetric
DFT	Density functional theory

Flux Crystal Growth, Crystal Structures and Optical Properties of Ga/Ge-Based Oxide and Oxysulfides

Contents

Chapter 1. Introduction

1.1. Mixed-anion compounds

Mixed-anion compounds are groups of functional solid-state materials with a variety of new characteristics that has been under explored. They contain more than one kind of anionic species, providing interesting basic functions for seeking new materials.[1-4] When looking at the local structure of mixed-anion compounds, it is easy to find the bonding of metallic cationic center with more than one anionic ligand forming heteroleptic coordination geometry, which is the main diffenernce from single anionic species. Different anionic properties, such as charge, ionic radius, electronegativity and polarizability, [5-6] may add a new dimension to the control and adjustment of the electronic and atomic structure of materials, which may support phenomena that cannot be achieved by single anion.

This anionic directed research is still in the early stage, where there is much untapped space and brings new opportunities and chanllenges in material science. The main target in the literature part of this thesis is to summarize mixed-anion compound groups, compare the physical and chemical properties of similar compounds and variations across groups.

1.2. Classes and subgroups

This thesis focuses on mixed-anion compouds which contains oxygen and one type of another anionic species. These can be further devided into subgroups which the names are derived from the latter anionic species besides oxygen. For example, oxysulfide is a subgroup of oxychalcogenide.

1.2.1. Oxychalcogenides

Oxychalcogenides consist of both oxygen and at least one chalcogen anions from group 16 (S, Se, and Te). Oxysulfides are the main points of this thesis. Oxychalcogenides have a wide range of conductive properties from nearly insulator to metallic conduction. Zn-based oxysulfides exhibit excellent ionic conductivity with carrier mobility as high as 40 $cm^2V^{-1}s^{-1}$.[7] The alteration of distinct layers in oxysulfides result in the tunability of conductivity. Oxychalcogenides exhibit a wide optical transparent window from deep ultra-violet (DUV) to mid-infrared regions.[8] The high conduction band offset offers the possibility of tunable band gap, which is impossible for single anionic species. The low-dimensionality structure with ionic and covalent bonding also promotes the applications in thermoelectric fields.[9,10]

1.2.1.1 Oxysulfide

Oxysulfides are rare in nature due to the unstability of sulfides toward oxidation. The most reported oxysulfides are synthetic. The competition between sulfide and sulfate should be also concerned for designing the synthetic route.

To the best of our knowledge, the first oxysulfide was $Ce_xO_yS_z$ reported by Mosander in 1827 as the production of the sulfidation of Ce_2O_3 to Ce_2S_3. The first crystalline oxysulfide was La_2O_2S by Pitha et al. in 1947. Since this discovery, the series of Ln_2O_2S (Ln = lanthanide elements) was developed. [11-13] Later, a lot of quaternary oxysulfides consisting of lanthanides and transition metal elements were synthesized. These compounds, in which oxygen atoms are always connected only to the lanthanide and sulfur only coordinated with the transition metal elements, exhibit a special selective bonding manner. This selective bonding can be explained by the HSAB rule, because sulfur anions are thought to be more polarizable than oxygen anions, which results in different anionic ordering. The lamellar preformed structures by the selective bonding can be extended to any oxysulfides if one of the anions prefers to bind to one of the

metal elements and vice versa. However, if no such order is present in the structure, the oxysulfides will exhibit unselective bonding manner. In order to illustrate the difference between selective/unselective bonding, we use quaternary oxysulfides of $Ln_2Ti_2S_2O_5$ and $La_4Ti_3O_8S_4$ as examples.[14,15] $Ln_2Ti_2S_2O_5$ crystallizes in Ruddlesden-Popper structure containing $[Ln_2S_2]^{2+}$ and $[Ti_2O_5]^{2-}$ layers in selective bonding manner, while $La_4Ti_3O_8S_4$ doesn't show any selective bonding, leading to heteroleptic coordination environment around the metal atoms. Another example is the La-Ga-based oxysulfides, in which $La_{3.33}Ga_6O_2S_{12}$ is in selective bonding manner as well La_3GaOS_5 is in unselective bonding manner.[16,17] The comparisons of strucutres of the above oxysulfides are shown in Figure 1.1. Quinary oxysulfides also exist, and most of them have layered structure with selective bonding manner. The reported oxysulfides are summarized in Table 1.1. Because of the low toxicity and earth-abundant elements, oxysulfides have become promising materials with multifunctional properties.

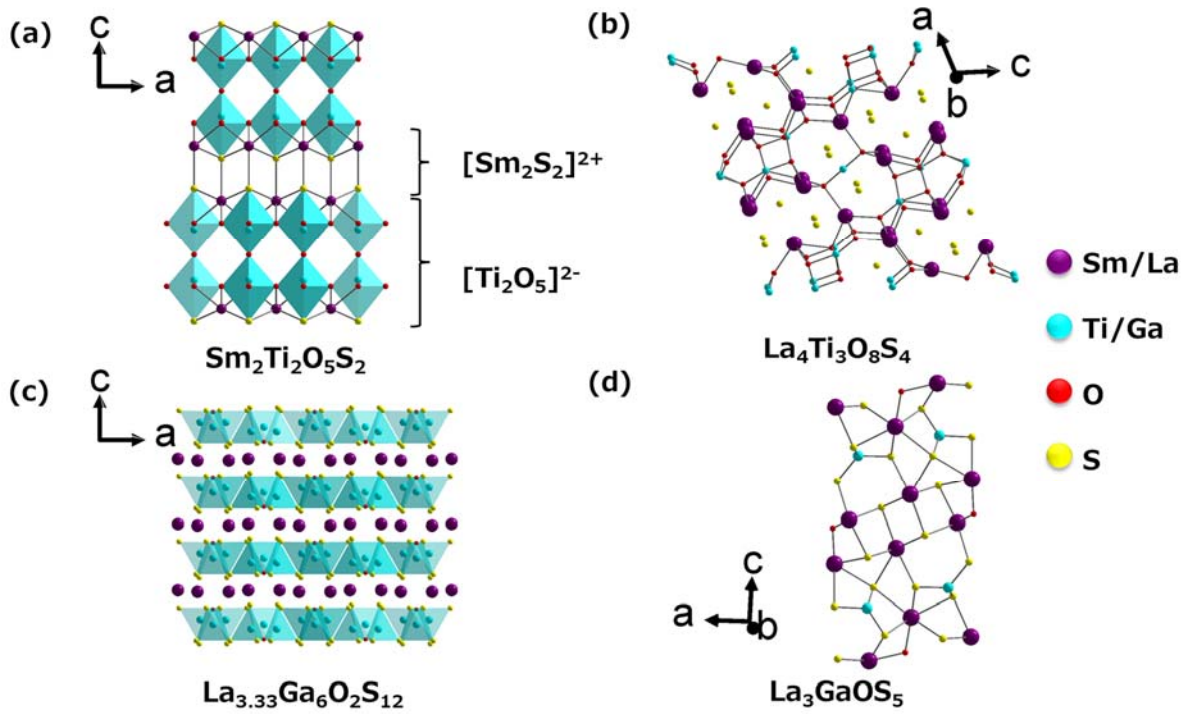

Figure 1.1. Various oxysulfides structures. (a) $Sm_2Ti_2O_5S_2$ and (c) $La_{3.33}Ga_6O_2S_{12}$ exhibit selective bonding, while (b) $La_4Ti_3O_8S_4$ and (d) La_3GaOS_5 show different unselective bonding.

Table 1.1. Some oxysulfides and their structure.

Chemical formula	Space group	Ref.	Chemical formula	Space group	Ref.
$Ln_2Ti_2O_5S_2$ (Ln = Pr, Nd, Sm)	*I*4/*mmm*	14	$LaGaOS_2\alpha$	$P2_1ab$	38
$La_4Ti_3O_8S_4$	*C*2/*m*	15	$LaGaOS_2\beta$	*Pmca*	39
$La_6Ti_2O_5S_8$	$P2_1/m$	15	La_3GaS_5O	*Pnma*	17
$La_{14}Ti_8O_4S_{33}$	*C*2/*m*	18	$La_{3.33}Ga_6S_{12}O_2$	$P42_1m$	16
$La_8Ti_{10}O_4S_{24}$	*P*4/*mmm*	19	$Ce_4Ga_2O_4S_5$	*I*4/*mmm*	40
$La_{20}Ti_{11}O_6S_{44}$	*Pmmn*	20	$Ln_4Ga_{1.33}O_4S_4$ (Ln = La, Ce)	*P*4/*mmm*	38
$Nd_{16}Ti_5O_{17}S_{17}$	*I*4/*m*	21	$Ln_4Ga_2O_4S_5$ (Ln = Pr, Nd, Sm)	*Pbca*	41
$Ln_5V_3O_7S_6$ (Ln = La, Ce, Pr, Nd)	*Pmnm*	22	$La_5In_3O_3S_9$	*Pbcm*	42
$LaCrOS_2$	*Pbnm*	23	$La_{10}In_6O_6S_{17}$	*Immm*	43
$LnCrOS_2$ (Ln =Ce, Pr, Nd, Sm)	*B*2/*m*	24	$Ln_4Sn_2O_4S_6$ (Ln = La, Ce, Pr, Nd)	*Pbnm*	41
La_4MnOS_6	$P6_3mc$	25	$Ln_4Ge_{1.5}O_4S_5$ (Ln = La, Ce, Pr, Nd)	*Pbca*	41

$Ln_2Fe_2O_3S_2$ (Ln = La, Ce, Pr)	*I*4/*mmm*	26	$La_4As_2O_4S_5$	*I*4/*mmm*	40
LnCuOS (Ln =La, Pr, Nd, Sm)	*P*4/*nmm*	27	$La_6Sb_4O_{12}S_3$	$I4_1/amd$	44
$La_5Cu_6O_4S_7$	*Imma*	28	$NdSbOS_2$	*P*4/*nmm*	45
BiCuOS	*P*4/*nmm*	29	$CaSb_{10}O_{10}S_6$	*C*2/*c*	46
$La_2Nb_3O_8S_2$	*Pnnm*	30	CaCoOS	$P6_3mc$	47
$La_3MO_5S_2$ (M = Nb, Ta)	*I*4/*mmm*	31	BaCoOS	*Cmcm*	47
$Ce_3NbO_4S_3$	*Pbam*	32	CaZnOS	$P6_3mc$	48
$Ln_3NbO_4S_3$ (Ln = Sm, Gd)	$Pn2_1a$	33, 34	BaZnOS	*Cmcm*	49
$Ln_2Ta_3O_8S_2$ (Ln = La, Sm)	*Pnnm*	35, 36	$SrZn_2OS_2$	$Pmn2_1$	50
LaAgOS	*P*4/*nmm*	37	$Sr_6Cd_2Sb_6S_{10}O_7$	*Cm*	51

Optical properties. Many oxides have wide band gaps and transparent optical windows. Non-oxygen anions with lower electronegativity against oxygen in semiconductors will raise the valence-band maximum (VBM) and narrow the band gap, affording the applications from DUV to mid-infrared regions. When less electronegativity chalcogenide

anions (S, Se, Te) substitute the oxygen anions, the non-oxygen *p* orbitals with high energy push the valence band to conduction band and allow for the visible-light or infrared absorption.

This strategy is of particular significance for seeking novel photocatalyst which can split water under solar irradiation. One limitation of oxides with a narrow band gap (<3 eV) is that, the conduction band minimum (CBM) will become more positive than the water reduction potential. In order to overcome this problem, various oxysulfides have been designed and shown water splitting performance. La-Ga-based oxysulfides $LaGaS_2O$ and La_3GaS_5O were characterized as photocatalysts for water oxidation and reduction.[52] La_3GaS_5O exhibited to split water under visible irradiation ($\lambda > 420$ nm), while $LaGaS_2O$ produced photocurrent under ultraviolet light ($\lambda > 290$ nm), because La_3GaS_5O has a higher VBM than $LaGaS_2O$. $Y_2Ti_2O_5S_2$ with narrow bang gap (E_g = 1.9 eV) achieved the overall water-splitting reaction under solar irradiation, which extends the range of promising materials for solar energy conversion.[53]

Metal oxysulfides are also investigated for non-linear optical (NLO) materials due to the wide transparency and large NLO efficiency. For single anion metal sulfides, their second harmonic generation (SHG) coefficiency and birefringence are usually significantly higher than single metal oxides, while the band gap and laser damage threshold (LDT) are lower than those of oxides. Recently, metal oxysulfides are reported to be promising NLO materials, which high SHG property, fine tunable band gap, good birefringence and LDT can be stabilized in one structure. $SrZn_2S_2O$ exhibits twice of SHG coefficiency to that of benchmark potassium dihydrogen phosphate (KDP) in the phase-matchable manner. $Sr_6Cd_2Sb_6S_{10}O_7$ shows strong SHG response of 4 times of benchmark $AgGaS_2$ in the infrared region with SHG active building block units SbS_4O pyramids in the structure. Although strong SHG properties have been detected in these oxysulfides, their band gaps are narrower than 4.0 eV, which limits the applications in the UV regions. Therefore, It is still a great challenge to push the opto-transparent window of the oxysulfide phase to the fourth or sixth harmonic generation

wavelength of the Nd:YAG laser while maintaining a high SHG coefficient and appropriate birefringence. In this thesis, we report a new UV NLO oxysulfide $La_3Ga_3Ge_2S_3O_{10}$, which exhibits an exceptionally wide band gap (E_g = 4.70 eV) and a phase-matchable SHG response of twice KDP.

Superconductivity. Studies of superconductivity in oxysulfides have been conducted in the past decades. The superconducting performance comes from the layered structure as the electron carrier transportation path.[54] The discovery of LaOFeAs superconductor with FeAs layers provides the guidelines in seeking new oxysulfide materials with similar layered structure. With the utilization of high-pressure synthesis and substituting non-magnetic elements with magnetic species, more and more oxysulfides with excellent superconductivity performance have benn reported.

One bulk superconductor is a ternary oxysulfide $Bi_4O_4S_3$, which exhibits T_c = 4.4 K under magnetization measuremnets. The structure of $Bi_4O_4S_3$ consists of alternatin layers of Bi_2O_2, Bi_2S_2, and SO_4. The BiS_2 layers are regarded as the induction of superconductivity by the hybridization of Bi-6*p* and S-3*p* orbitals.[55] Another example is the oxysulfide $LnOBiS_2$ (Ln = La, Ce, Pr, Nd) featuring from the BiS_2 double layers stacked with a blocking LnO layer. The superconducting property can be enhanced by cationic or anionic substitution accompanied with phase transition from monoclinic to tetragonal.

Electrochemistry. The electromechimal performance of oxysulfides have been discussed due to the redox reactions with transition metals. $Li_xTiO_yS_z$ thin film was studied as cathodes in solid-state lithium-ion battery.[56] For anode applications, TiO_2@MoO_yS_z composite was reported.[57] The hybridation of molybdenum oxysulfide was supposed to improve the electronic conductivivity of the hybrid material.

1.2.1.2 Oxyselenides & oxytellurides

Similar to oxysulfides, oxyselenides also exhibit interesting properties. These include layered structure and the possibility of preparing rare cationic coordination environments, offen with low oxidation states. A large amount ox oxyselenides have similar structures to the superconducting chalcogenides. A typical case is oxyselenide superconductor $LaOBiSe_2$, which T_c = 2.6 K has been reported.[58]

The synthesis of oxyselenides must also be more carefully, especially in ambient atmosphere. In the synthesis, we should avoid the oxidation of selenium and selenide to higher oxidation state. In addition, selenium is toxic and will volatize above 685 °C, therefore, low heating rate and low temperature stay should be used to protect the reaction tubes or chambers.

The most investigated oxyselenides is BiOCuSe, which crystallizes in alternative conductive $(Cu_2Se_2)^{2-}$ and insulating $(Bi_2O_2)^{2+}$ layered structure along the *c* axis, as shown in Figure 1.2.[59,60] Therefore, the high carrier mobility along the *a*-*b* plane is expected due to the anisotropy. Due to the low thermal conductivity of oxyselenides, BiOCuSe has a much greater thermoelectric value (ZT) than other oxides. The thermoelectric property can be futher enhanced by the hole doping with Ba, because the electrical transport property is improved.

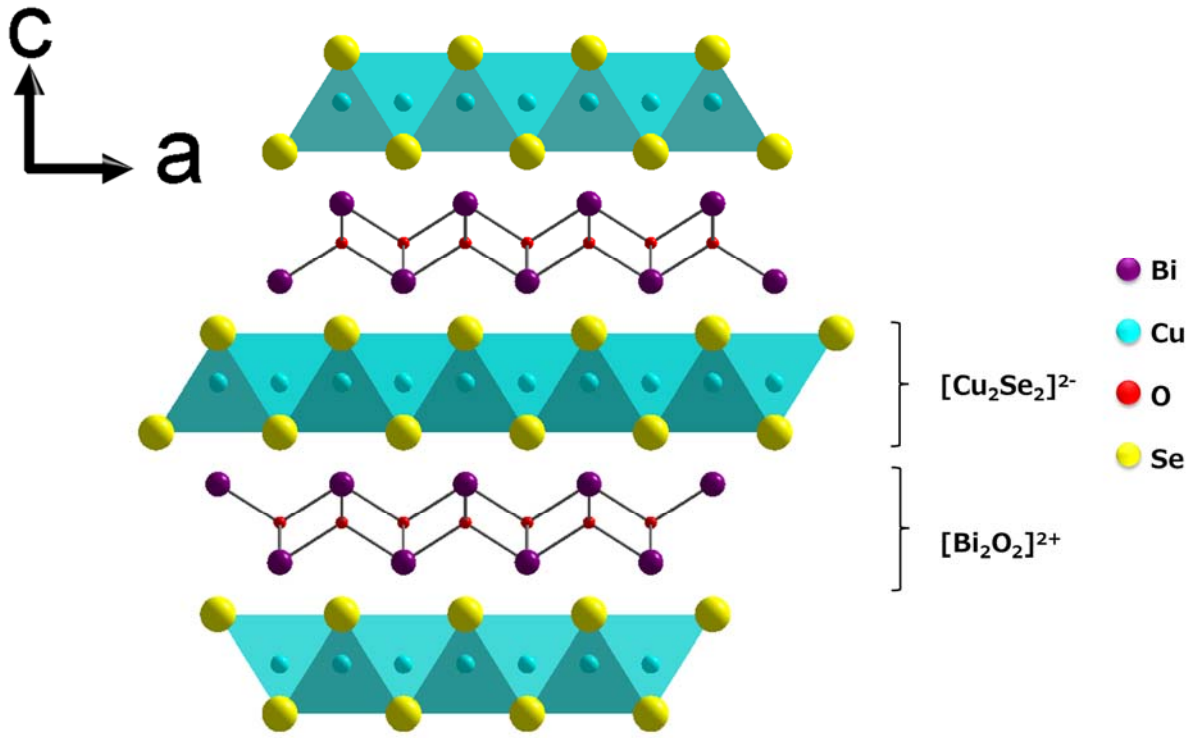

Figure 1.2. Crystal structure of BiOCuSe, which shows alternative conductive $(Cu_2Se_2)^{2-}$ and insulating $(Bi_2O_2)^{2+}$ layers.

The optical band gap for Bi-based oxyselenides varies from 0.8 to 2.0 eV.[61] The band gap engineering can be achieved by Se substitution with S, which the optical band gap increases to 2.8 to 3.1 eV for $BiOCuS_{1-x}Se_x$.[62] The study of first-principles calculation indicates that $[Cu_2Se_2]^{2-}$ with the antibonding states affects most to the band gap. The results show that the insulating layer $[La_2O_2]^{2+}$ restricts the hole carriers to the $[Cu_2Se_2]^{2-}$ layer, resulting in significant two-dimensional characteristics. This band gap engineering feature makes oxychalcogenides promising candidates for the applications of p-type semiconductors.

The physical properties of oxyselenides can also be enhanced by doping. Ba and Na substitution have been reported to improve BiOCuSe carrier concentration significantly.[63] The ferromagnetic-antiferromagnetic transition temperature for $Sr_4Mn_3O_{7.5}$ can be tuned by the F or O de-intercalation.[64] The selected oxyselenides and the properties are listed in Table 1.2.

Table 1.2. Some oxyselenidesand and their properties.

Chemical formula	Conductivity [σ] (S/cm)	Optical band gap [E_g] (eV)	Ref.
CaOFeSe	$6.6*10^{-5}$	1.8	65
$LaOCuS_{1-x}Se_x$	/	2.8-3.1	60
$La_2O_2CdSe_2$	Very small	3.3	66
Bi_2O_2Se	/	1.4	67
BiOCuSe	1.12	0.8	68
$Bi_{1-x}La_xOCuSe$	10-60	0.2-1.2	69
$Bi_{1-x}Mg_xOCuSe$	32	0.9	70

Oxytellurides exhibit similar behaviors as oxyselenides in electrical and thermoelectric properties. The Te substitution of Se in BiOCuCh results in increased electrical conductivity and decreased thermal conductivity. Therefore, BiOCuTe exhibits improved thermoelectric property than BiOCuSe. Bi_2O_2Te also shows attractive thermal conductivity (0.91 $Wm^{-1}K^{-1}$).[71] The research of oxytellurides is not well investigated as oxyselenides and still going on.

1.2.2. Oxynitrides & Oxypnictides

Oxynitrides are a relatively new class of functional materials, which may exhibit the features of both oxides and nitrides. Oxynitrides have been reported as insulators or semiconductors, because they show the properties of carrier concentrations of 10^{13} – 10^{23} cm^{-3} and Hall mobilities of up to 200 $cm^2V^{-1}s^{-1}$.[72,73] Interesting applications of oxynitrides includes oxynitrides glasses, thin films, and photocatalysts. High corrosion resistance, electrical conductivity, elastic modulus, and tenacity after the combination of oxides and nitrides make oxynitrides appealing to researchers.[74,75]

Oxynitrides are of great interest in the filed of photocatalystic processes because of their narrow band gap leading to activity in the visible light-driven water splitting for hydrogen and oxygen evolution. Common oxynitrides contains metals such as Ti, Nb, Zr, Ga, and Ta. The typical example is d^0-type TaON-based oxynitride photocatalysts. TaON was reported to photocatalytically evolve H_2 and O_2 from aqueous solutions because of the suitable bandgap and corrosion stability up to 510 nm visible light region. The structure of TaON crystalizes in monoclinic phase with Ta hepta-coordinated with O and N anions, as shown in Figure 1.3. The available wavelength was expanded to 600 nm by using a solid solution of $LaTaON_2$ and $LaMg_{2/3}Ta_{1/3}O_3$ forming the $LaMg_{1/3}Ta_{2/3}O_2N$ oxynitride perovskite.[76]

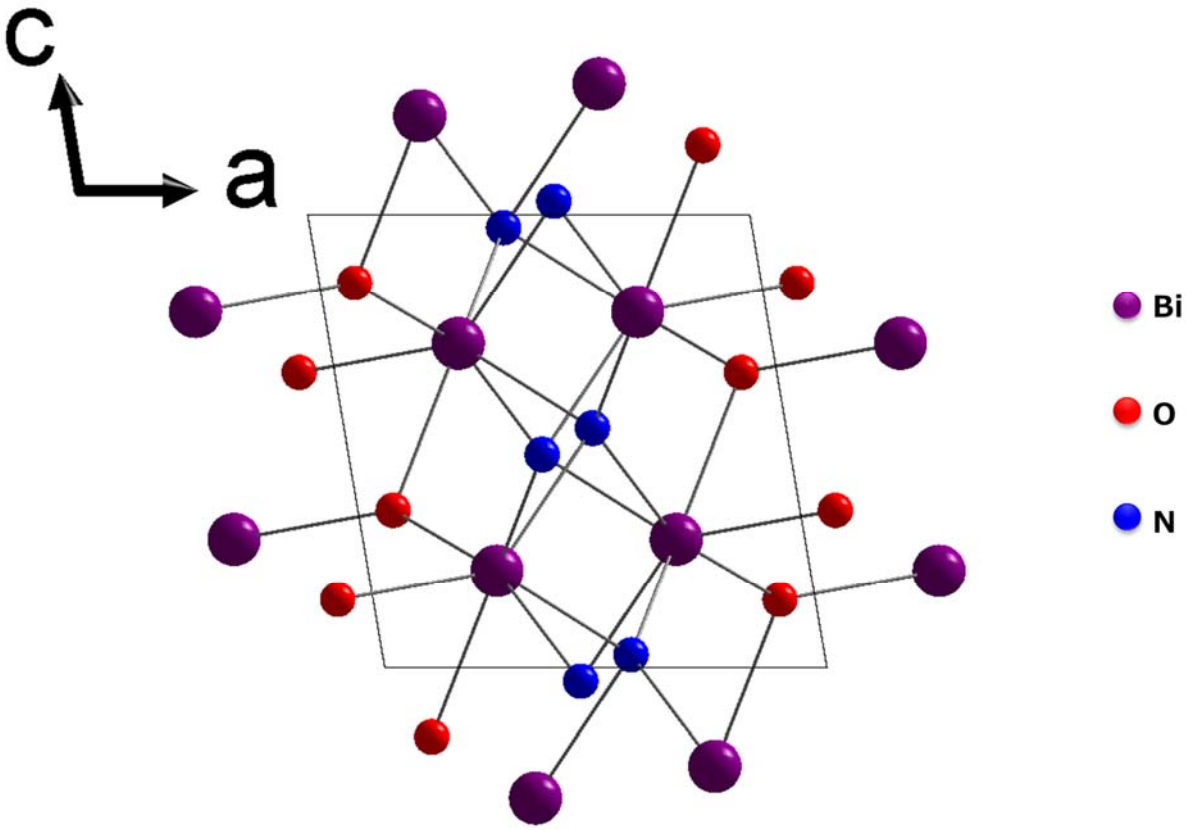

Figure 1.3. Crystal structure of TaON viewing from *b* axis. Ta atoms are hepta-coordinated with O and N atoms.

Oxytrides also exhibit other interesting performance. Lithium phosphorus oxynitride LiPON exhibits high ionic conductivity and is utilized as electrolyte for Li-ion battery.[77]

$EuNbO_2N$ and $EuWON_2$ have perovskite structures and have been reported as ferromagnetic materials.[78,79] The oxynitrides and their properties are summarized in Table 1.3.

Table 1.3. Some oxynitrides and their properties.

Chemical formula	Conductivity [σ] (S/cm)	Optical band gap [E_g] (eV)	Ref.
LiOPN	$3.8*10^{-10}$ – $1.67*10^{-6}$	/	77
$CaTaO_2N$	/	2.43	80
SiO_xN_y:H	$4.5*10^{-3}$	2.3	81
ZnON	0.1	3.2	82
ZnSnON	$2.3*10^{-6}$	3.2	75
$REHfO_2N$ (RE = La, Nd, Sm)	$1.0*10^{-10}$	3.4	83
$LaTiO_2N$	/	2.1	84

Oxypnictides consists of both oxygen and heavier pnictogen (P, As, and Sb) anions. Over 300 oxypnictides have been reported. The synthesis of bulk oxypnictides usually requires extreme conditions under high temperature or high pressure. The typical structural feature of oxypnictides is the alternating layers. Polyatomic anions pnictates are always formed as the results of the coexistence of both oxygen and pnictogen, such as phosphates, arsenates, and antimonates (PnO_4^{3-}, Pn = P, As, and Sb). The structre-property relationships of layered d-metal oxynitrides have been investigated by the inter- and intra- layers in the structure, which selects cations for interlayers and pnictide ions for intralayers. Most usual structures of oxypnictides include fluorite, or antifluorite type layered structures, as shown in Figure 1.4 of two typical oxypnictide structures and common crystallographic sites for species to occupy.

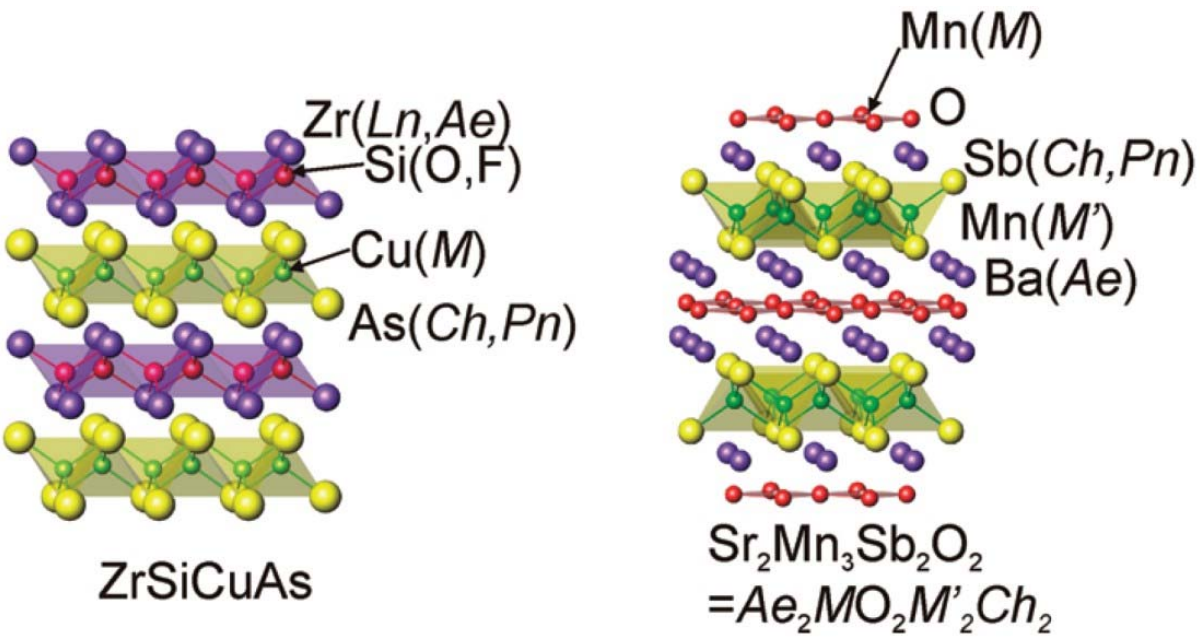

Figure 1.4. Oxypnictide ZrSiCuAs (left) and $Sr_2Mn_3Sb_2O_2$ (right) structures, which show crystallographic sites for species to occupy.[85]

The oxide and pnictide layers in oxypnictides are quite different electronically in terms of their electronic properties. The difference depends on the cationic size in the structure, which is due to the different distances between the metal and the pnictogen atoms. Therefore, the pnictide anions may be more or less involved in bongding with metals.

Oxypnictides have similar layered structure to that of oxysulfides, examples are two mixed-anion compounds LaOCuCh (Ch = chalcogen) and LaOTMPn (TM = divalent transition metal, Pn = pnictogen). La^{3+} and Cu^{+}/TM^{2+} indicate that lanthanum layer has more positive charge than copper or divalent TM layer. The CuCh and TMPn layer between the oxide layers are regareded as transportation path for hole carriers. The formations of LaO, CuCh, and TMPn layers can be explained by the Hard-Soft-Acid-Base (HSAB) theory. According to HSAB theory, hard acid (La) is inclined to connected with hard base (O), while soft acid (Cu, TM) tends to be coordinated with soft base (Ch, Pn). LaOFeP and LaONiP are isostructural to the above phase and exhibit superconductivity.[86] Oxypnictides also have promising performance, such as electric, ferromagnetic, ferroelectric properties, as the relative oxychalcogenides.

Doping and substitution have been induced for higher superconducting temperatures, for example, $BaOTi_2Sb_2$ increased the superconducting transition temperature by Na substitution. SmOFeAs has been reported to exhibit T_c = 55 k after fluorine doping, which is one of the highest superconducting transition temperatures. A selection of oxypnictides and their physical performance is listed in Table 1.4.

Table 1.4. Some oxypnictides and their properties.

Chemical formula	Conductivity [σ] (S/cm)	[T_c] (K)	Ref.
$Ba_2Ti_2Cr_2OAs_4$	2.3	/	87
GdFeAsO	~1.0	53.5	88
$LaFeO_{1-x}F_xAs$	0-3.33	43	87
LaNiOP	0.83	3	89
LaNiOAs	0.29	2.4	90

1.2.3. Oxyhalides

Oxyhalides are mixed-anion compounds consisting of oxygen and one or more halogen atoms (F, Cl, Br, I). Most metal elements have been reported to form oxyhalides except alkali metals. Some of the oxyhalides even include nitrogen, phophorus, and sulfur forming more complicated heteroleptic coordination environment.

Oxyhalides have attracted more and more attention in various research fields, including photocatalyst, optoelectronicity, and electrochemistry. Oxyfluorides are an emerging group of high-capacity cathode materials. The cathode cyclability can be significantly enhanced by oxygen substitution in pure halides. Complex electrochemical reactions can be attributed to the

cycling in mixed-anion compounds, whose electrochemical performance are improved by substitution. For instance, FeO_xF_{2-x} exhibits improved electrical conductivity than the FeO or FeF_2 due to the higher oxidation state of Fe.[91] Oxyfluorides also act act as fluorinating agents, which reacts strongly with water and phosphorus, such as $SeOF_2$.

Especially, bismuth oxyhalides (BiOX, X = Cl, Br, and I) have been studied comprehensively.[92] The crystal structure of BiOX consists of slabs of [X-Bi-O-Bi-X] layers combined via van der Waals forces, which form a tetragonal matlockite crystal structure, as depicted in Figure 1.5. Each bismuth atom is surrounded by four oxygen atoms and four halogen atoms in a decahedral coordination environment. Excellent properties, such as optical and electric, are generated from the synergistic effect of van der Waals interaction among the atomic layers and covalent bonding among the cation and surrounded anions.

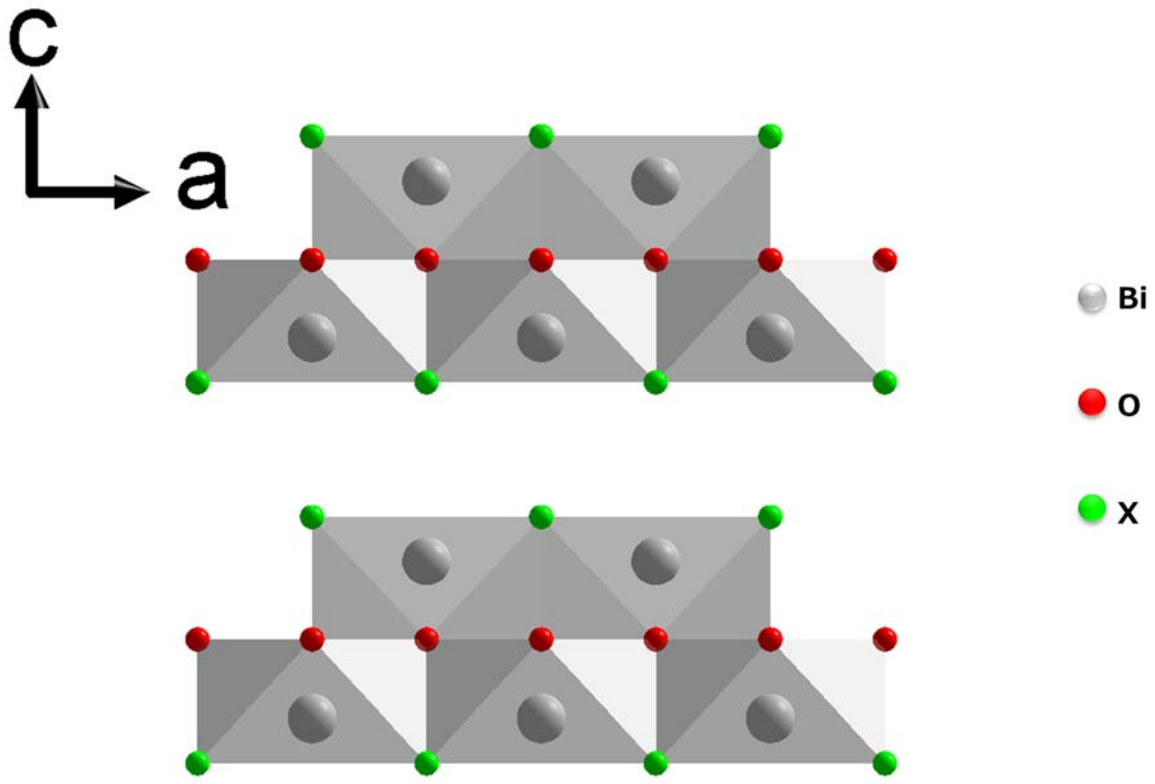

Figure 1.5. Crystal system of BiOX (X = F, Cl, Br, I) with slabs of [X-Bi-O-Bi-X] layers

stacked along the *c* axis.

The examples of oxyhalide compounds and their properties are listed in Table 1.5.

Table 1.5. Some oxyhalides and their properties.

Chemical formula	Conductivity [σ] (S/cm)	Optical band gap [E_g] (eV)	Ref.
$Sr_2RuO_3F_2$	0.024	/	93
$SrFeO_{3-x}F_x$	/	2.4	94
$NdNiO_{3-x}F_x$	0.0001	2.1	95
BiOX (X = Cl, Br, I)		BiOCl: 3.4 BiOBr: 2.8 BiOI: 1.8	92

1.3. d^{10} transition metal elements

Benefiting from the high optical performances, metal oxychalcogenides with d^{10} transition metal are highly promising materials for NLO, photocatalysis, and photoluminescence. D^{10} transition cations (In^{3+}, Ga^{3+}, Ge^{4+}, Sn^{4+}…) are preferential options for designing novel functional materials due to the heteroleptic or homoleptic coordination environment around the metal center, which is regarded as the functional building block units for those oxychalcogenides. The optical properties of typical d^{10} transition metal oxychalcogenides or oxides are stated in this part based on the local coordination structures and the band structures.

1.3.1. Effects of coordination structures

Alkaline earth metal and gallium-based oxides MGa_2O_4 (M = Mg, Sr, Ba) exhibit different photocatalytic activity for water splitting under UV irradiation, in which $MgGa_2O_4$ has negligible photocatalytic property but $SrGa_2O_4$ and $BaGa_2O_4$ show remarkable evolution

of H_2 and O_2 from water splitting. The differences in the crystal structures result in the photocatalytic activity. $MgGa_2O_4$ crystalizes in cubic structure and contains GaO_6 octahedra, which is nearly free from the distortion around Ga^{3+} cation and the dipole moment is 0. $SrGa_2O_4$ and $BaGa_2O_4$ have monoclinic and hexagonal structures, and both consist of GaO_4 tetrahedra as the photocatalytic fundamental units. The distorted GaO_4 tetrahedra have large dipole moments (0.80, 1.2, and 1.2 D for $SrGa_2O_4$, 1.70, 1.11, and 2.58 for $BaGa_2O_4$). The comparison between structures, photocatalytic properties and dipole of MGa_2O_4 is shown in Figure 1.6. It is noteworthy that distorted MGa_2O_4 (M = Sr, Ba) with a dipole moment has photocatalytic activity, while the activity of $MgGa_2O_4$ without distortion is negligible.[96-98]

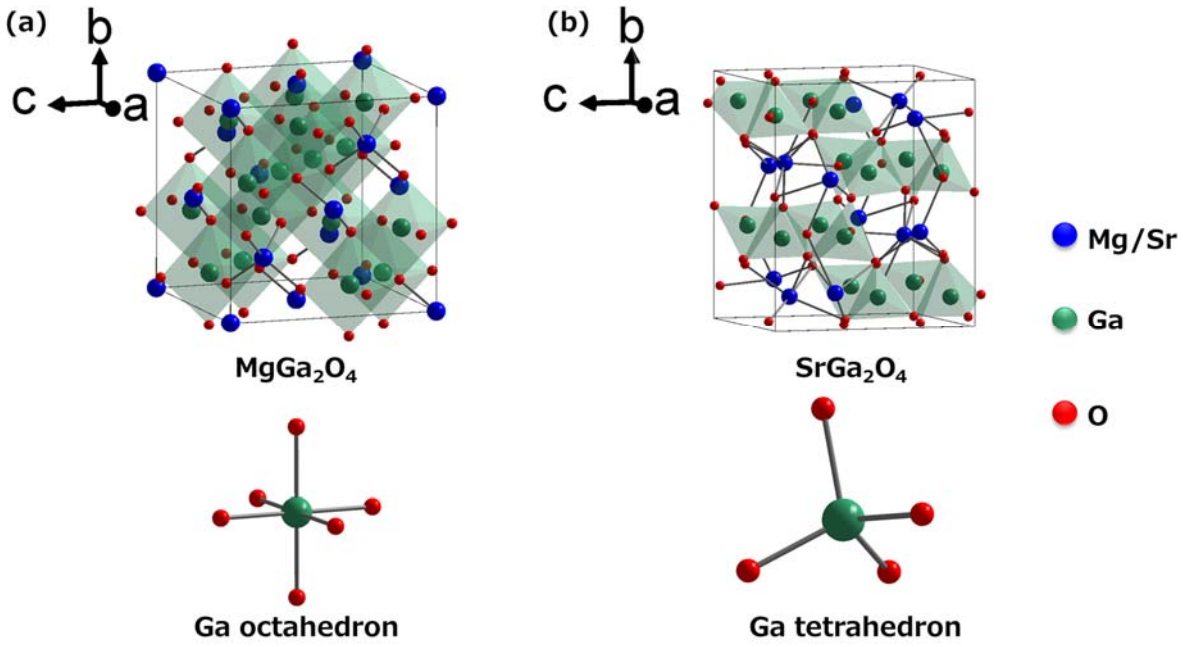

Figure 1.6. Crystal structures of MGa_2O_4 (a: M = Mg, b: M = Sr) and the geometry of involved octahedral GaO_6 and tetrahedral GaO_4.

Highly polarizable mixed-anion structural building block units have been reported as prospective candicates for optical materials with high performance. The isovalent substitution of O atoms by chalcogen atoms in the $[TMQ_4]$ (TM = transition metal, Q = O or chalcogen atoms) tetrahedra can form heteroleptic coordination environment, therefore influence the crystal structure and optical property. Two Sr-Ge-based quaternary oxychalcogenides

$Sr_3Ge_2O_4Se_3$ and $SrGe_2O_3S_2$ contain [GeQ_4] tetrahedra but have different crystal structures.[99] $Sr_3Ge_2O_4Se_3$ crystallizes in non-centrosymmetric spece group *R*3*m* consisting of highly distorted [$GeOSe_3$] and [GeO_4] tetrahedra. It exhibits SHG intensity (0.8 times of $AgGaS_2$) at infrared region (E_g = 2.96 eV). $SrGe_2O_3S_2$ crystallizes in centrosymmetric space group $P2_1/c$ with [GeO_3S] tetrahedra in the structure. It shows large birefringence (calculated Δn = 0.22 - 0.17 from 0.4 to 4.0 μm). The optical properties should be attributed to the arrangement of dipole moments of these structural functional building block units. The SHG intensities of Ba/Sr-Ge base oxychalcogenides are consistent with the results of those dipole moments.

1.3.2. Effects of electronic structures

MGa_2O_4 (M = Mg, Sr) shows different electronic structures via the first-principles calculation. The valence band of $MgGa_2O_4$ contains O-2*p* orbitals, while the conduction band consists of Ga-4*s* and Ga-4*p* orbitals. Mg orbitals make no contribution to the valence and conduction bands, and the calculation gives the band gap of 2.56 eV. For $SrGa_2O_4$, similar electronic configuration is observed in valence band, while Sr-4*s*, Sr-4*p*, and Ga-3*d* orbitals dominate the conduction band. The calculated band gap is 2.97 eV. The energy band diagram and density of state (DOS) is shown in Figure 1.7. The result indicates the influence of geometric environment of d^{10} cation on the electronic structures.

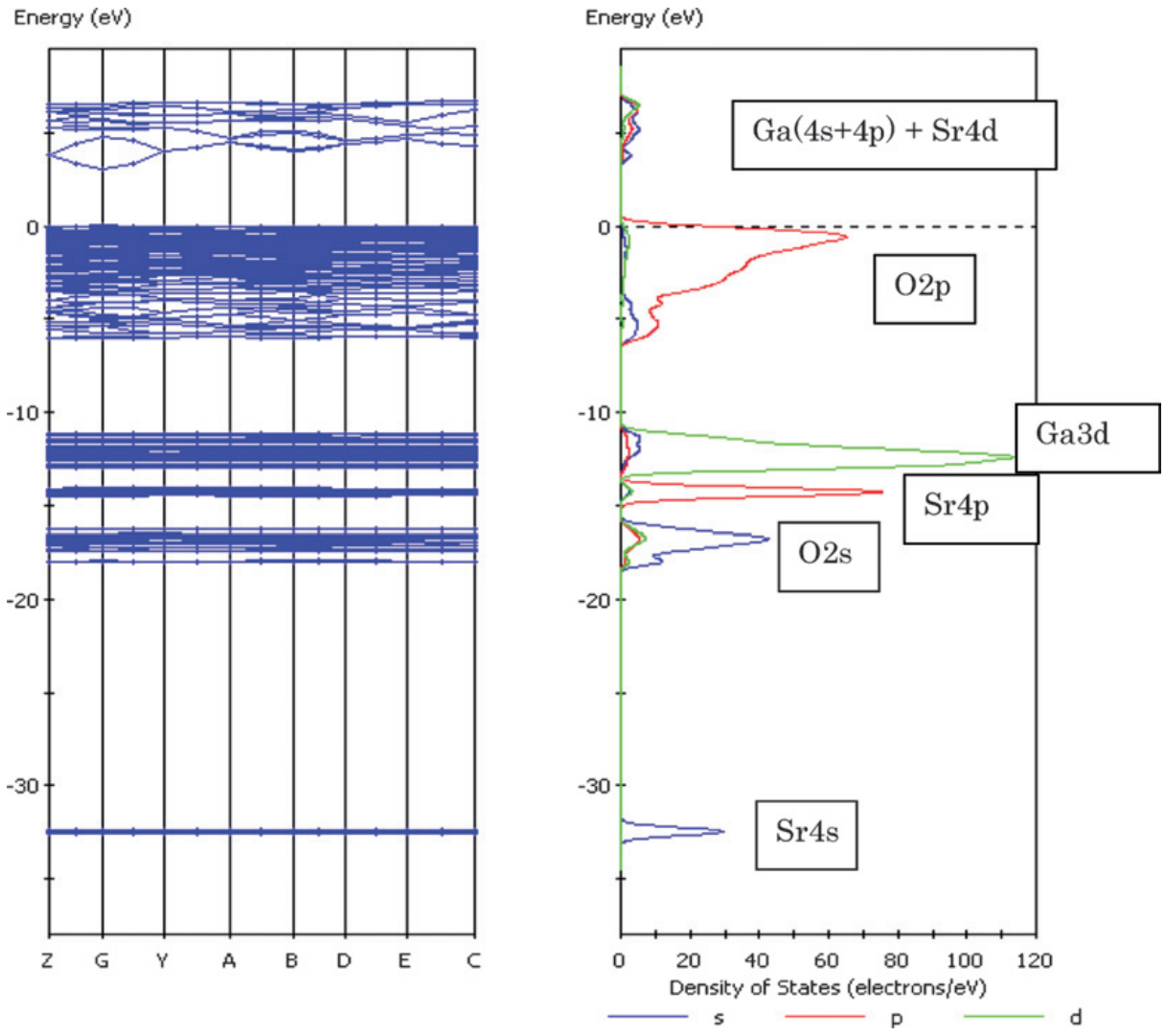

Figure 1.7. Energy band diagram and DOS of $SrGa_2O_4$.

In the d^{10} oxychalcogenides with heteroleptic coordinations, more complicated hybridized orbitals can be observed. The electronic band structure of $Sr_3Ge_2O_4Se_3$ and $SrGe_2O_3S_2$ is displayed in Figure 1.8. The partial DOS of $Sr_3Ge_2O_4Se_3$ clearly shows that, the maximum of VB is mainly occupied by Se-4*p* and O-2*p* orbitals, wihle the Ge-4*s* and Se-4*p* mainly contribute to the minimum of CB. In $SrGe_2O_3S_2$, similar electronic configuration is observed. The top of VB is composed of S-3*p* and O-2*p*, while the bottom of CB consists of Ge-4*s* and S-3*p*. The hybridations of electronic orbitals are consistent with the crystal structures of $Sr_3Ge_2O_4Se_3$ and $SrGe_2O_3S_2$: in $Sr_3Ge_2O_4Se_3$, $[GeOSe_3]$ and $[GeO_4]$ tetrahedra form the zero-dimensional $[Ge_2O_4Se_3]^{6-}$ units; in $SrGe_2O_3S_2$, the conner-shared $[GeO_3S]$ form 2∞

$[Ge_2O_3S_2]^{2-}$ layers. The theoretical calculations indicate that the mixed-anion $[GeOSe_3]$ and $[GeO_3S]$ have significant effect on the SHG response and large birefringence mentioned above.

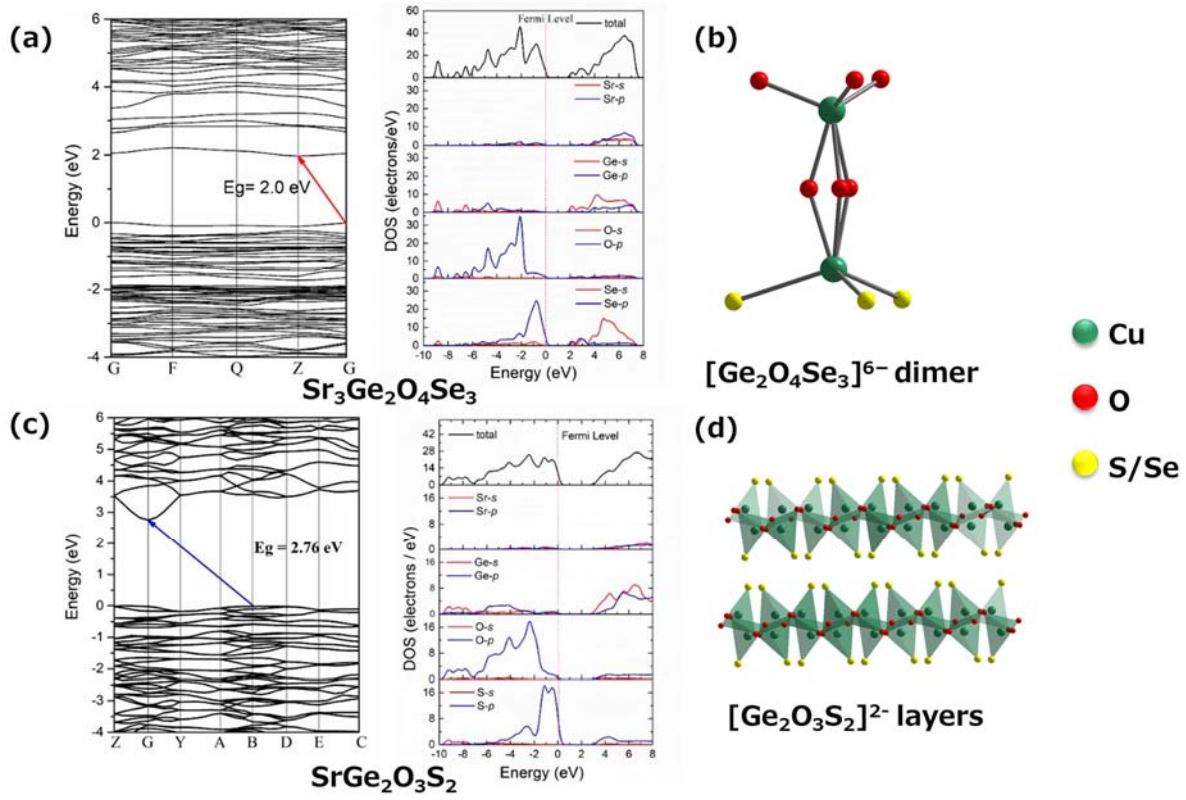

Figure 1.8. Energy band diagram and DOS of $Sr_3Ge_2O_4Se_3$ (a) and $SrGe_2O_3S_2$ (b) and the geometry features of involved $[Ge_2O_4Se_3]^{6-}$ dimer and $[Ge_2O_3S_2]^{2-}$ layers.

1.4. Non-linear Optics

Non-linear optics (NLO) is the study of the interaction between light and materials, in which the properties of the medium change because of the external electric field. Different from the traditional linear optics, the electric polarization of the material has a non-linear relationship with the external electric field in NLO. The interactions between non-linear medium and electric filed is weak in nature. In order to observe the NLO effect, the intense laser excitation is usually required. Franken and co-workers first discovered the NLO second harmonic generation (SHG) in quartz after the first demonstration of laser work in 1960.

Nowadays, NLO effect is playing a significant role in various technical fields, such as high-precision microfabrication, ablative photodecomposition, and semiconductor mask inspection.

1.4.1. NLO in Single Crystals

This part reviews the basic theory of NLO. NLO effect is caused by the change in the optical performance in the medium induced by light. Therefore, the properties of the NLO material determines the NLO process.

The optical response of a material to the applied external filed can be described by the expanding polarization P in terms of the electic filed E as follow

$$P_i = \Sigma\chi_{ij}^{(1)}E_j(\omega_1) + \Sigma\chi_{ijk}^{(2)}E_j(\omega_1)E_k(\omega_2) + \Sigma\chi_{ijkl}^{(3)}E_j(\omega_1)E_k(\omega_2)E_l(\omega_3) + \ldots, \quad (1.1)$$

where $\chi_{ij}^{(1)}$ is the linear polization susceptibility, $\chi_{ijk}^{(2)}$ and $\chi_{ijkl}^{(3)}$ are the second and third order nonlinear polization susceptibilities. The values of the susceptibilities gradually decreased by several orders of magnitude. ω_1, ω_2, and ω_3, … are the angular frequencies under different external electric filed.

Generally, the intensity of optical frequency electric field of general light source is small, and the first term in Eq. 1.1 alone is sufficient to describe the linear optical properties of materials, such as refraction, reflection, birefringence and diffraction. Laser is a kind of light with extremely strong frequency electric field. The second and third nonlinear terms in the Eq. 1.1 can play important roles and different nonlinear optical phenomena can be observed. In this case, the polarizability of crystals will no longer be a constant, but a function of the optical frequency electric field E. Taking the first derivative of the electric polarization intensity P of the crystal to the optical frequency electric field E, the following can be obtained,

$$\frac{dP_i}{dE} = \Sigma\chi_{ij}^{(1)} + \Sigma\chi_{ijk}^{(2)}E + \Sigma\chi_{ijkl}^{(3)}EE + \ldots \quad (1.2)$$

Based on Eq. 1.2, the linear optical property is only related to $\chi_{ij}^{(1)}$, and the higher order non-linear polarization term can cause the NLO effect. Among them, the NLO effect caused by the quadratic term $\chi_{ijk}^{(2)}E$ is the most significant and most widely used. The quadratic term in Eq. 1.1 can be written as,

$$P_i^{(2)} = \Sigma\chi_{ijk}^{(2)}(\omega_1, \omega_2, \omega_3)E_j(\omega_1)E_k(\omega_2) \quad (1.3)$$

where $P_i^{(2)}$ is the nonlinear electric polarization intensity component generated by the secondary polarization term, and $\chi_{ijk}^{(2)}$ is the second-order nonlinear polarization coefficient, ω_1 and ω_2,are the angular frequencies of the light, $\omega_3 = \omega_1 \pm \omega_2$, E_j and E_k are the optical frequency electric field component of incident light. When $\omega_3 = \omega_1 + \omega_2$, the SHG effect is called sum frequency generation (SFG), and it generates frequency multiplication light; when $\omega_3 = \omega_1 - \omega_2$, the SHG effect is called difference frequency generation (DFG), and the laser passes through the crystal to create a direct current electric polarization, which is called optical rectification.

The optical phenomena mentioned above are all NLO effect, which doesn't obey the general rules of linear optics.

1.4.2. Second Order NLO Susceptibility

The second order electric polarization intensity $P_i^{(2)}$ is proportional to the second order non-linear polarization susceptibility $\chi_{ijk}^{(2)}$. When $\omega_1 = \omega_2 = \omega$, $\omega_3 = \omega_1 + \omega_2 = 2\omega$, then Eq. 1.3 is

$$P_i(2\omega) = \Sigma\chi_{ijk}^{(2)}E_j(\omega)E_k(\omega) \quad (1.4)$$

where $\chi_{ijk}^{(2)} \equiv \chi_{ijk}(2\omega)$ is second order NLO susceptibility, also known as frequency multiplication susceptibility d_{ijk}.

The second order NLO susceptibility is the third order tensor describing the SHG process, which is a function of three kinds of frequency (ω_3, ω_1, ω_2). In general, with a total of 27 independent components, it can only exist in 20 piezoelectric crystal systems with noncentrosymmetric structure. Only in this way, the second order NLO susceptibilitiy components are not all zero.

Because the sequence of the two optical frequency electric field components in the NLO crystal has no effect on the intensity, the *jk* subscript is symmetric. Therefore, the double subscripts $jk = kj$ can be replaces by single subscript *n*, which is

n	1	2	3	4	5	6
$jk = kj$	11	22	33	23 = 32	31 = 13	12 = 21

$$\chi_{ijk}(2\omega) = \chi_{ikj}(2\omega) = \chi_{in}(2\omega) \quad (1.5)$$

Therefore, the 27 independent components decrease to 18 independent components of χ_{in}.

In 1962, Kleinman found that in the mid-near infrared and visible light region, the frequency of light was far away from the resonant frequency region of crystal ions. Because the mass of ions was much larger than that of electrons, ions can not keep up with the periodic vibration of optical frequency electric field, and the contribution of ion displacement to the electric polarization intensity of crystal was almost zero. Therefore, the NLO susceptibility mainly depends on the electron motion, and the polarization free energy of crystal (G) can be simplified as

$$G = -1/3\ \chi_{ijk}(2\omega)E_iE_jE_k \quad (1.6)$$

Taking the derivative of G to E, as well as the subscript of E has no relationships with the sequence of frequency, then

$$\frac{\partial^3 G}{\partial E_i \partial E_j \partial E_k} = \frac{\partial^3 G}{\partial E_j \partial E_k \partial E_i} = \frac{\partial^3 G}{\partial E_k \partial E_i \partial E_j} \quad (1.7)$$

Taking Eq. 1.6 into Eq. 1.7 and considering the relationship in Eq. 1.5, we have

$$\chi_{ijk} = \chi_{jki} = \chi_{kij} = \chi_{ikj} = \chi_{jik} = \chi_{kji} \quad (1.8)$$

The Eq. 1.8 is the Kleinman symmetry. Based on Kleinman symmetry, the 18 independent components decrease to 10. Therefore, the matrix of χ_{in} is

$$\begin{bmatrix} \chi_{11} & \chi_{12} & \chi_{13} & \chi_{14} & \chi_{15} & \chi_{16} \\ \chi_{16} & \chi_{22} & \chi_{23} & \chi_{24} & \chi_{14} & \chi_{12} \\ \chi_{15} & \chi_{24} & \chi_{33} & \chi_{23} & \chi_{13} & \chi_{14} \end{bmatrix}$$

And the second order NLO susceptibility of point groups 422 and 622 in the piezoelectric crystal system are all zero. Therefore, the NLO effect can only be observed in 18 point groups among the 32 crystal systems.

1.4.3. Designing Novel UV NLO Single Crystals

Promising NLO single crystals should crystallize in noncentrosymmetric space groups as a sufficient condition. Towards the creation of novel NCS single crystals containing functional building block units based on the anionic group theory, several strategies have been developd, including Π-conjuncted systems, second-order Jahn-Teller (SOJT) distorted transition metal cations with d^0 electric configurations, stereochemically-active lone-pair (SCALP) cations, and d^{10} transition metal cations with local polar displacements.[100-102]

The requirements for NLO single crystals which can be used in UV regions are as following: a wide band gap, excellent SHG coefficients, chemical and thermal stability, phase-matchability, moderate birefringence, and large size. The most favorable anionic units for UV crystals are the planar $[BO_3]^{3-}$ as well as isoelectronic anions such as $[CO_3]^{3-}$ and $[NO_3]^{3-}$, which

posseses not only large SHG coefficients but also moderate birefringence. Phosphates with acentric tetrahedral units are considered as attractive candidates for potential UV application due to the wide UV transparency and ease to be grown large bulk crystals.

Recently, mixed-anion-directed strategies have attracted growing attention due to the heteroleptic coordination environment formed by mixed-anion groups, which results in the more polarized atomic displacement around the building block units and further enhanced SHG properties. For UV applications, the introduction of halogen elements results in a wider band gap and stronger SHG intensity, because their higher electronegativity and polarizability than oxygen atoms.

In contrast, chalcogenide atoms have been underdeveloped for UV applications. Metal chalcogenides are most investigated as infrared NLO materials due to their lower bond stretching frequency in IR regions. Single anion metal chalcogenides usually exhibit significantly strong SHG efficiency and birefringence, while the band gap and laser damage thresholds are small. Recently, mixed-anion of oxide and chalcogenide is known to be more promising NLO candidates, which can finely tune the SHG, birefringence, band gap, as well LDT in one crystal, such as $SrZnS_2O$ (2 × KDP, E_g = 3.89 eV), $BaGeSe_2O$ (1.1 × AGS, E_g = 3.18 eV). Although those oxychalcogenides show strong SHG intensities, their band gaps are too narrow to be applied in UV regions.

1.5. Flux Growth Method

Flux growth utilizes a high-temperature of sinple inorganic compounds, such as $BaCl_2$, NaCl, KI, as the solvent for crystallization, which melt at conventiently low temperatures. The melting point can be further reduced by the combination of inorganic compounds, which forms a lower melting eutectic. To be a good flux, the inorganic compound needs to meet the following criteria, including:

1. Dissolving a large quantity of the regents,
2. Relatively low melting point,
3. Solubility changed with temperature,
4. Non-volatility and non-toxicity,
5. Unreaction toward the crucible,
6. Easy separation from crystals after growth,
7. Low cost.

During the crystal growth, the solution becomes supersaturated when the reagent dissolves in a suitable solvent and crystallization occurs. Reducing the total volume of melt solvent by cooling or evaporation are the common ways to achieving supersaturated.

A large number of oxysulfide single crystals have been obtained flux growth method. These oxysulfide compounds are obtained incidentally from reactions that are considered to be oxygen free, usually under vacuum atmosphere. Sinple oxides from the starting materials act as oxygen agent. Some oxysulfides, however, can be obtained via solid state synthesis. Comparing with flux growth method, very precise control of the oxygen content is required, because oxides are of high stability while sulfides usually decompose with the elevated temperature.

Many oxysulfide single crystals have been grown using alkali chloride fluxes in a sealed fused silica tube under relatively vacuum environment. For example, $SrZn_2S_2O$, the first NLO phase matchable oxysulfide material, was obtained using a eutectic KF-KCl mixture under 900 ℃ for several days. $AeGeS_2O$ (Ae = Sr, Ba) single crystals were prepared by the mixtures of starting materials and KI as the molten flux. Some oxyschalcogenide single crystals don't need alkali chlorides as flux but the starting materials as the self flux. $Sr_3Ge_2O_4Se_3$ single crystals were found in the reaction productions on the SrSe, $GeSe_2$, Sb_2Se_3, and Sb_2O_3, where Sb_2Se_3

with the lowest melting point (611℃) acts as the flux and facilitates the reaction to take place at lower temperature.[103,104]

1.6. Objectives of this thesis

In this thesis, all compounds were synthesized by flux growth method using alkali earth metal, rare earth metal, and Ga/Ge based oxides or sulfides in a fused silica tube. Three series compounds of Ga/Ge-based oxysulfide/oxide single crystals were introduced.

1.6.1. $La_3Ga_3Ge_2S_3O_{10}$

In order to develop novel NLO material for UV applications, mixed-anion directed strategy was applied to find oxysulfides with NCS structure as well tunable wide band gap. Here, we report mixed-anion oxysulfide $La_3Ga_3Ge_2S_3O_{10}$, which that crystallized in the hexagonal non-centrosymmetric space group *P*-62*c*, which exhibits phase-matchable SHG property of twice KDP intensity and a wide band gap of 4.70 eV. The theoretical calculations indicate that the attractive optical properties are mainly attributed to the S and O orbitals hybridized with transition metals. The details will be given in Chapter 3.

1.6.2. $La_4(GeS_2O_2)_3$

A novel germanium based oxysulfide $La_4(GeS_2O_2)_3$ was obtained by the flux growth method via a $BaCl_2$-$CaCl_2$ mixture, which crystallizes in the centrosymmetric space group *R*-3. The structure of $La_4(GeS_2O_2)_3$ features from a complex three-dimensional anion order in the framework, which consists of rarely existed GeS_2O_2 tetrahedra and three types of La-centered polyhedra. The structure of $La_4(GeS_2O_2)_3$ is of high similarity with apatite germante $La_{9.33}(GeO_4)_6O_2$. The UV-vis measurement revealed the optical band gap of 3.67 eV, which is

well consistent with the first-principles calculations. The details will be discussed in Chapter 4.

1.6.3. $Ce_2CaMg_2Ge_3O_{12}$

A new germanate garnet single crystal $Ce_2CaMg_2Ge_3O_{12}$ was grown through a $BaCl_2$-$CaCl_2$ eutectic mixture, which crystallizes in the centrosymmetric space group *Ia*-3*d*. The common garnet formula can be descripted as $A_3B_2C_3O_{12}$, where Ce/Ca, Mg, and Ge occupied the A, B, and C sites, respectively. The combination of UV-vis spectroscopy and first-principles calculations suggest the band gap of 2.21 eV between the VBM composed of Ce-4*f* orbital and the CBM consisting of Ce-5*d* orbital. The photoluminescene emission spectroscopy exhibits a peak around 600 nm, which is corresponding to the transition from 5*d* to 4*f* energy level. The discussions will be shown in Chapter 5.

References in chapter 1

1. Hiroshi Kageyama, Katsuro Hayashi, Kazuhiko Maeda, J. Paul Attfield, Zenji Hiroi, James M. Rondinelli & Kenneth R. Poeppelmeier. Expanding frontiers in materials chemistry and physics with multiple anions. *Nat. Commun*. **2018**, 9, 772.
2. Ebbinghaus, S. G. et al. Perovskite-related oxynitrides – Recent developments in synthesis, characterisation and investigations of physical properties. *Prog. Solid State Chem*. **2009**, 37, 173–205.
3. Tsujimoto, Y., Yamaura, K. & Takayama-Muromachi, E. Oxyfluoride chemistry of layered perovskite compounds. *Appl. Sci*. **2012**, 2, 206–219.
4. Kobayashi, Y., Tian, M., Eguchi, M. & Mallouk, T. E. Ion-exchangeable, electronically conducting layered perovskite oxyfluorides. *J. Am. Chem. Soc*. **2009**, 131, 9849–9855.
5. Iwazaki, Y., Suzuki, T. & Tsuneyuki, S. Negatively charged hydrogen at oxygen-vacancy sites in BaTiO3: Density-functional calculation. *J. Appl. Phys*. **2010**, 108, 083705.
6. Shannon, R. D. Revised effective ionic radii and systematic studies of interatomic distances in halides and chalcogenides. *Acta Cryst*. **1976**, A32, 751–767.
7. S. Bereznev, H. Kocharyan, N. Maticiuc, R. Naidu, O. Volobujeva, A. Tverjanovich, and J. Kois. One-stage pulsed laser deposition of conductive zinc oxysulfide layers. *Appl. Surf. Sci*. **2017**, 425, 722–727.
8. Yan-Yan Li, Wen-Jing Wang, Hui Wang, Hua Lin, and Li-Ming Wu. Mixed-Anion Inorganic Compounds: A Favorable Candidate for Infrared Nonlinear Optical Materials. *Cryst. Growth Des*. **2019**, 19, 4172−4192.
9. H. Hiramatsu, K. Ueda, T. Kamiya, H. Ohta, M. Hirano, and H. Hosono. Synthesis of single-phase layered oxychalcogenide La2CdO2Se2: crystal structure, optical and electrical properties. *J. Mater. Chem*. **2004**, 14, 2946.

10. S. Sinha, D. K. Nandi, S. H. Kim, and J. Heo. Atomic-layer-deposited buffer layers for thin film solar cells using earth-abundant absorber materials: A review. *Sol. Energy Mater. Sol. Cells*. **2018**, 176, 49–68.

11. Pitha, J. J., Smith, A. L., and Ward, R. The preparation of lanthanum oxysulfide and its properties as a base material for phosphors stimulated by infrared. *J. Am. Chem. Soc*. **1947**, 69, 1870–1871.

12. Zachariasen, W. H. Crystal chemical studies of the 5f-series of elements. VII. The crystal structure of Ce2O2S, La2O2S and Pu2O2S. *Acta Crystallogr*. **1949**, 2, 60–62.

13. Flahaut, J., Guittard, M., and Patrie, M. Les oxysulfures Me2O2S des élements du groupe des terres rares. *Bull. Soc. Chim. Fr*. **1958**, 7, 990–994.

14. M. Goga, R. Seshadri, V. Ksenofontov, P. Gutlich and W. Tremel. Ln2Ti2S2O5 (Ln = Nd, Pr, Sm): a novel series of defective Ruddlesden–Popper phases. *Chem. Commun.* **1999**, 979–980.

15. Cody, J. A., and Ibers, J. A. Synthesis and characterization of the new rareearth/ transition-metal oxysulfides La6Ti2S8O5 and La4Ti3S4O8. *J. Solid State Chem*. **1995**, 114, 406–412.

16. A. Mazurier, M. Guittard et S. Jaulmes. Structure cristalline d'un oxysulfure isotype de la mélilite, La3.33Ga6O2S12. *Acta Cryst*. **1982**, B38, 379-382.

17. S. Jaulmes, A. Mazurier et M. Guittard. Structure de l'oxypentasulfure de gallium et de trilanthane, GaLa3OS5. *Acta Cryst*. **1983**, C39, 1594-1597.

18. Tranchitella, L. J., Fettinger, J. C., and Eichhorn, B. W. Synthesis and structural analysis of Sr5.8La4.4Ti7.8S24O4 and La14Ti8S33O4 : two new oxysulfides containing a common [(Ti4S2O4)(TiS6)4/2]12- layer. *Chem. Mater*. **1996**, 8, 2265–2271.

19. Cario, L., Deudon, C., Meerschaut, A., and Rouxel, J. Synthesis and structure determination of La8Ti10S24O4. *J. Solid State Chem*. **1998**, 136, 46–50.

20. Deudon, C., Meerschaut, A., Cario, L., and Rouxel, J. Preparation and crystal structure determination of La20Ti11S44O6. *J. Solid State Chem*. **1995**, 120, 164–169.

21. Boyer-Candalen, C., Deudon, C., and Meerschaut, A. Synthesis and structure determination of Nd16Ti5S17O17. *J. Solid State Chem*. **2000**,152, 554–559.

22. Vovan, T., Dugué, J., and Guittard, M. Oxysulfures mixtes de vanadium et de terre rare de formule generale R5V3S6O7 (R = lanthane a neodyme). *Comptes Rendus l'Acad. Sci*. **1981**, 292, 957–959.

23. Vovan, T., Dugué, J., and Guittard, M. Oxysulfures mixtes de chrome III et de terres rares. *Mater. Res. Bull*. **1978**, 13, 1163–1166.

24. Dugué, J., Vovan, T., and Villers, J. Etude structurale des oxysulfures de chrome(III) et de terres rares. II. Structure de I'oxysulfure CeCrOS2. *Acta Crystallogr*. **1980b**, B36, 1294–1297.

25. Ijjaali, I., Deng, B., and Ibers, J. A. Seven new rare-earth transition-metal oxychalcogenides: syntheses and characterization of Ln4MnOSe6 (Ln=La, Ce, Nd), Ln4FeOSe6 (Ln=La, Ce, Sm), and La4MnOS6. *J. Solid State Chem*. **2005**, 178, 1503–1507.

26. Mayer, J. M., Schneemeyer, L. F., Siegrist, T., Waszczak, J. V., and Van Dover, B. New layered iron-lanthanum-oxide-sulfide and -selenide phases: Fe2La2O3E2(E=S,Se). Angew. Chemie Int. Ed. English. **1992**, 31, 1645–1647.

27. Palazzi,M. Préparation et affinement de la structure de (LaO) CuS. *Comptes Rendus Hebd. l'Acad. Sci.* **1981**, 292, 789–791.

28. Huang, F. Q., Brazis, P., Kannewurf, C. R., and Ibers, J. A. Synthesis, structure, electrical conductivity, and band structure of the rare-earth copper oxychalcogenide La5Cu6O4S7. *J. Solid State Chem*. **2000**, 155, 366–371.

29. Kusainova, A. M., Berdonosov, P. S., Akselrud, L. G., Kholodkovskaya, L. N., Dolgikh, V. A., and Popovkin, B. A. New layered compounds with the general composition (MO)

(CuSe), where M = Bi, Nd, Gd, Dy, and BiOCuS: syntheses and crystal structure. *J. Solid State Chem*. **1994**, 112, 189–191.

30. L. Cario, H. Kabbour, C. Guillot-Deudon and A. Meerschaut. A mixed-valent niobium oxy-sulfide, La2Nb3S2O8. *Acta Cryst*. **2003**, C59, i55-i56.

31. Cario, L., Popa, A. F., Lafond, A., Guillot-Deudon, C., Kabbour, H.,Meerschaut, A., et al. Cation deficient layered ruddlesden–popper-related oxysulfides La2LnMS2O5 (Ln = La, Y; M = Nb, Ta). *Inorg. Chem*. **2007**, 46, 9584–9590.

32. Altmannshofer, S., and Johrendt, D. Synthesis, crystal structure and magnetismof the new oxysulfide Ce3NbO4S3. *Zeitschrift für Anorg. Allg. Chem*. **2008**, 634, 1361–1364.

33. Boyer-Candalen, C., Meerschaut, A., and Palvadeau, P. Crystal structure determination of the new compound Sm3NbO4S3. *Mater. Res. Bull*. **2000**, 35, 1593–1601.

34. Kabbour, H., Cario, L., Deudon, C., and Meerschaut, A. A gadolinium and niobium oxide sulfide, Gd3NbS3O4. *Acta Crystallogr. Sect. E Struct*. **2003**, 59, i101–i102.

35. Brennan, T. D., and Ibers, J. A. Metal-metal bonding and mixedvalent tantalum in La2Ta3S2O8. J. Solid State Chem. **1992**, 98, 82–89.

36. Guo, G., Wang, Y., Chen, J., Zhuang, H., Huang, J., and Zhang, Q. Samarium tantalum oxysulfide, Sm2Ta3S2O8. *Acta Crystallogr. Sect. C Cryst. Struct. Commun*. **1995**. 51, 1964–1966.

37. Palazzi, M., Carcaly, C., and Flahaut, J. Un nouveau conducteur ionique (LaO)AgS. *J. Solid State Chem*. **1980**, 35, 150–155.

38. Guittard, M., Jaulmes, S., Loireau-Lozac'h, A. M., Mazurier, A., Berguer, F., and Flahaut, J. Étude du systeme La2S3-La2O3-Ga2O3-Ga2S3: description structurale des phases quaternaires et approche du diagramme de phase. *J. Solid State Chem*. **1985**, 58, 276–289.

39. Jaulmes, S. Oxysulfure de gallium et de lanthane LaGaOS2. *Acta Crystallogr. Sect. B Struct. Crystallogr. Cryst. Chem*. **1978**, 34, 2610–2612.

40. Jaulmes, S., Godlewski, E., Palazzi, M., and Etienne, J. (). Deux structures isotypes a sites anioniques et cationiques lacunaires: (CeO)4Ga2S5 et (LaO)4As2S5. *Acta Crystallogr. Sect. B Struct. Crystallogr. Cryst. Chem*. **1982**, 38, 1707–1710.

41. Guittard, M., Benazeth, S., Dugue', J., Jaulmes, S., Palazzi, M., Laruelle, P., et al. Oxysulfides and oxyselenides in sheets, formed by a rare earth element and a second metal. *J. Solid State Chem*. **1984**, 51, 227–238.

42. Kabbour, H., Cario, L.,Moëlo, Y., andMeerschaut, A. Synthesis, X-Ray and optical characterizations of two new oxysulfides: LaInS2O and La5In3S9O3. *J. Solid State Chem*. **2004**, 177, 1053–1059.

43. Gastaldi, L., Carré, D., and Pardo,M. P. Structure de l'oxysulfure d'indium et de lanthane In6La10O6S17. *Acta Crystallogr. Sect. B Struct. Crystallogr. Cryst. Chem*. **1982**, 38, 2365–2367.

44. Aliev, O. M., and Tanryverdiev, V. S. The synthesis and some physical properties of rare-earth oxysulfostibnites. *Zhurnal Neorg. Khimii*. **1997**, 42, 1918–1921.

45. Pardo, M.-P., Céolin, R., and Guittard, M. Sur les oxysulfures a deux élements metalliques, terre rare et bismuth, ou terre rare et antimoine. *Comptes rendus Hebd. l'Acad. Sci*. **1976**, 283, 735–738.

46. Nakai, I., Nagashima, K., Koto, K., and Morimoto, N. Crystal chemistry of oxide–chalcogenide. I. The crystal structure of sarabauite CaSb10O10S6. *Acta Crystallogr. Sect. B Struct. Crystallogr. Cryst. Chem*. **1978**, 34, 3569–3572.

47. Salter, E. J. T., Blandy, J.N., and Clarke, S. J. Crystal and magnetic structures of the oxide sulfides CaCoSO and BaCoSO. *Inorg. Chem*. **2016**, 55, 1697–1701.

48. Petrova, S. A., Mar'evich, V. P., Zakharov, R. G., Selivanov, E. N., Chumarev, V. M., and Udoeva, L. Y. Crystal structure of zinc calciumoxysulfide. *Dokl. Chem*. **2003**, 393, 255–258.

49. Broadley, S., Gál, Z. A., Corà, F., Smura, C. F., and Clarke, S. J. (). Vertexlinked ZnO2S2 tetrahedra in the oxysulfide BaZnOS: a new coordination environment for zinc in a condensed solid. *Inorg. Chem*. **2005**, 44, 9092–9096.

50. Tsujimoto, Y., Juillerat, C. A., Zhang, W., Fujii, K., Yashima, M., Halasyamani, P. S., et al. Function of tetrahedral ZnS3O building blocks in the formation of SrZn2S2O: a phase matchable polar oxysulfide with a large second harmonic generation response. *Chem. Mater*. **2018**, 30, 6486–6493.

51. R. Q. Wang, F. Liang, F. K. Wang, Y. W. Guo, X. Zhang, Y. Xiao, K. J. Bu, Z. S. Lin, J. Y. Yao, T. Y. Zhai, F. Q. Huang. Sr6Cd2Sb6O7S10: Strong SHG Response Activated by Highly Polarizable Sb/O/S Groups. *Angew. Chem. Int. Ed.* **2019**, 58, 8078–8081.

52. Kiyonori Ogisu, Akio Ishikawa, Yoshiki Shimodaira, Tsuyoshi Takata, Hisayoshi Kobayashi, and Kazunari Domen. Electronic Band Structures and Photochemical Properties of La-Ga-based Oxysulfides. *J. Phys. Chem. C*. **2008**, 112, 11978–11984.

53. Qian Wang, and Kazunari Domen, et al. Oxysulfide photocatalyst for visible-light-driven overall water splitting. *Nature Materials*. 2019, 18, 827–832.

54. D. C. Johnston. The puzzle of high temperature superconductivity in layered iron pnictides and chalcogenides. Adv. Phys. **2010**, 59, 803–1061.

55. S. K. Singh, A. Kumar, B. Gahtori, Shruti, G. Sharma, S. Patnaik, and V. P. S. Awana. Bulk superconductivity in bismuth oxysulfide Bi4O4S3. *J. Am. Chem. Soc*. **2012**,134, 16504–16507.

56. Dubois, V., Pecquenard, B., Soulé, S., Martinez, H., and Le Cras, F. Dual cation- and anion-based redox process in lithium titanium oxysulfide thin film cathodes for all-solid-state lithium-ion batteries. *ACS Appl. Mater. Interfaces*. **2017**, 9, 2275–2284.

57. Qiao, Y., Hu, X., Liu, Y., Liang, G., Croft, M. C., and Huang, Y. Surface modification of MoOxSy on Porous TiO2 nanospheres as an anode material with highly reversible and ultra-fast lithium storage properties. *J. Mater. Chem. A*. **2013**, 1, 15128–15134.

58. A. Krzton-Maziopa, Z. Guguchia, E. Pomjakushina, V. Pomjakushin, R. Khasanov, H. Luetkens, P. K. Biswas, A. Amato, H. Keller, and K. Conder. Superconductivity in a new layered bismuth oxyselenide: LaO0.5F0.5BiSe2. *J. Phys. Condens. Matter*. **2014**, 26, 1–6.

59. J. Sui, J. Li, J. He, Y.-L. Pei, D. Berardan, H. Wu, N. Dragoe, W. Cai, and L.-D. Zhao. Texturation boosts the thermoelectric performance of BiCuSeO oxyselenides. *Energy Environ. Sci*. **2013**, 6, 2916–2920.

60. K. Ueda, H. Hiramatsu, H. Ohta, M. Hirano, T. Kamiya, and H. Hosono. Single-atomic-layered quantum wells built in wide-gap semiconductors LnCuOCh (Ln = lanthanide, Ch = chalcogen). *Phys. Rev. B - Condens. Matter Mater. Phys*. **2004**, 69, 2–5.

61. L.-D. Zhao, J. He, D. Berardan, Y. Lin, J.-F. Li, C.-W. Nan, and N. Dragoe. BiCuSeO oxyselenides: new promising thermoelectric materials. *Energy Environ. Sci*. **2014**, 7, 2900–2924.

62. K. Ueda, and H. Hosono. Band gap engineering, band edge emission, and p-type conductivity in wide-gap LaCuOS 1-xSe x oxychalcogenides. J. Appl. Phys. **2002**, 91, 4768–4770.

63. J. Li, J. Sui, Y. Pei, X. Meng, D. Berardan, N. Dragoe, W. Cai, and L.-D. Zhao. The roles of Na doping in BiCuSeO oxyselenides as a thermoelectric material. J. Mater. Chem. A. **2014**, 2, 4903-4906.

64. O. J. Rutt, G. R. Williams, and S. J. Clarke. Reversible lithium insertion and copper extrusion in layered oxysulfides. *Chem. Commun*. **2006**, 88, 2869–2871.

65. F. Han, D. Wang, C. D. Malliakas, M. Sturza, D. Y. Chung, X. Wan, and M. G. Kanatzidis. (CaO)(FeSe): A Layered Wide-Gap Oxychalcogenide Semiconductor. *Chem. Mater*. **2015**, 27, 5695–5701.

66. H. Hiramatsu, K. Ueda, T. Kamiya, H. Ohta, M. Hirano, and H. Hosono. Synthesis of single-phase layered oxychalcogenide La2CdO2Se2: crystal structure, optical and electrical properties. J. Mater. Chem. **2004**, 14, 2946-2950.

67. J. Wu, C. Tan, Z. Tan, Y. Liu, J. Yin, W. Dang, M. Wang, and H. Peng. Controlled Synthesis of High-Mobility Atomically Thin Bismuth Oxyselenide Crystals. Nano Lett. **2017**, 17, 3021–3026.

68. F. Li, J.-F. Li, L.-D. Zhao, K. Xiang, Y. Liu, B.-P. Zhang, Y.-H. Lin, C.-W. Nan, and H.-M. Zhu. Polycrystalline BiCuSeO oxide as a potential thermoelectric material. *Energy Environ. Sci*. **2012**, 5, 7188-7195.

69. L. X. Pan, Q. L. Xia, S. L. Ye, N. Ding, and Z. R. Liu. First principles study of electronic structure, chemical bonding and elastic properties of BiOCuS. *Trans. Nonferrous Met. Soc. China (English Ed*. **2012**, 22, 1197–1202.

70. J. Li, J. Sui, C. Barreteau, D. Berardan, N. Dragoe, W. Cai, Y. Pei, and L. D. Zhao. Thermoelectric properties of Mg doped p-type BiCuSeO oxyselenides. *J. Alloys Compd*. **2013**, 551, 649–653.

71. S. D. N. Luu, and P. Vaqueiro. Synthesis, characterisation and thermoelectric properties of the oxytelluride Bi2O2Te. *J. Solid State Chem*. **2015**, 226, 219–223.

72. Y. Ye, R. Lim, and J. M. White. High mobility amorphous zinc oxynitride semiconductor material for thin film transistors. *J. Appl. Phys*. **2009**, 106, 074512.

73. T. Yamazaki, K. Shigematsu, Y. Hirose, S. Nakao, I. Harayama, D. Sekiba, and T. Hasegawa. Amorphous ZnOxNy thin films with high electron Hall mobility exceeding 200 $cm^2 V^{-1} s^{-1}$. *Appl. Phys. Lett*. **2016**, 109, 262101.

74. Z. W. Fu, W. Y. Liu, C. L. Li, Q. Z. Qin, Y. Yao, and F. Lu. High-k lithium phosphorous oxynitride thin films. *Appl. Phys. Lett*. **2003**, 83, 5008–5010.

75. K. M. Niang, B. C. Bayer, J. C. Meyer, and A. J. Flewitt. Highly stable amorphous zinc tin oxynitride thin film transistors under positive bias stress. *Appl. Phys. Lett*. **2017**,111, 122109.

76. M. Ahmed, and G. Xinxin. A review of metal oxynitrides for photocatalysis. *Inorg. Chem. Front*. **2016**, 3, 578–590.

77. M. Nisula, Y. Shindo, H. Koga, and M. Karppinen. Atomic Layer Deposition of Lithium Phosphorus Oxynitride. *Chem. Mater*. **2015**, 27, 6987–6993.

78. A. B. Jorge, J. Oró-Solé, A. M. Bea, N. Mufti, T. T. M. Palstra, J. A. Rodgers, J. P. Attfield, and A. Fuertes. Large coupled magnetoresponses in EuNbO2N. *J. Am. Chem. Soc*. **2008**, 130, 12572–12573.

79. M. Yang, J. Oró-Solée, J. A. Rodgers, A. B. Jorge, A. Fuertes, and J. P. Attfield. Anion order in perovskite oxynitrides. *Nat. Chem*. **2011**, 3, 47–52.

80. J. Xu, C. Pan, T. Takata, and K. Domen. Photocatalytic overall water splitting on the perovskite-type transition metal oxynitride CaTaO2N under visible light irradiation. *Chem. Commun*. **2015**, 51, 7191–7194.

81. N. Brinkmann, D. Sommer, G. Micard, G. Hahn, and B. Terheiden. Electrical, optical and structural investigation of plasma-enhanced chemical-vapor-deposited amorphous silicon oxynitride films for solar cell applications. *Sol. Energy Mater. Sol. Cells*. **2013**, 108, 180–188.

82. F. Xian, J. Ye, S. Gu, H. H. Tan, and C. Jagadish. Structural transition, subgap states, and carrier transport in anion-engineered zinc oxynitride nanocrystalline films. *Appl. Phys. Lett*. **2016**, 109, 023109.

83. A. P. Black, H. Suzuki, M. Higashi, C. Frontera, C. Ritter, C. De, S. Athinarayanan, R. Abe, and A. Fuertes. New rare earth hafnium oxynitride perovskites with photocatalytic activity in water oxidation and reduction. *Chem. Commun*. **2018**, 54, 1525–1528.

84. F. Zhang, A. Yamakata, K. Maeda, Y. Moriya, T. Takata, J. Kubota, K. Teshima, S. Oishi, and K. Domen. Cobalt-modified porous single-crystalline LaTiO2N for highly efficient water oxidation under visible light. *J. Am. Chem. Soc*. **2012**, 134, 8348–8351.

85. S. J. Clarke, P. Adamson, S. J. C. Herkelrath, O. J. Rutt, D. R. Parker, M. J. Pitcher, and C. F. Smura. Structures, physical properties, and chemistry of layered oxychalcogenides and oxypnictides. *Inorg. Chem*. **2008**, 47, 8473–8486.

86. H. Hiramatsu, Y. Kamihara, H. Yanagi, K. Ueda, T. Kamiya, M. Hirano, and H. Hosono. Layered mixed-anion compounds: Epitaxial growth, active function exploration, and device application. *J. Eur. Ceram. Soc*. **2009**, 29, 245–253.

87. H. Le Dréo, O. Banakh, H. Keppner, P. A. Steinmann, D. Briand, and N. F. de Rooij. Optical, electrical and mechanical properties of the tantalum oxynitride thin films deposited by pulsing reactive gas sputtering. *Thin Solid Films*. **2006**, 515, 952–956.

88. À. R. Garcia, C. Clausell, and A. Barba. Oxynitride glasses: A review. *Bol. La Soc. Esp. Ceram. y Vidr*. **2016**, 55, 209–218.

89. Takumi Watanabe, Hiroshi Yanagi, Toshio Kamiya, Yoichi Kamihara, Hidenori Hiramatsu, Masahiro Hirano, and Hideo Hosono. Nickel-Based Oxyphosphide Superconductor with a Layered Crystal Structure, LaNiOP. *Inorg. Chem*. **2007**, 46, 7719–7721.

90. Takumi Watanabe, Hiroshi Yanagi, Yoichi Kamihara, Toshio Kamiya, Masahiro Hirano, Hideo Hosono. Nickel-based layered superconductor, LaNiOAs. *Journal of Solid State Chemistry*. **2008**, 181, 2117–212.

91. S. W. Kim, N. Pereira, N. A. Chernova, F. Omenya, P. Gao, M. S. Whittingham, G. G. Amatucci, D. Su, and F. Wang. Structure Stabilization by Mixed Anions in Oxyfluoride Cathodes for High-Energy Lithium Batteries. *ACS Nano*. **2015**, 9, 10076–10084.

92. Alex M. Ganose, Madeleine Cuff, Keith T. Butler, Aron Walsh, and David O. Scanlon. Interplay of Orbital and Relativistic Effects in Bismuth Oxyhalides: BiOF, BiOCl, BiOBr, and BiOI. *Chem. Mater*. **2016**, 28, 1980−1984.

93. K. Kawahara, A. Chikamatsu, T. Katayama, T. Onozuka, D. Ogawa, K. Morikawa, E. Ikenaga, Y. Hirose, I. Harayama, D. Sekiba, T. Fukumura, and T. Hasegawa. Topotactic fluorination of perovskite strontium ruthenate thin films using polyvinylidene fluoride. CrystEngComm. **2017**, 19, 313–317.

94. T. Katayama, A. Chikamatsu, H. Kamisaka, H. Kumigashira, and T. Hasegawa. Experimental and theoretical investigation of electronic structure of SrFeO3−xFx epitaxial thin films prepared via topotactic reaction. *Appl. Phys. Express*. **2016**, 9, 025801.

95. T. Onozuka, A. Chikamatsu, T. Katayama, Y. Hirose, I. Harayama, D. Sekiba, E. Ikenaga, M. Minohara, H. Kumigashira, and T. Hasegawa. Reversible Changes in Resistance of Perovskite Nickelate NdNiO3Thin Films Induced by Fluorine Substitution. *ACS Appl. Mater. Interfaces*. **2017**, 9, 10882–10887.

96. Philippe D'Arco, Bernard Silvi, Carla Roetti, Roberto Orlando. Comparative study of spinel compounds: A pseudopotential periodic Hartree-Fock calculation of Mg2SiO4, Mg2GeO4, Al2MgO4, and Ga2MgO4. *J. Geophys. Res. B*. **1991**, 96, 6107.

97. V. KahlenbergR, X. Fischer, and C. S. J. Shaw. Polymorphism of Strontium Monogallate: The Framework Structures of β-SrGa2O4 and ABW-Type γ-SrGa2O4. *J. Solid State Chem*. **2000**, 153, 294-300.

98. V. Kahlenberg, R. X. Fischer, and J. B. Parise. The Stuffed Framework Structure of BaGa2O4. *J. Solid State Chem*. **2000**, 154, 612-618.

99. Wenhao Xing, Pan Fang, Naizheng Wang, Zhuang Li, Zheshuai Lin, Jiyong Yao, Wenlong Yin, and Bin Kang. Two Mixed-Anion Units of [GeOSe3] and [GeO3S] Originating from Partial Isovalent Anion Substitution and Inducing Moderate Second Harmonic Generation Response and Large Birefringence. *Inorg. Chem*. **2020**, 59, 16716−16724.

100. Jin Chen, Chun-Li Hu, Fei-Fei Mao, Jiang-He Feng, and Jiang-Gao Mao. A Facile Route to Nonlinear Optical Materials: Three-Site Aliovalent Substitution Involving One Cation and Two Anions. *Angew. Chem. Int. Ed*. **2019**, 58, 2098 –2102.

101. Zhuang Li, Yi Yang, Yangwu Guo, Wenhao Xing, Xiaoyu Luo, Zheshuai Lin, Jiyong Yao, and Yicheng Wu. Broadening Frontiers of Infrared Nonlinear Optical Materials with π-Conjugated Trigonal-Planar Groups. *Chem. Mater*. **2019**, 31, 1110−1117.

102. Weiqun Lu, Zeliang Gao, Xitao Liu, Xiangxin Tian, Qian Wu, Conggang Li, Youxuan Sun, Yang Liu, and Xutang Tao. Rational Design of a LiNbO3-like Nonlinear Optical Crystal, Li2ZrTeO6, with High Laser-Damage Threshold and Wide Mid-IR Transparency Window. *J. Am. Chem. Soc*. **2018**, 140, 13089−13096.

103. Daniel E. Bugaris, and Hans-Conrad zur Loye. Materials Discovery by Flux Crystal Growth: Quaternary and Higher Order Oxides. *Angew. Chem. Int. Ed*. **2012**, 51, 3780 – 3811.

104. Christian A. Juillerat, Vladislav V. Klepov, Gregory Morrison, Kristen A. Pace and Hans-Conrad zur Loye. Flux crystal growth: a versatile technique to reveal the crystal chemistry of complex uranium oxides. *Dalton Trans*. **2019**, 48, 3162-3181.

Chapter 2. Experimental methods

In order to develop new oxysulfide materials for the structure-property research, this thesis focuses on the flux crystal growth method for the ease to incorporate more than one anion in the structure. In this work, all the samples were prepared in the fused silica tube under vacuum. Crystal structures, optical properties, and thermal stabilities were investigated, through single crystal X-ray diffraction (SCXRD), powder X-ray diffraction (PXRD), synchrotron X-ray diffraction (SXRD), UV-Vis-NIR diffuse reflectance spectroscopy (UV-Vis), and thermal gravimetric analysis (TGA).

2.1. Sample synthensis: flux growth method

2.2.1. Flux growth method

In this thesis, all the crystal samples were prepared using flux crystal growth method. The first step is to weigh stoichiometric reagents and fluxes into the crucible. The top of the crucible was closed with a cap, then removed the crucible to a sealed silica tube. The above steps must be operated in glove box, because the precusors were sensitive to the moisture. Then the silica tube was vacuated to 10 Pa then fused. The fused silica tube was heated at high temperature for several days. Finally, the producted were washed in distilled water under sonication, then the single crystals can be collected for the structural analysis.

2.2.2. Solid state synthesis

In this thesis, the polycrystalline samples were prepared using solid state synthesis. The starting reagents were weighed in a stoichiometric ratio. The mixture was ground, pelletized, sealed in silica tube under vacuum, and heated for several days. The quality of the polycrystalline samples was checked by PXRD. Polycrystalline of high purity was used for the further characterization.

2.2. X-ray diffraction

2.2.1. Single crystal X-ray diffraction

Structure determination of the single crystals was executed with a Rigaku XtaLab mini II diffractometer (Mo *Kα* radiation), as shown in Figure 2.1. The raw area detector data frames were reduced and corrected for absorption effects using the SAINT+ and SADABS programs. Final unit cell parameters were determined by least-squares refinement taken from the data set. The initial structural models were performed with the SHELX package, through the OLEX2 GUI.[1-3]

Figure 2.1. The picture of Single crystal X-ray Rigaku XtaLab mini II diffractometer

2.2.2. Powder X-ray diffraction

As an important technique to preliminarily characterize phase of materials, PXRD plays a significant role for structure research. Room temperature XRD data were collected from

Desktop X-ray Diffractometer MiniFlex (Rigaku), as shown in Figure 2.2. The machine equips a graphite monochromator and Cu Ka radiation (λ = 1.5418 Å) in 0.2° increments over the range 5°< 2θ <100° with scanning rate of 5°/min. In this situation, the beam of electrons come from the Cu-1*s* orbital.

Figure 2.2. The picture of Powder X-ray Diffractometer MiniFlex (Rigaku)

2.2.3. Synchrotron X-ray diffraction

SXRD is a very crucial technique to analyze materials with unknown phase efficiently due to their high energy. Synchrotron radiation is generated when charged particles, such as electrons, are accelerated radially. The high-speed charged particles circulate in ultra-high vacuum tubes, or storage rings, which is made of certain arrangement of magnets. The scheme of SXRD is shown in Figure 2.3. The diameter of the storage ring is usually hundreds of meters.

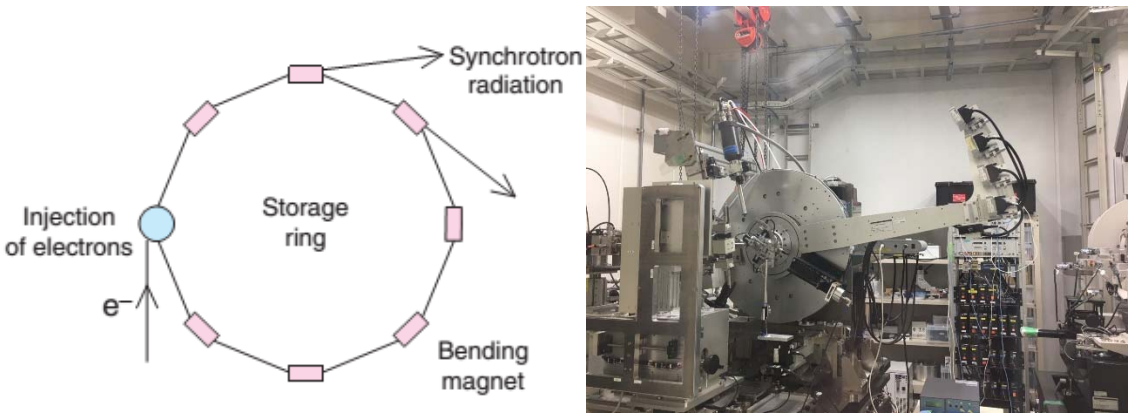

Figure 2.3. Schematic diagram of a synchrotron storage ring (left) and a picture of BL15XU in Spring-8(right).

In this thesis, SXRD measurements were caried out at room temperature using a one-dimensional detector installed on the NIMS BL15XU beamline at Spring-8 in Japan.[4,5] The synchrotron radiation X-rays were monochromatized to a wavelength of 0.65298 Å. A glass capillary tube (0.2 mm in internal diameter) was loaded with the polycrystalline samples. The diffraction data were analyzed by Rietveld refinement using the RIETAN-FP program.[6]

2.3. UV-Vis-NIR diffuse reflectance spectroscopy

UV-Vis spectra polycrystalline samples were carried out by a Shimazu UV- 2600 UV−Vis−NIR spectrometer (Figure 2.4) (used in the diffuse reflectance mode) equipped with an integrating sphere at the range of 220-1200 nm. Deuterium and halogen lamps were used as sources of UV and visible−NIR light, respectively. The recorded reflectance spectra were converted into the absorption data via the Kubelka−Munk function.[7]

Figure 2.4. The picture of Shimazu UV- 2600 UV−Vis−NIR spectrometer

2.4. Thermal gravimetric analysis

TGA observes the endothermic or exothermic behaviors when the sample undergoes phase transitions or chemical reaction. In this thesis, TGA of powder samples were performed using a Rigaku TG-DTA8188 system. The sample was loaded in an alumina crucible and heated up to elevated tempereature. The equipment is shown in Figure 2.5.

Figure 2.5. The picture of Rigaku TG-DTA8188 system

2.5. Magnetic properties measurement system (MPMS)

The magnetic properties of all samples were measured by MPMS-XL-7T (Quantum Design) as shown in Figure 2.6**.** The temperature dependent magnetic susceptibilities (χ) and field dependent isothermal magnetizations of all prepared samples were measured. The temperature dependent magnetic susceptibilities (χ) were measured under both field cooling (FC) and zero field cooling (ZFC) conditions in a temperature range 2 to 400 K under an applied magnetic field of 100 Oe and10 kOe. Initial negative magnetization on some ZFC curves could be caused by negative trapped fields inside a magnetometer or the sample insertion procedure.[8] The field dependence isothermal magnetizations were measured between +70 kOe and –70 kOe. The ac susceptibility was measured by using MPMS-1T (Quantum Design). The real parts (χ') and imaginary parts (χ'') were measured at different frequencies (f)

and different applied oscillating magnetic fields (H_{ac}).

Figure 2.6. The picture of MPMS-XL system

2.6. Other technologies used in this work.

2.6.1 SHG measurements

The powder SHG measurements were carried out by the Kurtz-Perry method using an incident laser beam (λ = 1064 nm) emitted from a Q-switched Nd:YAG laser.[9] Sintered polycrystalline sample was ground and sieved into distinct particle size ranges (38-55, 55-88, 88-105, 105-155, 155-200 μm). The intensities of the frequency-double output emitted from the sieved samples were KH_2PO_4 (KDP) was used as a benchmark material.

2.6.2 Photoluminescence (PL) and photoluminescence excitation (PLE) spectra

PL and PLE spectra were recorded at room temperature using a fluorescence spectrophotometer (Hitachi F-7000).

References in chapter 2

1. G. M. Sheldrick. SHELXT - Integrated space-group and crystal-structure determination. *Acta Cryst*. **2015**, A71, 3-8.

2. C. B. Hubschle, G. M. Sheldrick, B. Dittrich. ShelXle: a Qt graphical user interface for SHELXL. *J. Appl. Crystallogr*. **2011**, 44, 1281–1284.

3. O. V. Dolomanov, A. J. Blake, N. R. Champness, M. Schröder. OLEX: new software for visualization and analysis of extended crystal structures. *J. Appl. Crystallogr*. **2003**, 36, 1283–1284.

4. Tanaka, M.; Katsuya, Y.; Yamamoto, A. A new large radius imaging plate camera for high-resolution and high-throughput synchrotron X-ray powder diffraction by multiexposure method. *Rev. Sci. Instrum*. **2008**, 79(7), 075106.

5. Tanaka, M.; Katsuya, Y.; Matsushita, Y.; Sakata, O., Development of a synchrotron powder diffractometer with a one-dimensional X-ray detector for analysis of advanced materials. *J. Ceram. Soc. Jpn*. **2013**, 121 (1411), 287-290.

6. Izumi, F.; Momma, K. Three-Dimensional Visualization in Powder Diffraction. *Solid State Phenomena*. **2007**, 130, 15-20.

7. P Kubelka, and F Munk. An article on optics of paint layers. *Zeitschrift für Tech. Phys*. **1931**, 12, 593–601.

8. Zhang, L.; Terada, N.; Johnson, R. D.; Khalyavin, D. D.; Manuel, P.; Katsuya, Y.; Tanaka, M.; Matsushita, Y.; Yamaura, K.; Belik, A. A. High-pressure synthesis, structures, and properties of trivalent A-site-ordered quadruple perovskites RMn7O12 (R= Sm, Eu, Gd, and Tb). *Inorg. Chem*. **2018**, 57, 5987-5998.

9. S. K. Kurtz, and T. T. Perry. A Powder Technique for the Evaluation of Nonlinear Optical Materials. *J. Appl. Phys*. **1968**, 39, 3798–3813.

Chapter 3. Non-linear Optical Property of $La_3Ga_3Ge_2S_3O_{10}$ in Ultraviolet Region

3.1. Introduction

Nowadays, a lot of high technolegues, such as high-precision microfabrication, semiconductor mask inspection, ablative photodecomposition, request high-power and tightly focused UV lasers.[1] Currently, laser sources with required wavelengths below 300 nm in UV regions depend on excimer lasers, which use corrosive gas halides, such as XeCl, ArF, and KrF. These excimer lasers have various disadvantages including large volume, high-voltage gas discharge, and the requirement for regular maintenance, which limits the wide applications.[2] All-solid-state UV lasers, which have compacted dimensions and are maintenance-free, have drawn more and more attention with the combination of NLO single crystals.[3] The infrared lasers (typically 1064 nm for Nd:YAG lasers) can be easily converted to a UV frequency through sum-frequency generation by NLO single crystals. NLO single crystals also improve quality and power output of the high UV laser beams. Based on Chen's anionic group theory,[5] various novel UV NLO single crystals have been developed, such as β-BaB_2O_4 (β-BBO),[4,6] $KBe_2BO_3F_2$ (KBBF),[7] LiB_3O_5 (LBO),[8] and $CsLiB_6O_{10}$ (CBBO)[9]. However, there are still some challenges for practical applications in deep UV regions. The challenges include high SHG coefficients (d_{ij} > d_{36} (KDP) = 0.39 pm/V), wide UV transparency window, moderate birefringence (Δn ~0.07 – 0.10 at 1064 nm), thermal and chemical stability, as well large size single crystals.[10] In the past decades, this has prompted scientists to explore new materials. Various synthetic, theoretical and computational methods are also developed.[11]

In order to design novel UV NLO materials with wide optical transparent windows, the following two types of anionic groups have benn extensively studied based on Chen's anionic group theory: Π-conjugated NO_3^-, CO_3^{2-}, and BO_3^{3-},[12-16] as well as noncentral tetrahedral units

with polar atomic shifts, such as SO_4^{2-}, PO_4^{3-}, and BO_4^{5-} [17-21]. Recently, mixed-anion directed strategies, which combines more than one kind of anionic species in the structure, have attracted growing researching interests due to the enhanced optical properties for NLO materials.[22] Heteroleptic coordination environment around the cationic center, which is regarded as the optical functional building block units, leads to the improvement of polar atomic displacement in the units and further resulting in the rise of SHG responses. Halogen elements, which has higher electronegativity and polarizability than oxygen, have been successfully introduced into the practicable NLO single crystals and been reported of significant SHG performances and blue shifts in the absoption edges. KBBF-type fluoroborates AB_4O_6F (A = NH_4, Cs, Na, Rb)[23] and borate halides $AZn_2BO_3X_2$ (A = Na, K, Rb, Cs; X = F, Cl, Br)[24] as well as $KTiPO_4$-type fluoride sulfate $CsSbF_2SO_4$[25] have been developed and exhibited improved SHG properties than the model materials.

In contrast, chalcogenide ions (S, Se, Te) have been underexplored for UV applications.[26] This is due to the narrowing of the maximum band gap in their high-energy *p* orbitals in valance bands and the low phono energy in chalcogenides, which limits the applications in the visible or infrared regions.[27] There are many reports that mixing chalcogenides and oxide ions in one structure is a typical approach for finely adjusting the band gap. The S/O ratio of the functional unit is of great significance to the optical properties. In general, SHG coffcient increases with elevated S/O ratio, accompanied with narrower band gap. Table 3.1 summarizes some NLO oxysulfides,[28,29] including $AGeSe_2O$ (A = Sr, Ba) with $GeSe_2O_2$ tetrahedra (1.1–1.3 × AGS, E_g ~ 3.2 eV),[30,31] $SrZn_2S_2O$ with ZnS_2O_2 tetrahedra (2 × KDP, E_g = 3.89 eV),[32] and $Sr_6Cd_2Sb_6S_{10}O_7$ with SbS_4O and SbS_5 pyramids (4 × AGS, E_g = 1.89 eV)[33]. Although strong SHG intensities have been observed in the above oxychalcogenides, they can't be used in UV regions due to the narrow band gaps. It still remains a challenge to push the opto-transparent

window of the oxysulfide phases to the fourth or sixth HG wavelength of the Nd:YAG laser while maintaining a high SHG coefficient and appropriate birefringence.

Table 3.1. Comparison of the SHG intensities and band gaps of related

Composition	SHG intensity	Band gap (eV)	Ref.
$La_3Ga_3Ge_2S_3O_{10}$	2.0 × KDP	4.70	this work
$SrZn_2S_2O$	2.0 × KDP	3.86	32
$Na_{10}Cd(NO_3)_4(SO_3S)_4$	4.2 × KDP	3.74	18
$BaGeSe_2O$	1.1 × AGS	3.18	30
$SrGeSe_2O$	1.3 × AGS	3.2	31
$Sr_3Ge_2Se_3O_4$	0.8 × AGS	2.96	29
$Sr_6Cd_2Sb_6S_{10}O_7$	4× AGS	1.89	33
$Sr_4Pb_{1.5}Sb_5Se_8O_5$	0.25× AGS	0.92	28

In order to achieve both high SHG intensity and optical absorption cut-off edge in UV region in oxysulfide, we developed novel oxygen-rich oxysulfide, which consists of NLO active mixed-anion functional building block units. In this chapter, we report new UV NLO oxysulfide $La_3Ga_3Ge_2S_3O_{10}$. Comparing with the reported oxychalcogenides, it exhibits an exceptionally wide band gap of 4.70 eV, while retaining phase-matchable SHG property with twice intensity to that of KDP. The first-principles calculations reveal the contribution of $(Ga_{3/5}Ge_{2/5})_2O_7$ dimers and $^1_\infty[(Ga_{3/5}Ge_{2/5})_3S_3O_3]$ triangular tubes in the crystal structure. Anion-directed band gap engineering opens up the extension of oxychalcogenides to potential UV NLO materials.

3.2. Experimental details of Chapter 3

Reagents. La_2S_3 (Alfa Aesar, 99%), La_2O_3 (Rare Metallic, 99.9%), Ga_2O_3 (Rare Metallic, 99.9%), GeO_2 (Rare Metallic, 99.99%), Ge (High Purity Chemicals, 99.99%), S (High Purity Chemicals, 99.99%), $BaCl_2$ (Rare Metallic, 99.9%), and NaCl (Rare Metallic, 99.99%) were used as received. Before use, two chlorides were heated overnight in a dry oven at 260°C. All the raw materials were stored in an argon-filled glove box.

Crystal Growth. $La_3Ga_3Ge_2S_3O_{10}$ single crystals were prepared by $BaCl_2$-NaCl eutectic flux growth method. La_2S_3 (0.5mmol), Ga_2O_3 (0.5mmol), GeO_2 (0.5mmol), $BaCl_2$ (2.7mmol) and NaCl (4.0mmol) were placed into an alumina crucible in an Ar-filled glove box, The crucible was fused in a vacuum of 1Pa and sealed by flame in a quartz tube. The raw material was heated to 850℃ at 5℃/min in muffle furnace for 24 h and cooled to 550℃ at 0.08℃/min. Finally, the heater was turned off and cooled naturally to room temperature. The product was washed in sonicated water and extracted from flux. Colorless and transparent $La_3Ga_3Ge_2S_3O_{10}$ block crystal was prepared by vacuum filtration.

Solid State Reaction. $La_3Ga_3Ge_2S_3O_{10}$ polycrystalline powder samples were synthesized by stoichiometry ratio of La_2O_3 (3 mmol), Ga_2O_3 (3 mmol), GeO_2 (1 mmol), Ge (3 mmol) and S (6 mmol). The mixture was thoroughly ground with an agate mortar and pestle, pressed into pellets, sealed in a molten quartz tube at a vacuum value of 1pa, and then heated in a furnace at 850°C for 24 h.

Elemental Analysis. Elemental analysis of $La_3Ga_3Ge_2S_3O_{10}$ single crystals was performed by scanning electron microscopy (SEM) and energy dispersive X-ray (EDX) spectrometer (Oxford Instruments, Swift ED3000). Acceleration voltage was 15 keV.

Single-Crystal Structure Determination. The structure of $La_3Ga_3Ge_2S_3O_{10}$ single crystal was determined by Rigaku XtaLab Mini II diffractometer (Mo Kα radiation). Data collection covered 100% of reciprocal space $2\theta max = 26.312$ and Rint = 2.17% after absorption correction. Dual-space space algorithm (SHELXT) was used to solve the crystal structure, and Olex2 graphical user interface was used to optimize the crystal structure with SHELXT.

Laboratory X-ray Powder Diffraction. $La_3Ga_3Ge_2S_3O_{10}$ was confirmed to be pure phase by XRD test using Rigaku Miniflex-600 diffractometer (Cu Kα radiation).

Synchrotron X-ray Powder Diffraction and Rietveld Structure Refinement. SXRD measurements were made at room temperature using a one-dimensional detector mounted on the the NIMS BL15XU beamline at SPring-8 in Japan. Synchrotron radiation X-ray was

monochrome with A wavelength of 0.65298 Å. The $La_3Ga_3Ge_2S_3O_{10}$ polycrystalline sample was loaded on a glass capillary with an inner diameter of 0.2 mm. Diffraction data were collected in increments of 0.003 ◦ in the range 2-60 ◦ and analyzed using the Rietveld refined Rietan-FP program. Figure 3.3 shows the final results of Rietveld refinement on SXRD data based on a structural model obtained from single-crystal structure analysis. The experimental results are in good agreement with the calculated results. The final refined crystallization data are shown in Table 3.2.

Thermal Gravimetric Analysis. Thermogravimetric analysis (TGA) of $La_3Ga_3Ge_2S_3O_{10}$ powder samples was performed by Rigaku TG-DTA8188 system in a flowing O2 atmosphere (1.0 L/min). The samples were loaded into an alumina crucible and heated to 1000°C at 10°C/min.

UV-Vis-NIR Diffuse Reflectance Spectroscopy. The UV-Visible-NIR spectra of $La_3Ga_3Ge_2S_3O_{10}$ were measured by the Shimadzu UV-2600 UV-Visible-NIR spectrometer (for diffuse reflection mode) in the 220-1200 nm range. Deuterium lamp and halogen lamp served as ultraviolet and visible-near infrared light sources, respectively. The recorded reflection spectrum was converted into absorption data by the Kubelka−Munk function.

Powder SHG Measurements. The kurtz-Perry method was used to measure powder SHG using the incident laser beam emitted by the Q-switched Nd:YAG laser (λ = 1064 nm). Sintered polycrystalline $La_3Ga_3Ge_2S_3O_{10}$ samples were ground and sieved into different particle size ranges (38-55, 55-88, 88-105, 105-155, 155-200 μm). Using KH_2PO_4 (KDP) as reference material, the output intensity of frequency doubling of the sample was observed.

Computational Methods. CASTEP software package was adopted to carry out first-principles density functional theory (DFT) calculation by plane wave pseudopotential method. The generalized gradient approximation (GGA) based on the Perdew-Burke-Ernzerhof (PBE) function was adopted, and the cut-off limit of kinetic energy was set at 880 eV under the norm conservation pseudpotential. Monkhorst-Pack k-points sampling grid in Brillouin area set to

2×2×2. The automatic setting of the CASTEP code does not change the convergence conditions and other parameters when calculating the electronic properties. The orbital electrons of La-$5p^6 5d^1 6s^2$, Ga-$4s^2 4p^1$, Ge-$4s^2 4p^2$, S-$3s^2 3p^4$ and O-$2s^2 2p^4$ were treated as valence electrons. The linear optical and NLO characteristics of 1.3 eV are calculated by using the scissor operator correction, which are consistent with the band gap observed in the experiment. NLO coefficient was calculated by length specification formula. In order to study the source of NLO properties of $La_3Ga_3Ge_2S_3O_{10}$, SHG density method was used.

Calculation of the Distortion Index. The distortion index for GeO_4 and GeS_2O_2 tetrahedra was calculated using the following equation,

$$D = \frac{1}{n}\sum_{i=1}^{n}\left(\frac{|l_i - l_0|}{l_{av}}\right)$$

where l_i is the distance between the metal center and the i_{th} surrounding atom, and l_{av} is the average bond distance.

3.3. Results and discussion

3.3.1. Crystal Structure.

$La_3Ga_3Ge_2S_3O_{10}$ single crystal was successfully prepared by flux growth method via $BaCl_2$-NaCl mixture (Figure 3.1). The product was washed in sonicated water and extracted from flux. Colorless and transparent $La_3Ga_3Ge_2S_3O_{10}$ block crystals were collected through vacuum filtration, with typical size of 0.5×0.5×0.8 mm^3. Energy dispersive X-ray spectroscopy showed that the molar ratio of La/Ga/Ge/S was about 3.00/2.91/2.08/3.01(Figure 3.2), which was in good agreement with the chemical composition determined by single crystal structure analysis (CCDC Library No. 2110485)[34]. Polycrystalline powder samples can be synthesized as single phase using a conventional high-temperature reaction, with purity refined by Rietveld, using synchrotron powder X-ray diffraction data (Figure 3.3, Table 3.2).

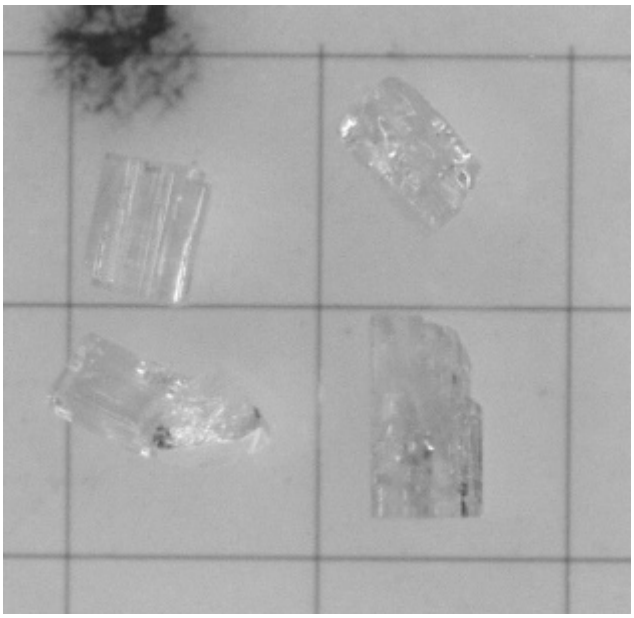

Figure 3.1. Photographs of single crystals of $La_3Ga_3Ge_2S_3O_{10}$ on a 1mm-grid glass plate.

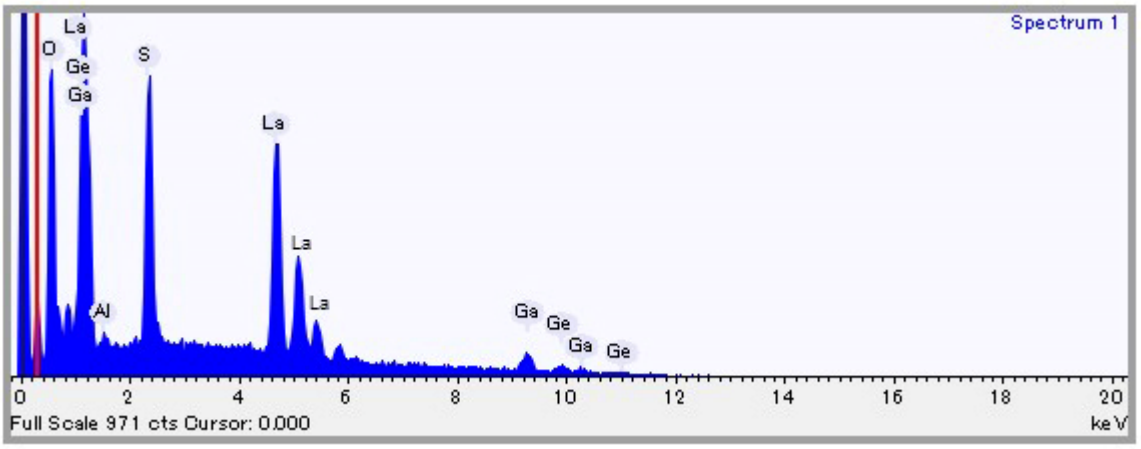

Figure 3.2. EDX analysis of $La_3Ga_3Ge_2S_3O_{10}$. The EDX analysis indicates that the molar ratio of La/Ga/Ge/S is 3.00/2.91/2.08/3.01, which is consistent with the result of single-crystal structure analysis.

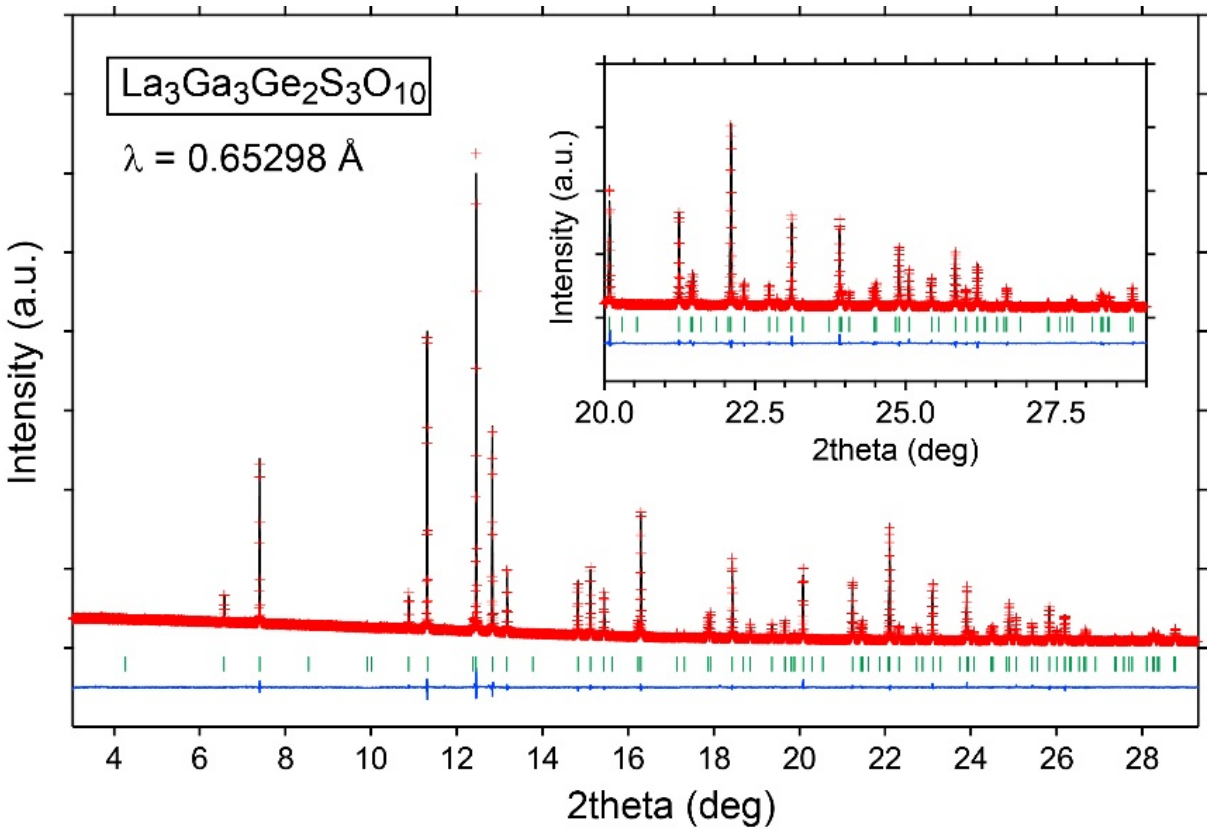

Figure 3.3. Synchrotron X-ray powder diffraction pattern collected from $La_3Ga_3Ge_2S_3O_{10}$ at room temperature. Rietveld refinements were performed using the SXRD data based on the structure model determined by single-crystal structure analysis. Obtained, calculated, and difference are presented by cross marks, upper solid lines, and bottom solid lines, respectively. The vertical lines represent the expected Bragg peak positions.

Table 3.2. Atomic Coordinates and Isotropic Displacement Parameters Refined against the SXRD Data Collected from $La_3Ga_3Ge_2S_3O_{10}$ at room temperature.

atom	site	*x*	*y*	*z*	occupancy	B_{equ}/ Å^2
La	6*h*	0.62002(6)	0.64252(7)	1/4	1	0.54(2)
Ga1	4*f*	2/3	1/3	-0.01280(24)	0.588	0.17(3)
Ge1	4*f*	2/3	1/3	-0.01280	0.412	0.17
Ga2	6*g*	0.81068(12)	0	1/2	0.608	0.71 (2)
Ge2	6*g*	0.81068	0	1/2	0.392	0.71
S	6*h*	0.6913(3)	0.0115(3)	3/4	1	1.00(7)

O1	2*c*	2/3	1/3	-1/4	1	1.6(3)
O2	6*g*	0.8244(5)	0.8244(5)	1/2	1	0.4(1)
O2	12*i*	0.6563(4)	0.4948(4)	0.0302(5)	1	0.5(1)

The space group is *P*-62*c* (No. 190) with $a = b = 10.12071$ (1) Å and $c = 7.48940$ (1) Å. The R factors are $R_{wp} = 2.35$ %, $R_B = 1.87$ %, and $R_F = 1.97$ %. All site occupancies were fixed to values obtained from the single-crystal structure analysis. Coordinates and B_{iso} values for Ga1/Ge1 and Ga2/Ge2 are independently constrained to the same values.

$La_3Ga_3Ge_2S_3O_{10}$ crystallizes in a noncentrosymmetric hexagonal space group *P*-62*c* (No.190) with lattice constants $a = 10.1406(5)$ Å, $c = 18.1645(9)$ Å. Ga/Ge (= M) site order has not been confirmed by structural refinement. This shows that Ga and Ge atoms are randomly distributed to the Wycoff position 4*f* and 6*g* in a 3:2 ratio. The asymmetric unit contains one La (6*h*), two M (4*f* and 6*g*), one S (6*h*), and three O sites (2*c*, 6*g*, and 12*i*) (Table 3.3-3.5). The crystal structure of $La_3Ga_3Ge_2S_3O_{10}$ is shown in Figure 4, as well as the local coordination environment around the metal center. $La_3Ga_3Ge_2S_3O_{10}$ crystallizes to form a unique three-dimensional structure, which is characterized by the coexistence of homoleptic and heteroleptic Ga/Ge coordination environments. The M1 atom at the 4*f* site tetrahehrally coordinates with four O atoms at $d_{M1\text{-}O1} = 1.7706(10)$ Å and $d_{M1\text{-}O3} = 1.736(5)$ Å (×3), indicating that tetrahedrons are uniaxially compressed along the *c*-axis (Table 3.6). The two $M1O_4$ tetrahedra form a separate dimer $(M1)_2O_7$, with O1 vertices shared. The M2 atom has tetrahedral coordination of two S and two O atoms at $d_{M2\text{-}S} = 2.2655(16)$ Å (×2) and $d_{M2\text{-}O2} = 1.859(3)$ Å (×2), respectively (Table S5). Compared with $M1O_4$ tetrahedron (D = 0.0089), M2S2O2 tetrahedron shows a larger distortion index[35] (D = 0.1005). The three $M2S_2O_2$ tetrahedra are connected by two common oxygen vertices to form a ternary ring $M2_3S_6O_3$ in the *ab* plane, which in turn shares two common sulfur vertices with its adjacent ternary ring along the *c*-axis to form a triangular tube $^1{}_\infty[M2_3S_3O_3]$. $M1O_4$ and $M2S_2O_2$ tetrahedra are separated by LaS_2O_6 square antiprisms ($d_{La\text{-}S} \sim 3.2275$ Å and $d_{La\text{-}O} \sim 2.5257$ Å on average), and

each tetrahedron has three common O atoms along the *c*-axis. In $M1O_4$, $M2S_2O_2$, and LaS_2O_6 polyhedra, the bond length between the metal and anion is consistent with the expected bond length for the sum of the ionic radii of each element[36]. However, the bond valence sum (BVS)[37] calculation of Ga and Ge sites suggests that there may be an ordered relationship between Ga/Ge site. Ga/Ge disordered model using single crystal structure analysis, obtained BVS of M1 and M2 sites are 3.91 and 3.07, inconsistent with the expected oxidation number respectively, while cationic ordered model Ga at 6*g* and Ge at 4*f* results in a more reasonable BVS of 2.95 for Ga and 4.02 for Ge. At this point, we cannot determine whether ordered $La_3Ga_3Ge_2S_3O_{10}$ has occurred because refinement of the ordered model using single-crystal X-ray diffraction data is unstable.

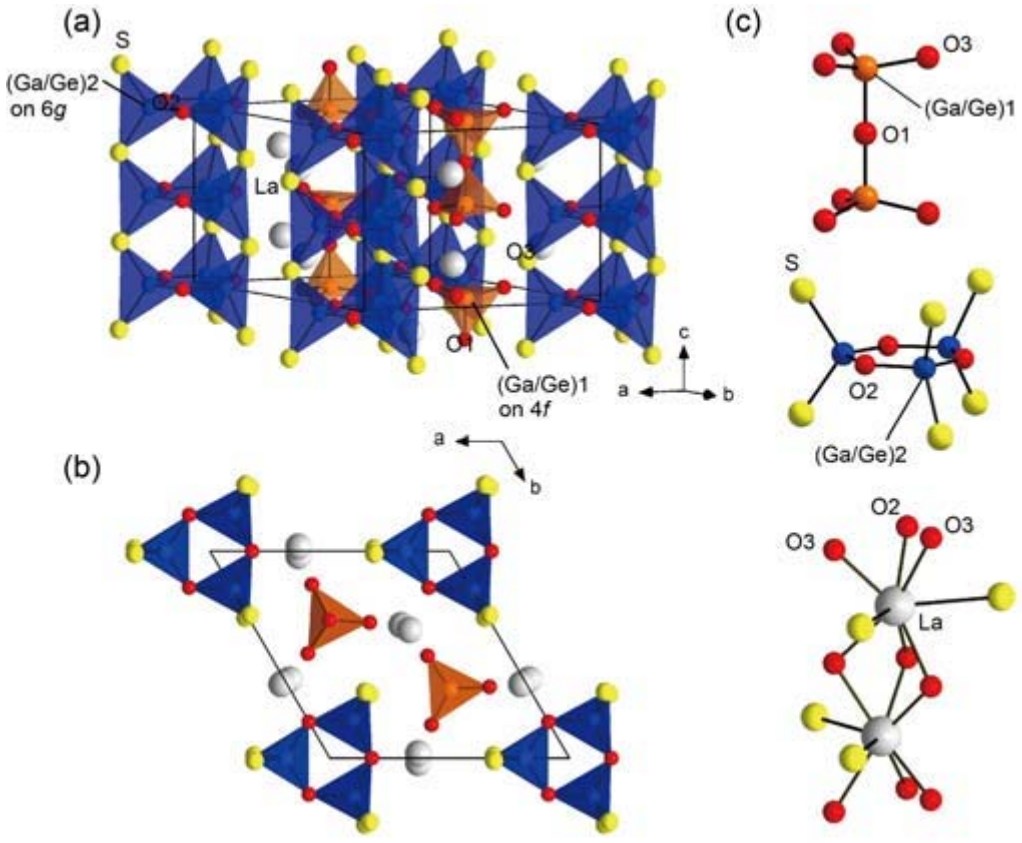

Figure 3.4. (a) Side and (b) top views of the crystal structure of $La_3Ga_3Ge_2S_3O_{10}$, which possesses triangular tubes and isolated dimers composed of $(Ga/Ge)S_2O_2$ and GaO_4 building blocks, respectively. (c) Local coordination environments around M1, M2, and La sites.

Table 3.3. Results of Structure Refinement of $La_3Ga_3Ge_2S_3O_{10}$ Using Single-Crystal XRD Data.

Formula	$La_3Ga_3Ge_2S_3O_{10}$
Formula weight	1027.25
Radiation	Mo Kα (λ=0.71073Å)
***T* (K)**	296
Crystal system	Hexagonal
Space group	*P*-62*c*
***a* (Å)**	10.1406(5)
***b* (Å)**	10.1406(5)
***c* (Å)**	7.5021(4)
***V* (Å^3)**	668.10(7)
Z	2
***D*$_{calc}$ (g/cm^3)**	5.106
***F*$_{000}$**	912
no. of measured reflns	1432
no. of unique reflns	470
no. of observed reflns ($F^2 > 2\sigma(F^2)$)	461
***R*$_{int}$ (%)**	1.83
$R[F^2 > 2\sigma(F^2)]/wR(F^2)$ (%)	1.81/4.07
GoF	1.061

Table 3.4. Structural Parameters for the Single Crystal of $La_3Ga_3Ge_2S_3O_{10}$.

atom	site	*x*	*y*	*z*	occupancy	U_{iso}/ Å^2
La	6*h*	0.61967(7)	0.64211(6)	1/4	1	0.0075(2)
Ga1	4*f*	2/3	1/3	-0.01398(13)	0.588	0.0033(3)
Ge1	4*f*	2/3	1/3	-0.01398	0.412	0.0030
Ga2	6*g*	0.81051(12)	0	1/2	0.608	0.0073(3)
Ge2	6*g*	0.81051	0	1/2	0.392	0.0073
S	6*h*	0.6918(3)	0.0123(3)	3/4	1	0.0101(6)
O1	2*c*	2/3	1/3	-1/4	1	0.029(4)

O2	6*g*	0.8235(7)	0.8235(7)	1/2	1	0.0111(17)
O3	12*i*	0.6551(6)	0.4949(6)	0.0327(7)	1	0.0117(11)

Table 3.5. Anisotropic Displacement Parameters Uij ($Å^2$) for $La_3Ga_3Ge_2S_3O_{10}$.

atom	U_{11}	U_{22}	U_{33}	U_{23}	U_{13}	U_{12}
La	0.0113(3)	0.0048(3)	0.0057(3)	0	0	0.0036(3)
Ga1	0.0023(4)	0.0023(4)	0.0051(6)	0	0	0.0012(2)
Ge1	0.0023(4)	0.0023(4)	0.0051(6)	0	0	0.0012(2)
Ga2	0.0064(5)	0.0051(5)	0.0099(5)	-0.0004(3)	-0.00018(16)	0.0025(3)
Ge2	0.0064(5)	0.0051(5)	0.0099(5)	-0.0004(3)	-0.00018(16)	0.0025(3)
S	0.0076(14)	0.0150(15)	0.0088(13)	0	0	0.0064(12)
O1	0.042(7)	0.042(7)	0.005(6)	0	0	0.021(3)
O2	0.006(3)	0.006(3)	0.018(4)	-0.0006(12)	0.0006(12)	0.001(3)
O3	0.016(3)	0.010(3)	0.015(2)	-0.0017(19)	0.001(2)	0.011(2)

Table 3.6. Selected Interatomic Distances (Å) and Bond Angles (°) of $La_3Ga_3Ge_2S_3O_{10}$.

	Bond distance(Å)		Bond angle **(°)**		Bond angle **(°)**
La-O3×2	2.356(5)	O3-La-O3	87.6(3)	O2-La-S×2	135.82(10)
La-O3×2	2.506(5)	O3-La-O3×2	71.8(2)	O3-La-S×2	132.77(13)
La-O2×2	2.715(5)	O3-La-O3×2	149.3(2)	O3-La-S×2	76.71(13)
La-S	3.211(3)	O3-La-O3	115.6(2)	O2-La-S×2	66.44(6)
La-S	3.244(2)	O3-La-O2×2	126.99(14)	S-La-S	130.91(7)
(Ga/Ge)1-O3×3	1.736(5)	O3-La-O2×2	69.25(15)	O3-Ga/Ge1-O3×3	116.04(12)
(Ga/Ge)1-O1	1.7706(10)	O3-La-O2×2	141.47(15)	O3-Ga/Ge1-O1×3	101.63(18)
(Ga/Ge)2-O2×2	1.859(3)	O3-La-O2×2	67.25(15)	O2-Ga/Ge2-O2	113.0(4)
(Ga/Ge)2-S×2	2.2655(16)	O2-La-O2	87.4(2)	O2-Ga/Ge2-S×2	110.39(11)
		O3-La-S×2	74.97(13)	O2-Ga/Ge2-	105.59(11)

			S×2	
	O3-La-S×2	77.72(12)	S-Ga/Ge2-S	112.04(12)

The crystal structure of $La_3Ga_3Ge_2S_3O_{10}$ can be regarded as a derivative of $A_3B_3C_2O_{13}$ (A = K, Rb; B = Nb, Ta, U; C = Si, Ge) in the same hexagonal space group (Figure 3.5)[38]. Here, sites B and C correspond to sites M2 and M1 of $La_3Ga_3Ge_2S_3O_{10}$. Oxysulfide phase and related oxide analogues adopt a common framework consisting of tetrahedral dimers and triangulated tubes. However, the B site in the oxide is in a nearly ideal octahedral coordination with the oxygen atom. Thus, the C_2O_7 dimer in these oxides and the $^1_\infty[B_3O_{12}]$ triangulated tubes are connected by a common oxygen vertex. In $La_3Ga_3Ge_2S_3O_{10}$, the asymmetric $^1_\infty[M23S_3O_3]$ triangulated tube composed of highly distorted $(Ga/Ge)S_2O_2$ tetrahedra will play an important role in the high SHG response.

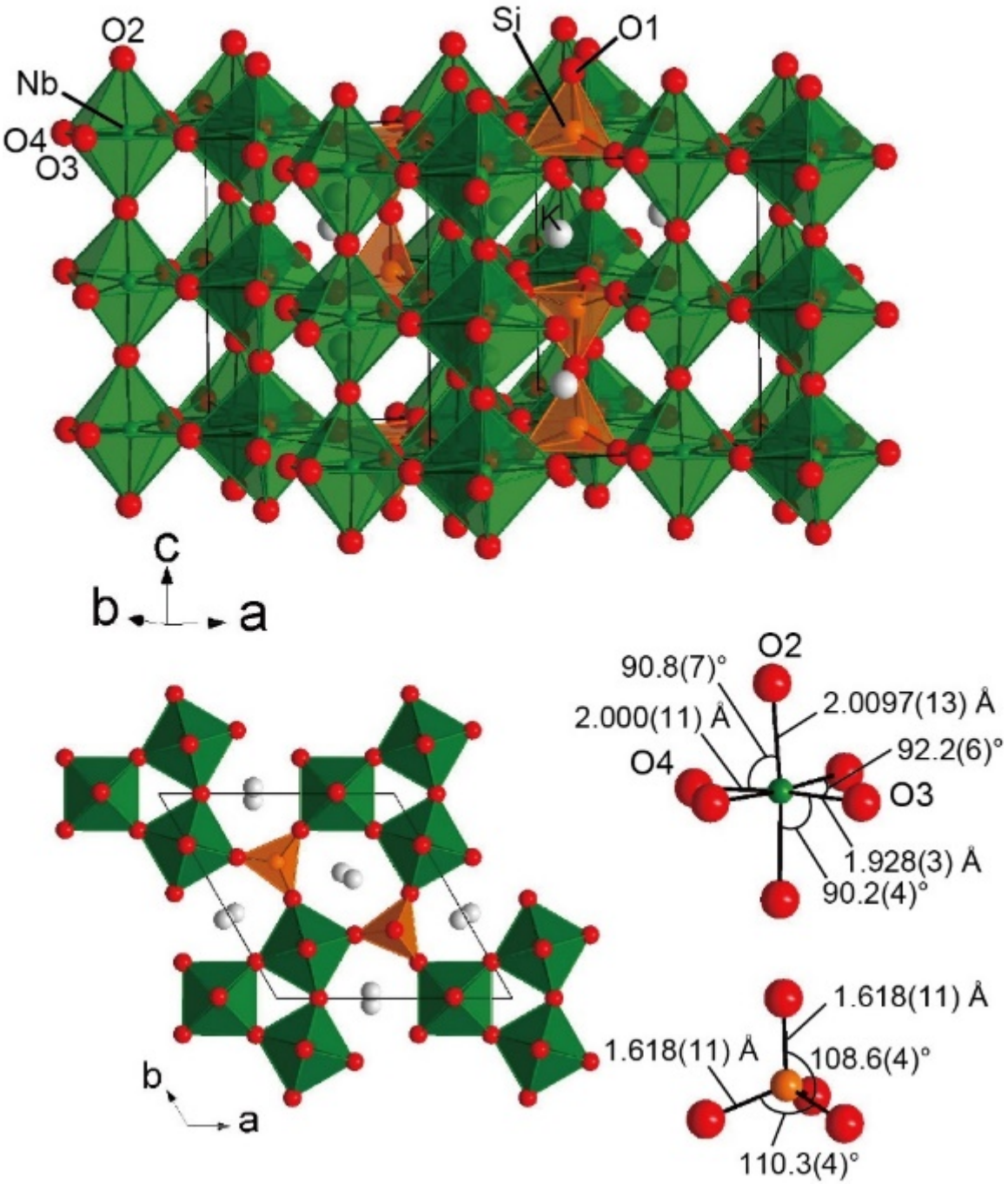

Figure 3.5. Schematic views of the crystal structure and local coordination environments around Nb/Si centers of $K_3Nb_3Si_2O_{13}$, which possesses triangular tubes and isolated dimers composed of NbO_6 and SiO_4 building blocks, respectively.

3.3.2. Thermal Stability of $La_3Ga_3Ge_2S_3O_{10}$.

The thermal stability of $La_3Ga_3Ge_2S_3O_{10}$ in a flowing oxygen atmosphere was studied using thermogravimetric and differential thermal analysis (TGA) measurements of powder samples

(Figure 3.6). At 800°C, the TG curve remained largely unchanged, but further heating to 1200°C resulted in a rapid increase in weight of about 3.5% at 950°C and only a small increase at 880°C. These behaviors are caused by the decomposition of the oxysulfide phase, as confirmed by XRD analysis after TG testing.

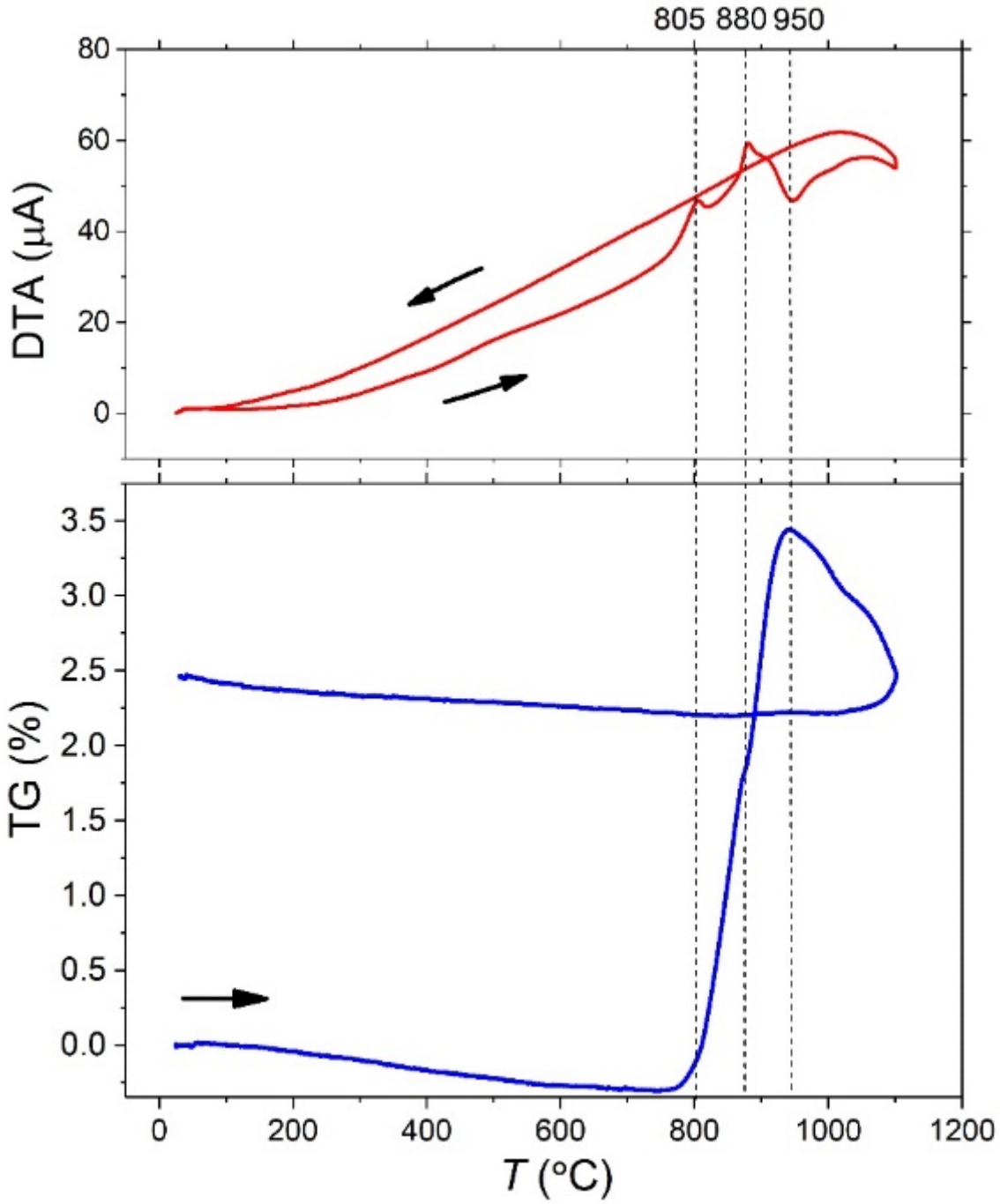

Figure 3.6. Thermogravimetric (TG) and differential thermal analysis (DTA) curves of $La_3Ga_3Ge_2S_3O_{10}$ in O_2 gas atmosphere. The DTA curves exhibited two exothermic peaks

and an endothermic peak corresponding to the anomalies observed in the TG curves, suggesting that complex decomposition processes take place.

3.3.3. UV-Vis Spectrum of $La_3Ga_3Ge_2S_3O_{10}$.

The UV-Vis diffuse reflectance and absorption spectra of $La_3Ga_3Ge_2S_3O_{10}$ are shown in Figure 3.7. These spectra have a UV cutoff edge of nearly 250 nm and a wide band gap of 4.70 eV. This band gap is very large compared to the reported NLO oxychalcogenide compound and also differs from these typical semiconductor oxides such as β-Ga_2O_3 and rutile GeO_2 (e.g. ~ 4.7eV),[39,40] which is much wider than the oxide analogue of $K_3Ta_3Si_2O_{13}$(e.g. = 4.2 eV)[41]. One possible reason for the larger oxysulfide band gap in this study is that all sulfur atoms share a metal center with oxygen atoms, which inhibits upward movement of the maximum valence band (VBM), which is occupied by the S-3*p* orbital compared to the full sulfide coordination. However, the existence of large band gap energy cannot be explained only by considering the heteroleptic coordination environment. In fact, the optical band gap of reported NLO oxychalcogenide compounds is less than 4 ev, and most of them have building blocks containing O and Q anions. Another important consideration is the molar ratio in the $La_3Ga_3Ge_2S_3O_{10}$, which is much higher than other NLO oxychalcogenides. The oxygen-rich concentration not only weakens the interaction between metal centers, but it also stabilizes the all-oxide coordinated environment $(Ga/Ge)O_4$ to improve UV transparency.

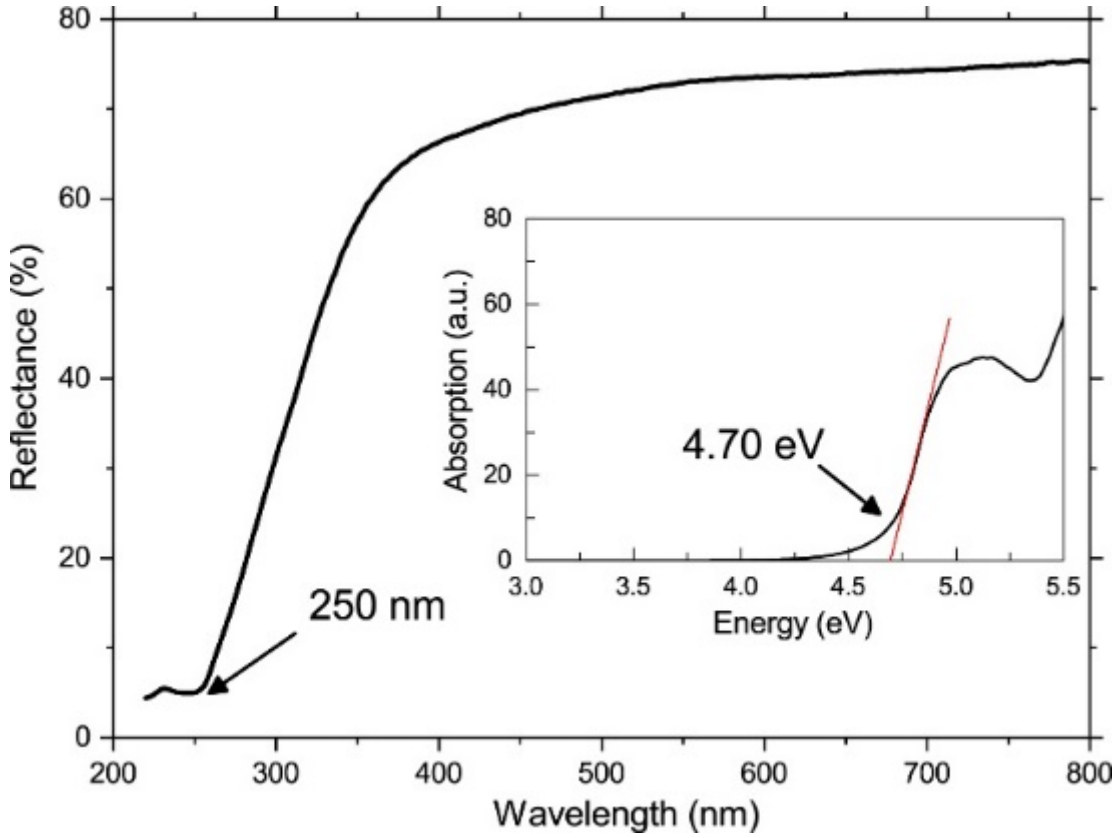

Figure 3.7. UV-Vis diffuse reflectance and absorption spectra of $La_3Ga_3Ge_2S_3O_{10}$.

3.3.4. Non-linear Optical Property of $La_3Ga_3Ge_2S_3O_{10}$.

According to the Kurtz-Perry method, the SHG response of $La_3Ga_3Ge_2S_3O_{10}$ was measured at λ = 1064 nm, using KDP as reference. Figure 3.8 shows the variation curve of SHG intensity of $La_3Ga_3Ge_2S_3O_{10}$ powder with particle size. In the region with small particle size, the SHG strength of $La_3Ga_3Ge_2S_3O_{10}$ increases with the increase of particle size, and reaches a plateau in the region larger than 125 mm. These behaviors indicate that $La_3Ga_3Ge_2S_3O_{10}$ satisfies the type-I phase matching condition. The SHG strength of $La_3Ga_3Ge_2S_3O_{10}$ is 2.0 times that of the reference KDP in the particle size range of 150−200 μm. The observed intensity of SHG is comparable to $SrZn_2S_2O$, which contains more sulfur atoms per formula unit.

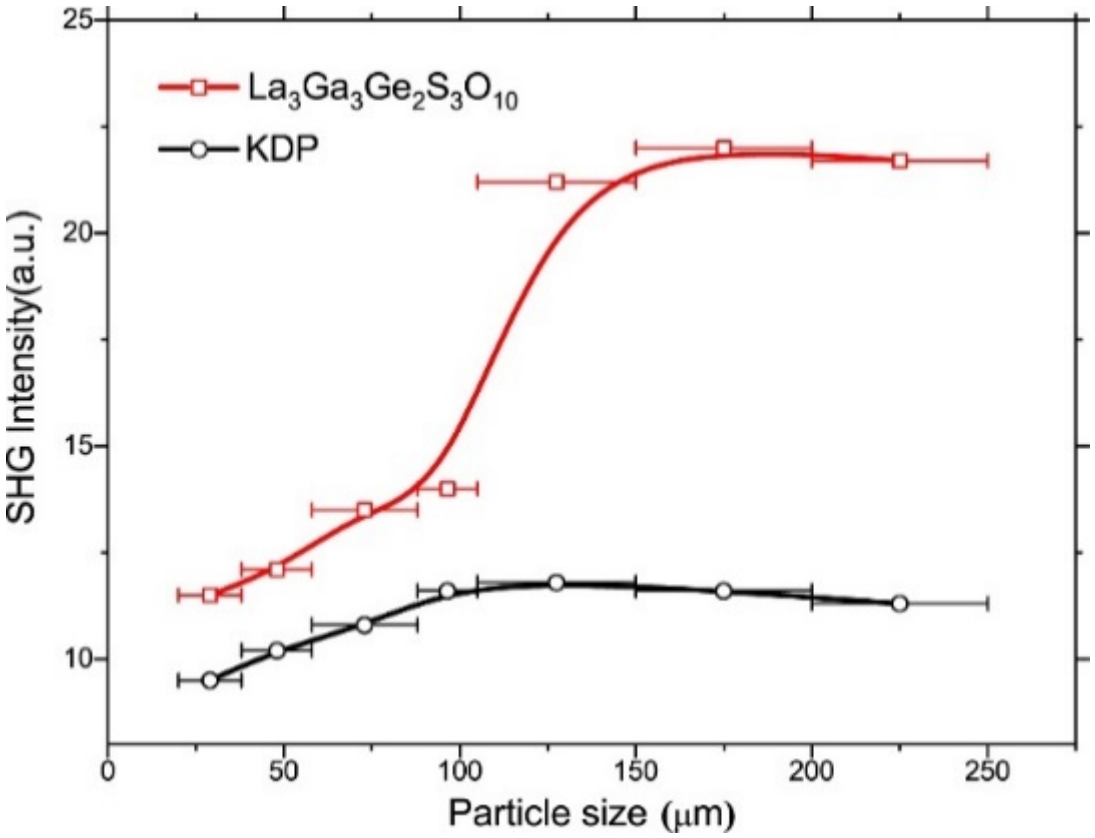

Figure 3.8. Plot of SHG intensity vs particle size at λ = 1064 nm. The solid curves are drawn as guides to the eyes.

3.3.5. Theoretical Calculation.

In order to better understand the relationship between electronic structure and optical properties, the plane wave pseudopotential method was used to perform first-principles calculations. Since it is not possible to directly calculate the mixed occupancy of Ga/Ge sites using first-principles calculations, a model with Ga/Ge atoms at the 6*g*/4*f* site, the possible ordered model discussed earlier, is used. Figure 3.9 shows the calculated total and partial state densities (DOS) and band structure of $La_3Ga_3Ge_2S_3O_{10}$. The band structure shows that the oxide sulfide phase is an indirect band gap semiconductor, Eg = 3.10 eV, less than the experimental value of UV-Vis spectrum. DFT calculations tend to underestimate band gaps due to the discontinuity of the exchange correlation energy. Part of DOS shows that La-5*d* and Ga-4*s*, *p* orbitals mainly occupy the minimum conduction band orbital (CBM). VBM is

mainly composed of S-3*p* and O-2*p* orbitals. The S-3*p* orbitals dominate in the high energy region, while the O-2*p* orbitals dominate in the low energy region, which is common in oxysulfide.

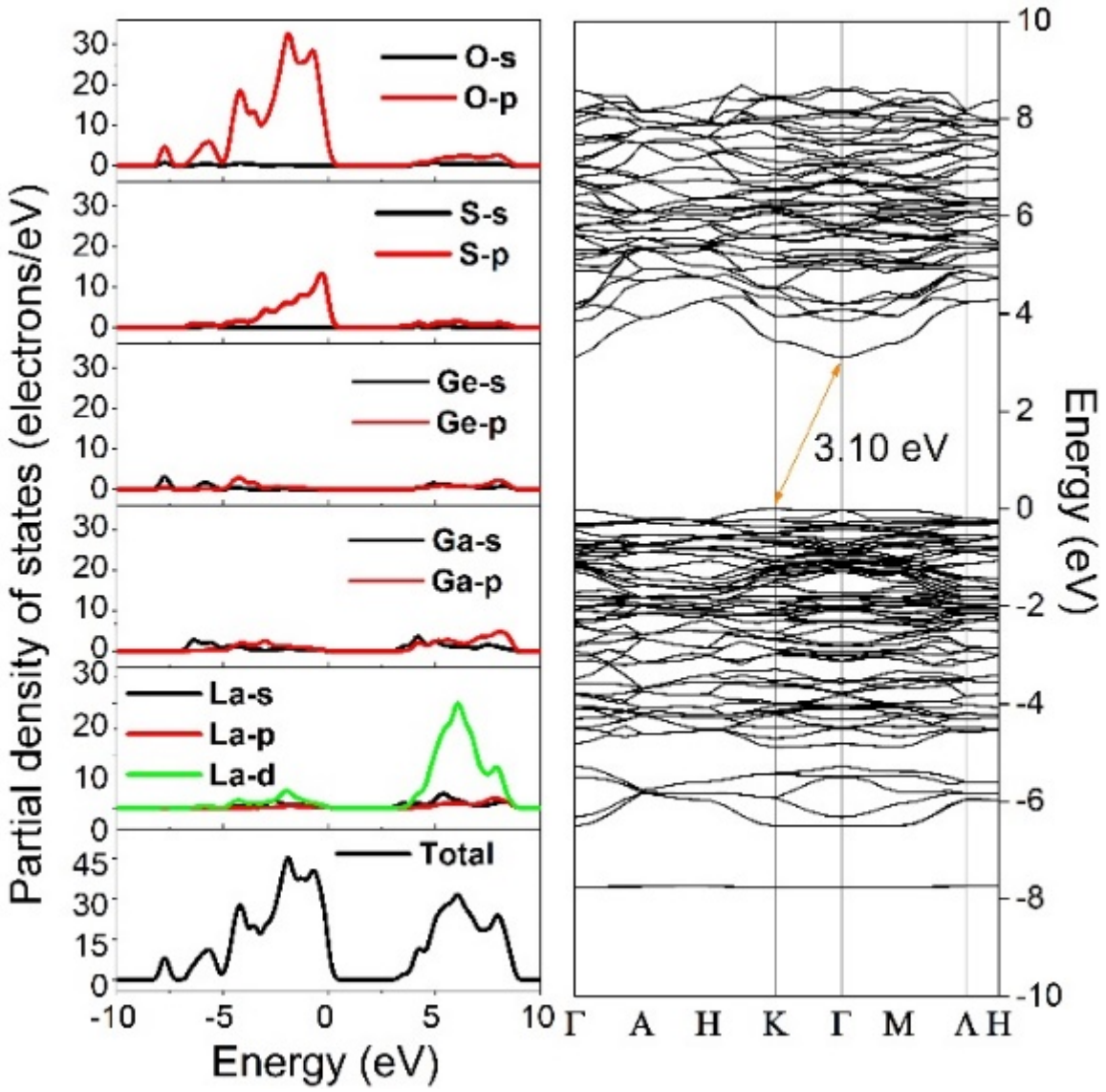

Figure 3.9. Partial and total density of states (right) and the band structure (left) of $La_3Ga_3Ge_2S_3O_{10}$.

For the space group *P*-62*c*, only two non-zero SHG coefficients d_{16} and d_{22} are allowed due to Kleiman symmetry. The calculated SHG coefficient of $La_3Ga_3Ge_2S_3O_{10}$ is $d_{22} = - d_{16}$ = 0.598 pm /V, which is in good agreement with the observed SHG intensity (2.0 × KDP). The birefringence at 1064 nm is 0.11, which is consistent with the matching ability of

oxysulfide phase. As shown in Figure 3.10, combining the band-resolved analysis[42] of d_{22} with the partial DOS made a significant contribution of the O-2*p* and S-3*p* orbitals and SHG response in the occupied state, while the La-5*d* orbital was also found to have a moderate contribution to the SHG response at unoccupied state. This can be confirmed by the SHG-weighted density diagram of d_{22} in occupied and unoccupied electron states (Figure 3.11), in which the SHG density of S-3*p* orbital is dominant, followed by that of O-2*p* orbital. Therefore, we can conclude that both $M1O_4$ and $M2S_2O_2$ tetrahedrons in $La_3Ga_3Ge_2S_3O_{10}$ are responsible for the observed high SHG response.

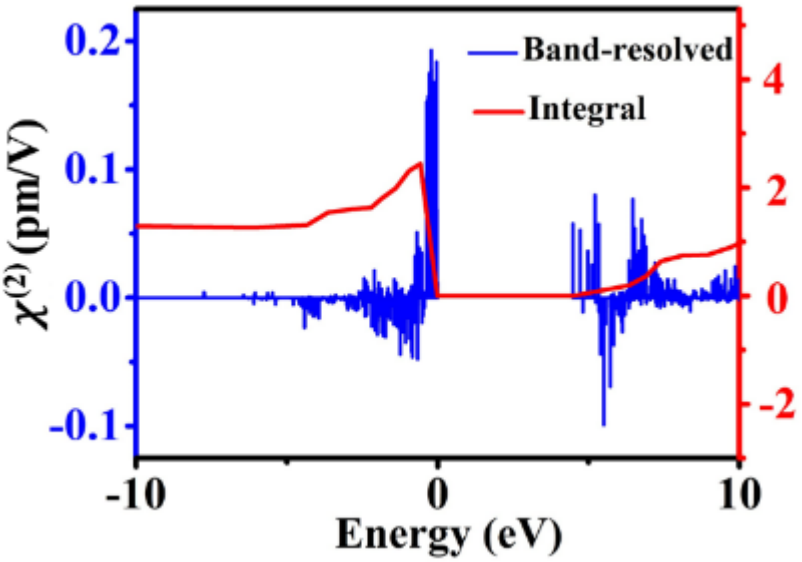

Figure 3.10. Band-resolved NLO susceptibility $\chi^{(2)}$ (= $2d_{22}$) and its integral for $La_3Ga_3Ge_2S_3O_{10}$.

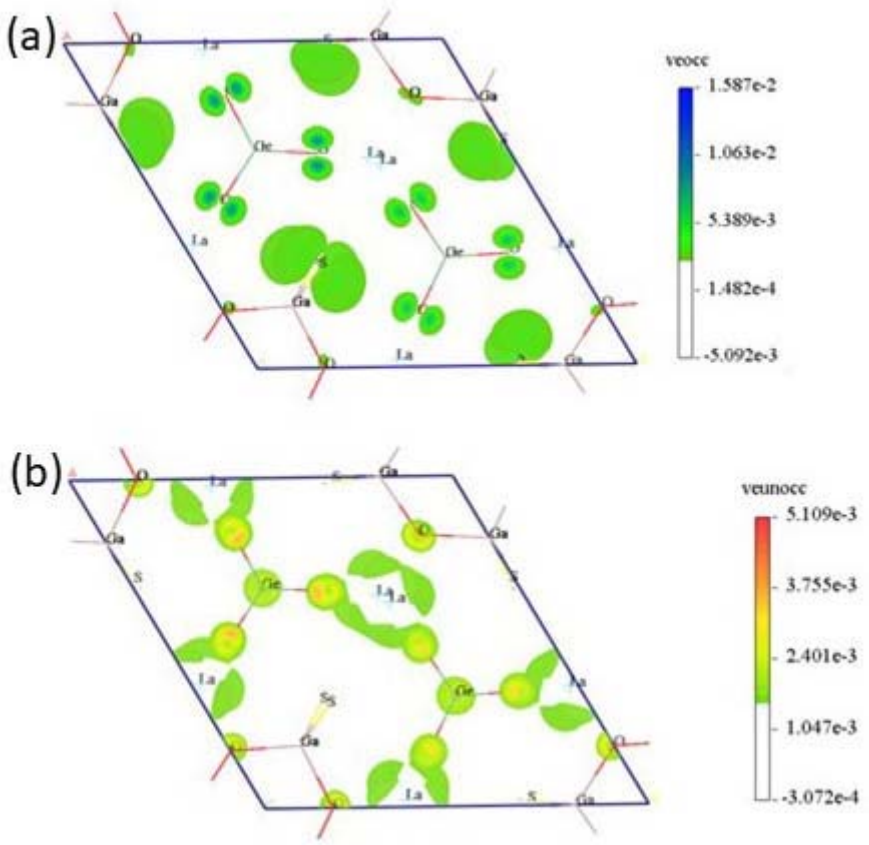

Figure 3.11. SHG density maps of $\chi^{(2)}$ for $La_3Ga_3Ge_2S_3O_{10}$ in the (a) occupied and (b) unoccupied electronic states.

3.4. Summary of Chapter 3

In summary, we discovered a new nonlinear optical oxygen-rich oxysulfide $La_3Ga_3Ge_2S_3O_{10}$ using the crystal growth method via $BaCl_2$-NaCl molten salt. The formation of 1D $^1{}_\infty[(Ga_{3/5}Ge_{2/5})_3S_3O_3]$ triangular tubes and 0D $(Ga_{3/5}Ge_{2/5})_2O_7$ dimers in homoleptic and heteroleptic Ga/Ge coordination environments make SHG reaction twice that of KDP. The observed large band gap (4.70 eV), high SHG intensity, and phase matching behavior at 1064 nm of the oxysulfide suggest that the sulfur anion, which possesses large polarizability but high energy levels compared with oxygen anions, can be a promising element in high-power UV nonlinear optical materials. Considering the structure of $La_3Ga_3Ge_2S_3O_{10}$, it is satisfies the lack of all-sulfide coordination environment and the existence of total oxide coordination

environment in order to achieve high transparency of ultraviolet region. The remaining large SHG response mainly comes from the S-3*p* orbital. Using other building blocks such as $(BO_3)^{3-}$ and $(PO_4)^{5-}$, rather than $(Ga/Ge)O_4$, it will be helpful to further push the oxysulfide phases into the UV or deep UV region.

References in chapter 3

1. a) J. Lin, Z. Peng, Y. Liu, F. Ruiz-Zepeda, R. Ye, E. L. G. Samuel, M. J. Yacaman, B. I. Yakobson, J. M. Tour. Laser-induced porous graphene films from commercial polymers. *Nat. Commun*. **2014**, 5, 5714; b) T. C. Chong, M. H. Hong, L. P. Shi. Laser precision engineering: from microfabrication to nanoprocessing. *Laser Photon. Rev*. **2010**, 4, 123–143; c) B. Wu, A. Kumar. Extreme ultraviolet lithography and three dimensional integrated circuit—A review. *Appl. Phys. Rev*. **2014**, 1, 011104; d) J. Parrish, T. Deutsch. Laser photomedicine. *IEEE J. Quantum Electron*. **1984**, 20, 1386–1396.
2. T. Sasaki, Y. Mori, M. Yoshimura, Y. K. Yap, T. Kamimura. Recent development of nonlinear optical borate crystals: key materials for generation of visible and UV light. *Mater. Sci. Eng. R Reports*. **2000**, 30, 1–54.
3. H. Xuan, H. Igarashi, S. Ito, C. Qu, Z. Zhao, Y. Kobayashi. High-Power, Solid-State, Deep Ultraviolet Laser Generation. *Appl. Sci*. **2018**, 8, 233.
4. G. M. Y. C. T. Chen, B. C. Wu, A. D. Jiang. A NEW-TYPE ULTRAVIOLET SHG CRYSTAL——β-BaB2O4. *Sci. Sin. B*. **1985**, 28, 235–243.
5. N. Ye, Q. Chen, B. Wu, C. Chen. Searching for new nonlinear optical materials on the basis of the anionic group theory. *J. Appl. Phys*. **1998**, 84, 555–558.
6. M. Mutailipu, K. R. Poeppelmeier, S. Pan. Borates: a rich source for optical materials. *Chem. Rev*. **2021**, 121, 1130–1202.
7. L. Mei, Y. Wang, C. Chen, B. Wu. Nonlinear optical materials based on MBe2BO3F2 (M=Na,K). *J. Appl. Phys*. **1993**, 74, 7014–7015.

8. C. Chen, Y. Wu, A. Jiang, B. Wu, G. You, R. Li, S. Lin. New nonlinear-optical crystal: LiB3O5. *J. Opt. Soc. Am. B*. **1989**, 6, 616-621.

9. Y. Mori, I. Kuroda, S. Nakajima, T. Sasaki, S. Nakai. New nonlinear optical crystal: cesium lithium borate. *Appl. Phys. Lett*. **1995**, 67, 1818–1820.

10. P. S. Halasyamani, W. Zhang. Inorganic materials for UV and deep-UV nonlinear-optical applications. *Inorg. Chem*. **2017**, 56, 12077–12085.

11. a) L. Kang, F. Liang, X. Jiang, Z. Lin, C. Chen. First-Principles Design and Simulations Promote the Development of Nonlinear Optical Crystals. *Acc. Chem. Res*. **2020**, 53, 209–217; b) D. Lin, M. Luo, C. Lin, F. Xu, N. Ye. KLi(HC3N3O3)·2H2O: Solvent-drop Grinding Method toward the Hydro-isocyanurate Nonlinear Optical Crystal. *J. Am. Chem. Soc*. **2019**, 141, 3390–3394, c) B. H. Lei, Z. Yang, H. Yu, C. Cao, Z. Li, C. Hu, K. R. Poeppelmeier, S. Pan. Module-guided design scheme for deep-ultraviolet nonlinear optical materials. *J. Am. Chem. Soc*. **2018**, 140, 10726–10733; d) B. Zhang, X. Zhang, J. Yu, Y. Wang, K. Wu, M.-H. Lee. First-principles high-throughput screening pipeline for nonlinear optical materials: Application to borates. *Chem. Mater*. **2020**, 32, 6772–6779.

12. T. T. Tran, J. Young, J. M. Rondinelli, P. S. Halasyamani. Mixed-metal carbonate fluorides as deep-ultraviolet nonlinear optical materials. *J. Am. Chem. Soc*. **2017**, 139, 1285–1295.

13. M. Luo, C. Lin, G. Zou, N. Ye, W. Cheng. Sodium–rare earth carbonates with shorite structure and large second harmonic generation response. *CrystEngComm*. **2014**, 16, 4414–4421.

14. L. Huang, G. Zou, H. Cai, S. Wang, C. Lin, N. Ye. Sr 2 (OH) 3 NO 3: the first nitrate as a deep UV nonlinear optical material with large SHG responses. *J. Mater. Chem. C*. **2015**, 3, 5268–5274.

15. R. Liu, H. Wu, H. Yu, Z. Hu, J. Wang, Y. Wu. K5Mg2La3(BO3)6: An Efficient, Deep-

Ultraviolet Nonlinear Optical Material. *Chem. Mater*. **2021**, 33, 4240–4246.

16. H. Yu, H. Wu, S. Pan, Z. Yang, X. Hou, X. Su, Q. Jing, K. R. Poeppelmeier, J. M. Rondinelli. Cs3Zn6B9O21: A Chemically Benign Member of the KBBF Family Exhibiting the Largest Second Harmonic Generation Response. *J. Am. Chem. Soc*. **2014**, 136, 1264–1267.

17. Y. Li, F. Liang, S. Zhao, L. Li, Z. Wu, Q. Ding, S. Liu, Z. Lin, M. Hong, J. Luo. Two non-π-conjugated deep-UV nonlinear optical sulfates. *J. Am. Chem. Soc*. **2019**, 141, 3833–3837.

18. Y. Liu, Y. Liu, Z. Lin, Y. Li, Q. Ding, X. Chen, L. Li, S. Zhao, M. Hong, J. Luo. Nonpolar Na10Cd(NO3)4(SO3S)4 Exhibits a Large Second-Harmonic Generation. *CCS Chem*. **2021**, 3, 694–699.

19. Q. Ding, X. Liu, S. Zhao, Y. Wang, Y. Li, L. Li, S. Liu, Z. Lin, M. Hong, J. Luo. Designing a deep-UV nonlinear optical fluorooxosilicophosphate. *J. Am. Chem. Soc*. **2020**, 142, 6472–6476.

20. C. Wu, L. Li, L. Lin, Z. Huang, M. G. Humphrey, C. Zhang. Gd (NO 3)(Se 2 O 5)· 3H 2 O: a nitrate–selenite nonlinear optical material with a short ultraviolet cutoff edge. *Dalt. Trans*. **2020**, 49, 3253–3259.

21. J. H. Feng, C. L. Hu, H. P. Xia, F. Kong, J. G. Mao. Li7(TeO3)3F: A Lithium Fluoride Tellurite with Large Second Harmonic Generation Responses and a Short Ultraviolet Cutoff Edge. *Inorg. Chem*. **2017**, 56, 14697–14705.

22. M. Mutailipu, M. Zhang, Z. Yang, S. Pan. Targeting the next generation of deep-ultraviolet nonlinear optical materials: Expanding from borates to borate fluorides to fluorooxoborates. *Acc. Chem. Res*. **2019**, 52, 791–801.

23. a) Z. Zhang, Y. Wang, B. Zhang, Z. Yang, S. Pan. Polar Fluorooxoborate, NaB4O6F: A Promising Material for Ionic Conduction and Nonlinear Optics. *Angew. Chem. Int. Ed*. **2018**, 57, 6577–6581; b) X. Wang, Y. Wang, B. Zhang, F. Zhang, Z. Yang, S. Pan.

CsB4O6F: A Congruent‐Melting Deep‐Ultraviolet Nonlinear Optical Material by Combining Superior Functional Units. *Angew. Chem. Int. Ed*. **2017**, 56, 14119–14123; c) G. Shi, Y. Wang, F. Zhang, B. Zhang, Z. Yang, X. Hou, S. Pan, K. R. Poeppelmeier. Finding the Next Deep-Ultraviolet Nonlinear Optical Material: NH4B4O6F. *J. Am. Chem. Soc*. **2017**, 139, 10645–10648; d) Y. Wang, B. Zhang, Z. Yang, S. Pan. Cation‐Tuned Synthesis of Fluorooxoborates: Towards Optimal Deep‐Ultraviolet Nonlinear Optical Materials. *Angew. Chem. Int. Ed*. **2018**, 57, 2150–2154.

24. a) J. Zhou, Y. Liu, H. Wu, H. Yu, Z. Lin, Z. Hu, J. Wang, Y. Wu. CsZn2BO3X2 (X2=F2, Cl2, and FCl): A Series of Beryllium‐Free Deep‐Ultraviolet Nonlinear‐Optical Crystals with Excellent Properties. *Angew. Chem. Int. Ed*. **2020**, 59, 19006–19010. b) Q. Huang, L. Liu, X. Wang, R. Li, C. Chen. Beryllium-Free KBBF Family of Nonlinear-Optical Crystals: AZn2BO3X2 (A = Na, K, Rb; X = Cl, Br). *Inorg. Chem*. **2016**, 55, 12496– 12499.

25. X. Dong, L. Huang, C. Hu, H. Zeng, Z. Lin, X. Wang, K. M. Ok, G. Zou. CsSbF2SO4: An Excellent Ultraviolet Nonlinear Optical Sulfate with a KTiOPO4 (KTP)‐type Structure. *Angew. Chemie Int. Ed*. **2019**, 58, 6528–6534.

26. H. Kageyama, K. Hayashi, K. Maeda, J. P. Attfield, Z. Hiroi, J. M. Rondinelli, K. R. Poeppelmeier. Expanding frontiers in materials chemistry and physics with multiple anions. *Nat Commun*. **2018**, 9, 772.

27. a) Y.-F. Shi, W.-B. Wei, X.-T. Wu, H. Lin, Q.-L. Zhu. Recent progress in oxychalcogenides as IR nonlinear optical materials. Dalton Trans. 2021, 4112–4118; b) A. Abudurusuli, J. Li, S. Pan. A review on the recently developed promising infrared nonlinear optical materials. *Dalton Trans*. **2021**, 50, 3155–3160.

28. Y. Wang, M. Luo, P. Zhao, X. Che, Y. Cao, F. Huang. Sr 4 Pb 1.5 Sb 5 O 5 Se 8: a new mid-infrared nonlinear optical material with a moderate SHG response. *CrystEngComm*. **2020**, 22, 3526–3530.

29. W. Xing, P. Fang, N. Wang, Z. Li, Z. Lin, J. Yao, W. Yin, B. Kang. Two Mixed-Anion Units of [GeOSe3] and [GeO3S] Originating from Partial Isovalent Anion Substitution and Inducing Moderate Second Harmonic Generation Response and Large Birefringence. *Inorg. Chem*. **2020**, 59, 16716–16724.

30. B. W. Liu, X. M. Jiang, G. E. Wang, H. Y. Zeng, M. J. Zhang, S. F. Li, W. H. Guo, G. C. Guo. Oxychalcogenide BaGeOSe2: Highly Distorted Mixed-Anion Building Units Leading to a Large Second-Harmonic Generation Response. Chem. Mater. 2015, 27, 8189–8192.

31. M.-Y. Ran, Z. Ma, H. Chen, B. Li, X.-T. Wu, H. Lin, Q.-L. Zhu. Partial Isovalent Anion Substitution to Access Remarkable Second-Harmonic Generation Response: A Generic and Effective Strategy for Design of Infrared Nonlinear Optical Materials. *Chem. Mater*. **2020**, 32, 5890-5896.

32. Y. Tsujimoto, C. A. Juillerat, W. Zhang, K. Fujii, M. Yashima, P. S. Halasyamani, H. C. Zur Loye. Function of Tetrahedral ZnS3O Building Blocks in the Formation of SrZn2S2O: A Phase Matchable Polar Oxysulfide with a Large Second Harmonic Generation Response. *Chem. Mater*. **2018**, 30, 6486–6493.

33. R. Q. Wang, F. Liang, F. K. Wang, Y. W. Guo, X. Zhang, Y. Xiao, K. J. Bu, Z. S. Lin, J. Y. Yao, T. Y. Zhai, F. Q. Huang. Sr6Cd2Sb6O7S10: Strong SHG Response Activated by Highly Polarizable Sb/O/S Groups. *Angew. Chem. Int. Ed*. **2019**, 58, 8078–8081.

34. Crystallograhic details are available on CCDC. The CCDC depository number is 2110485.

35. W. H. Baur. The geometry of polyhedral distortions. Predictive relationships for the phosphate group. Acta Crystallogr. Sect. B Struct. Crystallogr. Cryst. Chem. 1974, 30, 1195–1215.

36. R. D. Shannon. Revised effective ionic radii and systematic studies of interatomic distances in halides and chalcogenides. Acta Crystallogr. Sect. A 1976, 32, 751– 767.

37. N. E. Brese, M. O'Keeffe. *Acta Crystallogr. Sect. B Struct. Sci*. **1991**, 47, 192–197.

38. a) C.-H. Lin, C.-S. Chen, A. A. Shiryaev, Y. V. Zubavichus, K.-H. Lii. K3(U3O6)(Si2O7) and Rb3(U3O6)(Ge2O7): A Pentavalent-Uranium Silicate and Germanate. *Inorg. Chem*. **2008**, 47, 4445–4447; b) S. Jaulmes, S. Launay, P. Mahé, M. Quarton. Silicatoniobate de potassium, K3Nb3O6Si2O7. *Acta Crystallogr. Sect. C Cryst. Struct. Commun*. **1995**, 51, 794–796; c) J. Choisnet, N. Nguyen, D. Groult, B. Raveau. De nouveaux oxydes a reseau forme d'octaedres NbO6 (TaO6) et de groupes Si2O7: Les phases A3Ta6Si4O26 (A= Ba, Sr) et K6M6Si4O26 (M= Nb, Ta). *Mater. Res. Bull*. **1976**, 11, 887–894.

39. H. H. Tippins. Optical Absorption and Photoconductivity in the Band Edge of β-Ga2O3. *Phys. Rev*. **1965**, 140, A316–A319.

40. M. Stapelbroek, B. D. Evans. Exciton structure in the uv-absorption edge of tetragonal GeO2. *Solid State Commun*. **1978**, 25, 959–962.

41. T. Takayama, A. Iwase, A. Kudo. Photocatalytic Water Splitting over Rod-shaped K3Ta3Si2O13 and Block-shaped Ba3Ta6Si4O26 Prepared by Flux Method. *Chem. Lett*. **2015**, 44, 306–308.

42. B.-H. Lei, S. Pan, Z. Yang, C. Cao, D. J. Singh. Second harmonic generation susceptibilities from symmetry adapted Wannier functions. *Phys. Rev. Lett*. **2020**, 125, 187402.

Chapter 4. Structrue and Optical Properties of Germanium Oxysulfide $La_4(GeS_2O_2)_3$

4.1 Introduction

Mixed-anion compounds have provided a platform for solid-state scientists to explore unique physical and chemical performances. Differences in the electronic properties of anoins, such as ionic radius, elecronegativity, oxidation state, and polarizability, results in the formation of new crystal structures with heteroleptic functional building block units.[1-3] Mixed-anion compounds such as oxychalcogenides, usually exhibit long-term anionic ordering, leading to anionic separation in 2-dimensional (2D) layer structures.[4-7] Based on the hard-soft acid-base (HSAB) theory,[8] highly electronetative/polarizable cations tend to bond with highly electronetative/polarizable anions. Therefore, these anionic separation layers can be stabilized in one structure. However, when the difference in electronegativity or polarizability are small, or the concentration of a given anion is higher than another, the higher order dimensional anionic distribution will be observed in mixed-anion compounds.

Oxychalcogenides have been widely investigated for their interesting optical performances. The finely tuning of the optical band gap can be achieved by the combination of chalcogenide species (S, Se, Te) and oxides, which valence band maximum is rised due to the higher energy level of chalcogenides than oxides.[9,10] Following the mixed-anion directed strategy, many layerd oxysulfides with layered structures were successfully synthesized, and exhibited photocatalytic activity under solar irradiation.[11-13] For another important optical application NLO, oxychalcogenides with the high polarizable asentric functional building block units are promising candidates exhibiting outstanding SHG intensities.[14,15] $SrZn_2S_2O$ crystallizes in the NCS space group $Pmn2_1$ and exhibits phase-matchable SHG property of twice SHG coefficient to that of KDP. In addition, it can evolve H_2 and O_2 via a water-splitting

reaction under ultraviolet irradiation and show better photocorrosion resistance than that of single anionic Zn compounds ZnO and ZnS.[16] It seems that this anionic directed design will play a significant role in performing unique optical characterisitcs with the rearrangement of the various functional building block units.

In this chapter, we report a novel germanium-based oxysulfide $La_4(GeS_2O_2)_3$ via flux growth method, which have been considered as a widely utilized technology for developing new mixed-anion compounds.[17-24] Single crystals of $La_4(GeS_2O_2)_3$ were obtained from the reaction of starting materials and $BaCl_2$-$CaCl_2$ eutectic mixture. The crystal structure, characterized by unusual GeS_2O_2 tetrahedra, 3D anion ordering, electronic structure, and optical properties, are discussed.

4.2. Experimental details of Chapter 4

Reagents. La_2S_3 (Alfa Aesar, 99%), GeO_2 (Rare Metallic, 99.99%), $BaCl_2$ (Rare Metallic, 99.9%), and $CaCl_2$ (Rare Metallic, 99.99%) were used as received. Before use, two chlorides were heated overnight in a dry oven at 260°C. All the raw materials were stored in an argon-filled glove box.

Crystal Growth. $La_4(GeS_2O_2)_3$ single crystals were grown out of a $BaCl_2$-$CaCl_2$ eutectic flux. La_2S_3 (0.5mmol), GeO_2 (1.0 mmol), $BaCl_2$ (3.13 mmol) and $CaCl_2$ (3.13 mmol) were placed into an alumina crucible in an Ar-filled glove box. The crucible was fused in a vacuum of 10^{-4} Pa and sealed by flame in a quartz tube. The raw material was heated to 850℃ at 5℃ /min in muffle furnace for 24 h and cooled to 550℃ at 0.08℃/min. Finally, the heater was turned off and cooled naturally to room temperature. The product was washed in sonicated water and extracted from flux. Ivory-white $La_4(GeS_2O_2)_3$ block crystal was prepared by vacuum filtration.

Single-Crystal Structure Determination. X-ray intensity data of ivory block crystals at 301(2)K were collected using a Brock D8 QUEST diffractograph equipped with PHOTON-

100 CMOS area detector and Incoatec microfocusing (Mo Kα radiation, λ = 0.71073 Å). The data were collected in 100% reciprocal space, $2\theta_{max}$ = 72.6°, the average reflection redundancy was 14.7, and the Rint after absorption correction was 0.057. The original area detector data frames were reduced and corrected to eliminate absorption effects using SAINT+ and SADABS programs.[25,26] The final cell unit parameters were determined by least square refinement of 9908 reflections extracted from the dataset. An initial structural model was obtained using SHELXT.[27] Subsequent difference Fourier calculations and full matrix least-squares refinement against F2 were performed with SHELXL- 2018 using the ShelXle interface.[28]

Synchrotron X-ray Powder Diffraction. The single crystals of $La_4(GeS_2O_2)_3$ were pulverized with agate mortar and pestle to obtain fine powder. Synchronous X-ray powder diffraction (SXRD) spectra and UV-vis diffuse reflectance spectra were collected. SXRD measurements were made at room temperature using a one-dimensional detector mounted on the NIMS BL15XU beam at Spring-8, Japan. Synchrotron radiation X-rays were monochrome with a wavelength of 0.65298 Å. The powder $La_4(GeS_2O_2)_3$ sample was packed into a glass capillary with an inner diameter of 0.2 mm. Diffraction data were collected in 0.003° increments in the range of 2-60 ° and analyzed using the Rietveld refined Rietan-FP program.[29]

TGA, UV−Vis Diffuse Reflectance Spectra, and SEM-EDS. Thermogravimetric analysis (TGA) was performed using a PerkinElmer Pyris 1 TAG system at an O_2 gas flow with rate of 60 mL/min. The sample was placed in an alumina crucible and heated to 1000°C at 10°C/min. Rigaku MiniFlex X-ray diffractometer (Cu Kα radiation) was used for XRD analysis of thermal treatment samples. Diffuse reflectance spectrometric measurements were made at room temperature using a Shimazu UV-2600 spectrophotometer and an ISR-2600Plus integrating sphere. The diffuse reflection data were converted to absorbance within the instrument by the Kubelka−Munk function. Scanning electron microscopy (TESCAN Vega-E

SBU) was used to analyze the single crystal $La_4(GeS_2O_2)_3$. All crystals are mounted on a carbon tape and analysis was performed using an acceleration voltage of 20 kV.

Electronic Structure Calculations. First-principles total energy calculations for $La_4(GeS_2O_2)_3$ were performed using the projector augmented wave (PAW) method,[30,31] which was identical to the method in the Vienna ab-initio simulation package (VASP).[32-34] The configurations of valence electrons in PAW potential are as following: La-5s^2, 5p^6, 6s^2, 5d^1, Ge-3d^{10}, 4s^2, 4p^2, O-2s^2, 2p^2, and S-3s^2, 3p^4. The HSEsol-type hybrid functional was adopted.[35] In this work, the experimental hexagonal $La_4(GeS_2O_2)_3$ unit cell was used as the initial structural model for the calculation of first-principles total energy. The cutoff energy for the plane wave basis set and the mesh size for kpoint sampling in the Brillouin zone were set to be 550 eV and 1 × 1 × 3, respectively. Lattice constants and internal atomic positions were fully optimized until all residual forces became < 0.02 eV/Å.

4.3. Results and discussion

4.3.1. Crystal Structure

Ivory-white block single crystals of $La_4(GeS_2O_2)_3$ were shown in Figure 4.1. Single crystal structure analysis revealed that $La_4(GeS_2O_2)_3$ crystallizes in *R*-3 (No. 148) space group with lattice constants a = 16.8283(3) Å and c = 8.4140(2) Å. No atomic deviation from full occupancy was detected. Thus, in the final stage of structural improvement, their residential status was fixed. Table 4.1 lists the details of the structure refinements. Table 4.2 summarizes crystal parameters, including atomic coordinates and atomic displacement parameters. The anisotropic displacement parameters are shown in Table 4.3.

Figure 4.1. Photograph of single crystals of $La_4(GeS_2O_2)_3$ on a 1 mm grid-cell plate.

Table 4.1. Results of the Structure Refinement of $La_4(GeS_2O_2)_3$ Using Single-Crystal X-ray Diffraction

Formula	$La_4(GeS_2O_2)_3$
Formula weight	1061.77
Radiation	Mo Kα (λ = 0.71073 Å)
***T* (K)**	301(2)
Crystal system	trigonal
Space group	*R*-3
***a* (Å)**	16.8283(3)
***b* (Å)**	16.8283(3)
***c* (Å)**	8.4140(2)
***V* (Å^3)**	2063.54(9)

Z	6
D_{calc} (g/cm^3)	5.126
F_{000}	2808
no. of measured reflns	32798
no. of unique reflns	2225
no. of observed reflns ($F^2 > 2\sigma(F^2)$)	1868
R_{int} (%)	5.70
$R[F^2 > 2\sigma(F^2)]/wR(F^2)$ (%)	2.22/3.45
GoF	1.062

Table 4.2. Crystallographic and Refinement Data Obtained from Single-Crystal Structure Analysis of $La_4(GeS_2O_2)_3$

Atom	site	x	y	z	occupancy	U_{iso}/ Å^2
La1	18*f*	0.18672(2)	0.24104(2)	0.15890(2)	1	0.00902(3)
La2	3*b*	0	0	1/2	1	0.01243(7)
La3	3*a*	0	0	0	1	0.00792(6)
Ge	18*f*	0.18713(2)	0.04347(2)	0.24397(3)	1	0.00720(5)
S1	18*f*	0.26044(4)	−0.02833(4)	0.19177(7)	1	0.01228(11)
S2	18*f*	0.22741(4)	0.14889(4)	0.42442(7)	1	0.01035(11)
O1	18*f*	0.06959(11)	−0.04136(11)	0.25780(19)	1	0.0082(3)
O2	18*f*	0.18462(11)	0.10106(11)	0.06669(18)	1	0.0099(3)

Table 4.3. Anisotropic Displacement Parameters U_{ij} (Å^2) for $La_4(GeS_2O_2)_3$ at 301 K

Atom	U_{11}	U_{22}	U_{33}	U_{23}	U_{13}	U_{12}
La1	0.00858(6)	0.00651(6)	0.01144(6)	−0.00042(4)	−0.00159(5)	0.00338(5)
La2	0.01475(10)	0.01475(10)	0.00781(14)	0	0	0.00737(5)
La3	0.00733(9)	0.00733(9)	0.00910(13)	0	0	0.00366(4)

Ge	0.00696(11)	0.00689(11)	0.00789(10)	−0.00046(8)	−0.00042(8)	0.00356(9)
S1	0.0096(3)	0.0139(3)	0.0158(3)	−0.0047(2)	−0.0019(2)	0.0077(2)
S2	0.0099(3)	0.0099(3)	0.0106(2)	−0.00343(19)	−0.00225(19)	0.0046(2)
O1	0.0068(7)	0.0071(7)	0.0096(7)	−0.0008(6)	0.0010(6)	0.0025(6)
O2	0.0136(8)	0.0109(8)	0.0070(7)	0.0010(6)	0.0002(6)	0.0074(7)

Figure 4.2 shows the SXRD patterns of the powder samples of hand-picked $La_4(GeS_2O_2)_3$ single crystal obtained by fine grinding. Rietveld refinement was carried out using the structure model determined by single crystal structure analysis. The calculated model can reproduce the observed model well, and the refinement is easy to convergence, and the reliability index is good, $R_{wp} = 4.90\%$, $R_B = 6.88\%$, $R_F = 3.78\%$. Supporting information Table 4.4 summarizes the final refined crystallographic data.

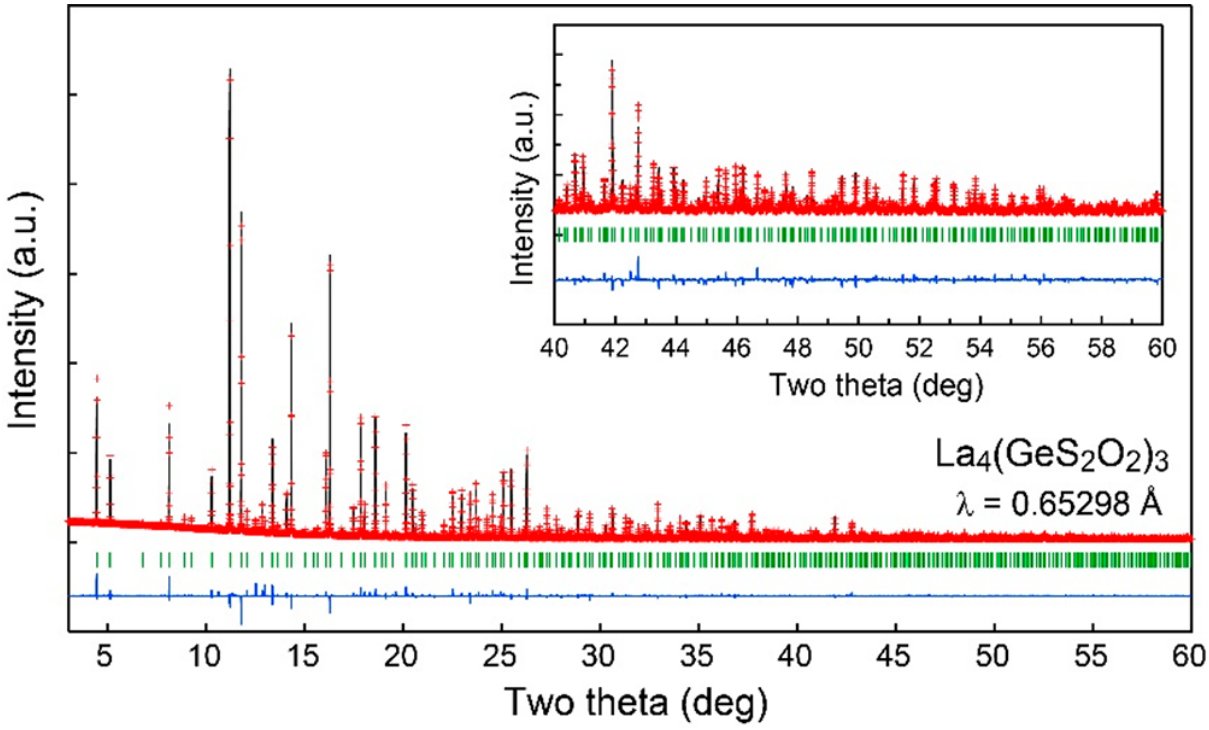

Figure 4.2. Synchrotron X-ray powder diffraction patterns of $La_4(GeS_2O_2)_3$ measured at room temperature. Obtained, calculated, and difference data are presented by cross marks (red), upper solid lines (black), and bottom solid lines (blue), respectively. The vertical lines (green)

represented the expected Bragg peak positions of $La_4(GeS_2O_2)_3$.

Table 4.4. Atomic Coordinates and Isotropic Displacement Parameters Refined against the SXRD Data Collected from $La_4(GeS_2O_2)_3$ at room temperature.

atom	site	*x*	*y*	*z*	occupancy	B_{equ}/ Å^2
La1	18*f*	0.18640(7)	0.24115(7)	0.15842(12)	1	0.780(15)
La2	3*b*	0	0	1/2	1	1.11(6)
La3	3*a*	0	0	0	1	0.43(4)
Ge	18*f*	0.18670(9)	0.04372(13)	0.24143(17)	1	0.45(3)
S1	18*f*	0.2602(3)	-0.0272(2)	0.1898(4)	1	1.26(8)
S2	18*f*	0.2273(2)	0.1531(2)	0.4181(4)	1	1.54(9)
O1	18*f*	0.0679(5)	-0.0441(6)	0.2503(9)	1	0.18(14)
O2	18*f*	0.1753(5)	0.0996(7)	0.0684(9)	1	0.18

The space group is *R*-3 (No. 148) with $a = b = 16.82677(1)$ Å, $c = 8.41591(1)$ Å. *R* indices are $Rwp = 4.90\%$, $R_B = 6.88\%$, and $R_F = 3.78\%$.

As shown in Figure 4.3, $La_4(GeS_2O_2)_3$ crystallizes in a three-dimensional crystal structure composed of unique La- and Ge-centered polyhedra. The non-equivalent La1, La2 and La3 atoms occupy Wyckoff positions of 18*f*, 3*f* and 3*a*, respectively. In contrast, only one germanium atom iss located at the 18*f* site. The two anions O^{2-} and S^{2-} are completely ordered in structure. Figure 4.4 shows the local coordination environment around the La and Ge atoms. In these three lanthanum sites, La1 and La2 are surrounded by two different anions. La1 is coordinated by three oxygen atoms ($d_{La-O1, La-O2} \sim 2.45$ Å on average) and six sulfur atoms ($d_{La-S1} \sim 3.28$ Å, $d_{La-S2} \sim 2.99$ Å on average) to form a twisted gyroelongated square pyramid. Although these bond distances vary from -7 to 12%,[36] from the reference value of the Shannon's ion radius, the bond valence sum (BVS)[37] calculated for La1 yields 2.91, which is consistent with the nominal oxidation state of the lanthanum ion. La2 is coordinated icosahedral by six oxygen atoms ($d_{La-O1} = 2.6123(19)$ Å) and six sulfur atoms ($d_{La-S2} =$

3.4262(6) Å). The bond lengths of La−O1 and La−S2 are 5% shorter and 7% longer than the sum of the ionic radii of La^{3+} and O^{2-}/S^{2-}, respectively. Compared with the two lanthanum atoms, La3 is a 12-fold coordinated that only connected with oxygen atoms, forming a relatively symmetric icosahedron (d_{La-O1} = 2.7159(19) Å; d_{La-O2} = 2.7524(16) Å). The bonds between lanthanum and oxygen atoms agree well, because their ionic radii add up to less than 1%. The BVS of La2 and La3 were 2.54 and 2.63, respectively, which were much lower than the expected values. In general, BVS values below ideal values are usually interpreted as underbonding (or tensile stress) between the metal center and the surrounding ligands. However, it is not clear why te BVS values of La2 and La3 are low. The germanium atom is tetrahedral coordinated by two oxygen atoms (d_{Ge-O1} = 1.7721(15) Å and d_{Ge-O2} = 1.7908(18) Å) and two sulfur atoms (d_{Ge-S1} = 2.1600(10) Å and d_{Ge-S2} = 2.1707(7) Å). These bond distances are consistent with those calculated from the sum of the radii of the Ge^{4+} and La^{3+} ions and the radii of the O^{2-} and S^{2-} ions. A reasonable value of 4.15 is obtained from the BVS calculation for Ge. The S−Ge−S bond Angle is 124.56(3) °, much higher than the O−Ge−O bond Angle of 99.89(8) °. This can be reasonably explained by considering the electrostatic repulsion between sulfide ions with larger ionic radii.

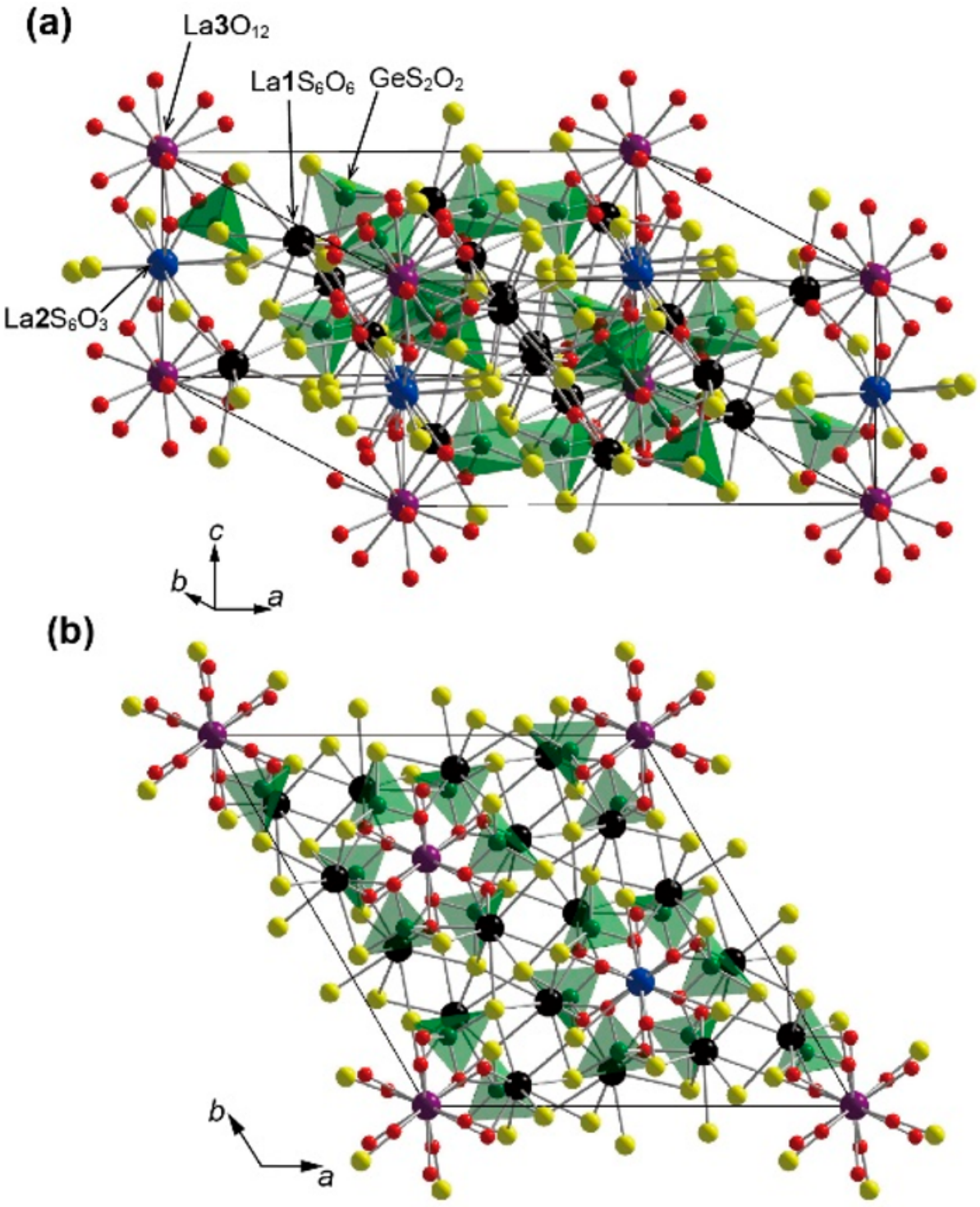

Figure 4.3. Crystal structure of $La_4(GeS_2O_2)_3$. Black, blue, purple, green, red, and yellow spheres stand for La1, La2, La3, Ge, O, and S atoms, respectively.

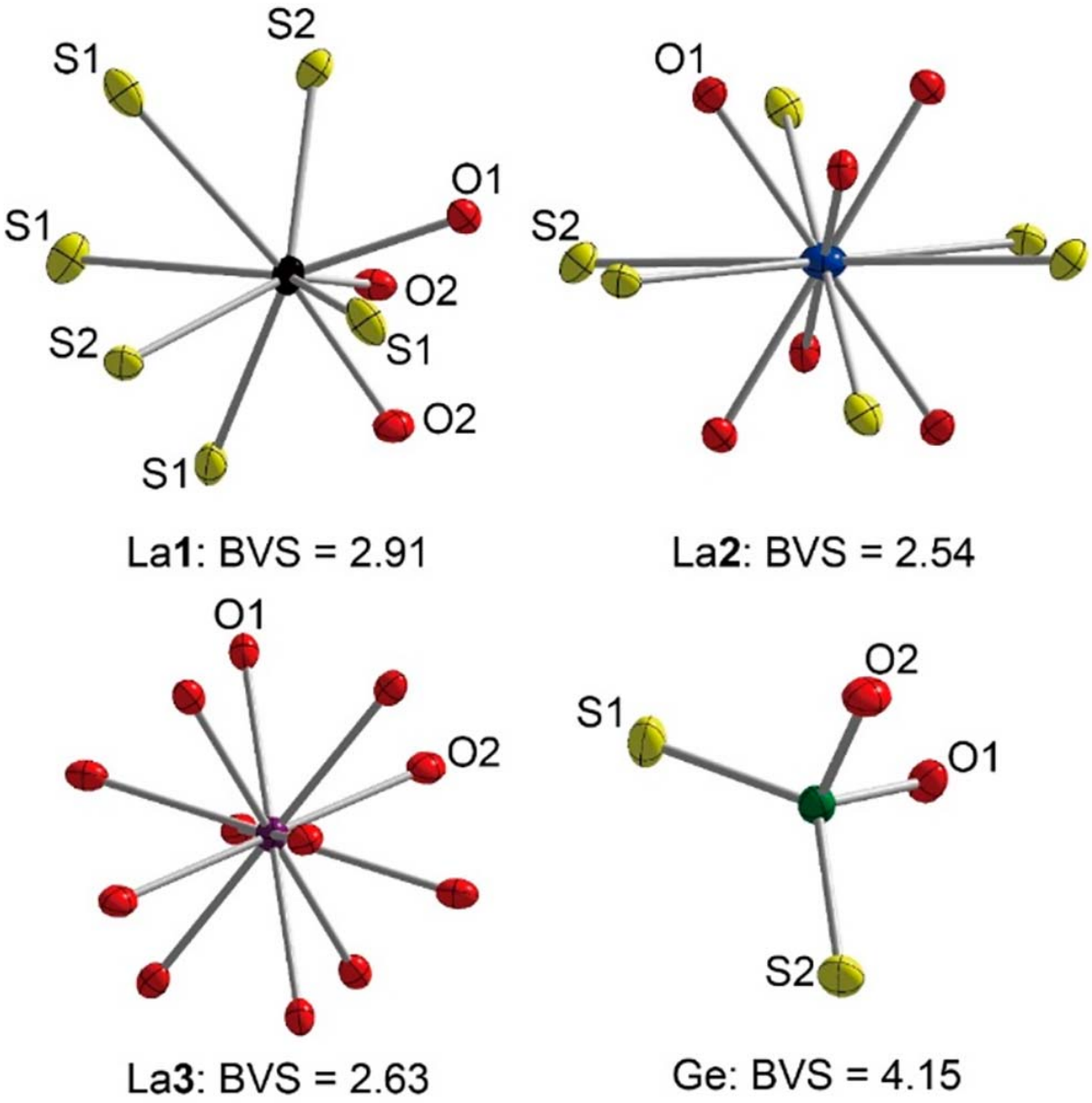

Figure 4.4. Local coordination environment around La1, La2, La3, and Ge atoms. Displacement ellipsoids are shown at the 90% level.

Germanium ions coordinated by two sulfides and two oxide ions are rare compared to the GeS_3O tetrahedron, which is normally stable in oxide sulfides with melilite structure.[38,39] As far as we know, only two other germanium-based compounds with similar coordination geometry centered on germanium were synthesized: $Na_2GeS_2(OH)_2 \cdot 5H_2O$[40] and $AGeS_2O$ (A = Sr, Ba)[21]. The Ge-S and Ge-O distances and the S-Ge-S and O-Ge-O bond angles of these

compounds are similar to $La_4(GeS_2O_2)_3$ (Table 4.5), but the GeS_2O_2 tetrahedron of $Na_2GeS_2(OH)_2 \cdot 5H_2O$ is slightly elongated with smaller S-Ge-S and O-Ge-O bond angles.

Table 4.5. Selected Interatomic Distances (Å) and Bond Angles (°) of $La_4(GeS_2O_2)_3$

bond distance (Å)		bond angle (°)	
La1-O1	2.4229(16)	O2-La1-O2	73.36(6)
La1-O1	2.4634(16)	O2-La1-O1	73.67(5)
La1-O1	2.4726(15)	O2-La1-O1	74.01(5)
La1-S2	2.9877(6)	O1-La2-O1×6	65.62(6)
La1-S2	2.9904(6)	O1-La2-O1×6	114.38(6)
La1-S1	3.1571(6)	O1-La2-O1×2	180.000
La1-S1	3.2075(6)	O1-La2-S2×4	61.99(4)
La1-S1	3.3467(6)	O1-La2-S2×6	118.01(4)
La1-S1	3.4279(6)	O1-La2-S2×6	115.82(4)
La2-O1×6	2.6123(15)	O1-La2-S2×6	64.18(4)
La2-S2×6	3.4262(6)	O1-La2-S2×6	62.06(4)
La3-O1×6	2.7159(16)	O1-La2-S2×6	117.94(4)
La3-O2×6	2.7524(16)	S2-La2-S2×5	63.363(6)
Ge1-O1	1.7720(16)	S2-La2-S2×5	116.637(6)
Ge1-O2	1.7908(16)	S2-La2-S2×3	180.000
Ge1-S1	2.1600(6)	O1-La3-O1×6	117.18(5)
Ge1-S2	2.1701(6)	O1-La3-O1×6	62.82(5)
		O1-La3-O1×3	180.00(8)
		O1-La3-O2×6	120.17(5)
		O1-La3-O2×6	65.81(5)
		O1-La3-O2×6	114.19(5)
		O1-La3-O2×6	59.83(5)
		O2-La3-O2×6	115.95(2)
		O2-La3-O2×6	64.05(2)
		O1-Ge1-O2	99.89(7)
		O1-Ge1-S1	106.40(5)
		O2-Ge1-S1	107.94(5)

	O1-Ge1-S2	112.29(5)
	O2-Ge1-S2	102.86(5)
	S1-Ge1-S2	124.56(2)

Figure 4.5a shows the connection between La- and Ge-centered polyhedra. $La_2S_6O_6$ and La_3O_{12} polyhedra have a common O3 plane and form a one-dimensional chain along the *c* direction. Each La-based one-dimensional chain is surrounded in a complex manner by $La1S_6O_3$ and GeS_2O_2 polyhedra. The $La_2S_6O_6$ icosahedron is connected to six $La1S_6O_3$ polyhedra and six GeS_2O_2 tetrahedra by edge-shared pairs of oxygen and sulfur atoms. These La1-based polyhedra are separated by Ge and La2 atoms. In contrast, the La_3O_{12} icosahedron shares an O3 plane with six $La1S_6O_3$ polyhedra and O2 edges with six GeS_2O_2 tetrahedra, all of which have two distinct independent z coordinates. In addition, the six $La1S_6O_3$ polyhedra are connected to each other by a shared edge formed by a pair of oxygen and sulfur atoms. All GeS_2O_2 tetrahedra share edges with $La1S_6O_3$, $La2S_6O_6$, and $La3O_{12}$ polyhedra.

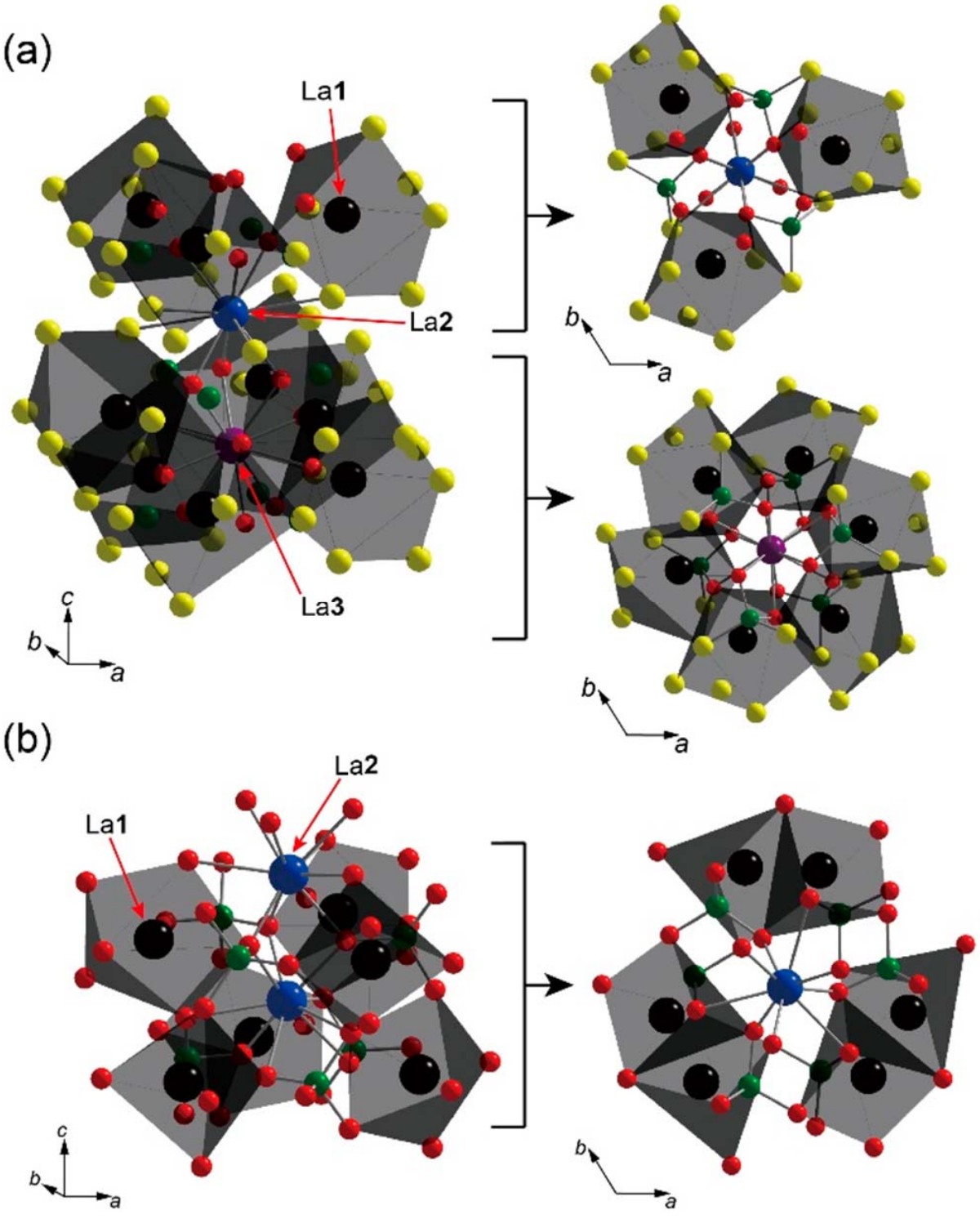

Figure 4.5. Linkage between La- and Ge-centered polyhedra in (a) $La_4(GeS_2O_2)_3$ and (b) $La_{9.33}(GeO_4)_6O_2$ viewed along two different directions. In the former, La2- and La3-centered polyhedra are surrounded by six La1-centered polyhedra and six Ge-centered tetrahedra in a different arrangement. In the latter, La2-centered polyhedra are surrounded by six La1-centered

polyhedra and six Ge-centered tetrahedra in a different arrangement.

It is interesting to compare the present oxygen sulfide with germanium oxide apatite $La_{9.33}(GeO_4)_6O_2$ formed in the hexagonal space group $P63/m$.[41,42] Despite the long anion ordered structure and completely different chemical composition of $La_4(GeS_2O_2)_3$, the oxysulfide phase of the compound exhibits a polyhedral arrangement with Ge- and La- center similar to the structure of oxygen apatite. As shown in Figure 4.5b, the $La2O_9$ polyhedra in the structure $La_{9.33}(GeO_4)_6O_2$, like in the structure $La_4(GeS_2O_2)_3$, form an infinite 1D chain along the *c* direction by sharing the O_3 plane. These one-dimensional chains are surrounded by six GeO_4 tetrahedra and six $La1O_7$ polyhedra with different z coordinates, which are connected to $La2O_9$ by shared oxygen edges and vertices, respectively. In $La_4(GeS_2O_2)_3$ and $La_{9.33}(GeO_4)_6O_2$, the La2/La3 atom lies at the geometric center of an equilateral triangle formed by Ge or La1 atoms. However, Ge- or La1-based triangles form a regular hexagon in oxysulfide, as shown in Figure 4.6 for a top-down view of these crystal structures. This contrasts with the twisted hexagons in the structure of oxyapatite.

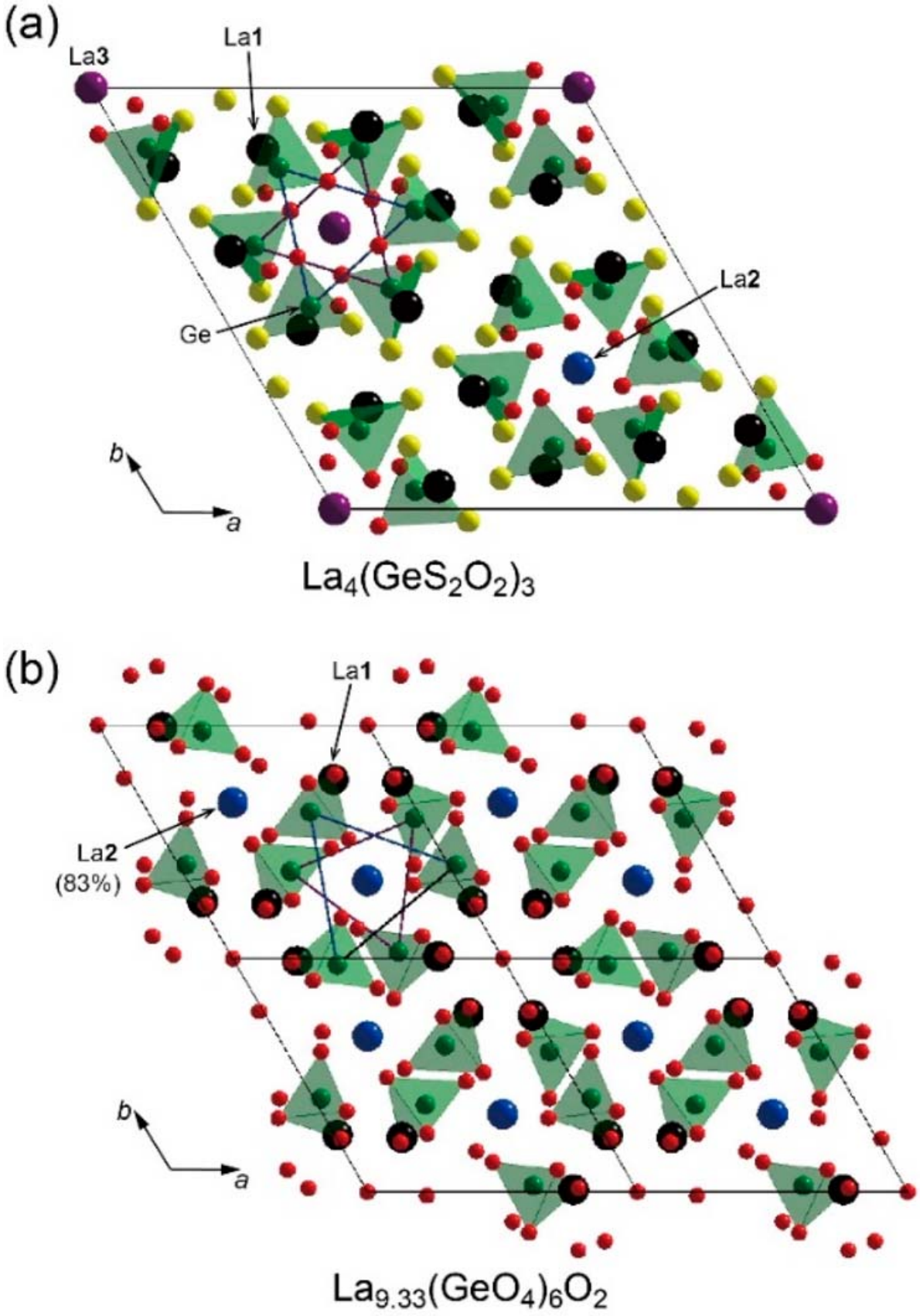

Figure 4.6. Crystal structure of $La_4(GeS_2O_2)_3$ (a) and $La_{9.33}(GeO_4)_6O_2$ (b) viewed along the c

axis.

4.3.2 Thermal Stability

Figure 4.7 shows the thermogravimetric data collected under flowing oxygen. $La_4(GeS_2O_2)_3$ was stable at 800°C, but on further heating to 1000°C the weight droped rapidly by about 3%, indicating decomposition of the oxysulfide phase. Weight cooled to ambient temperature was −2.9%. As shown in Figure 4.8, the powder XRD test of the thermal treatment sample revealed that the main phase was germanium oxyapatite. However, the secondary phase exhibited a relatively low intensity that cannot be identified.

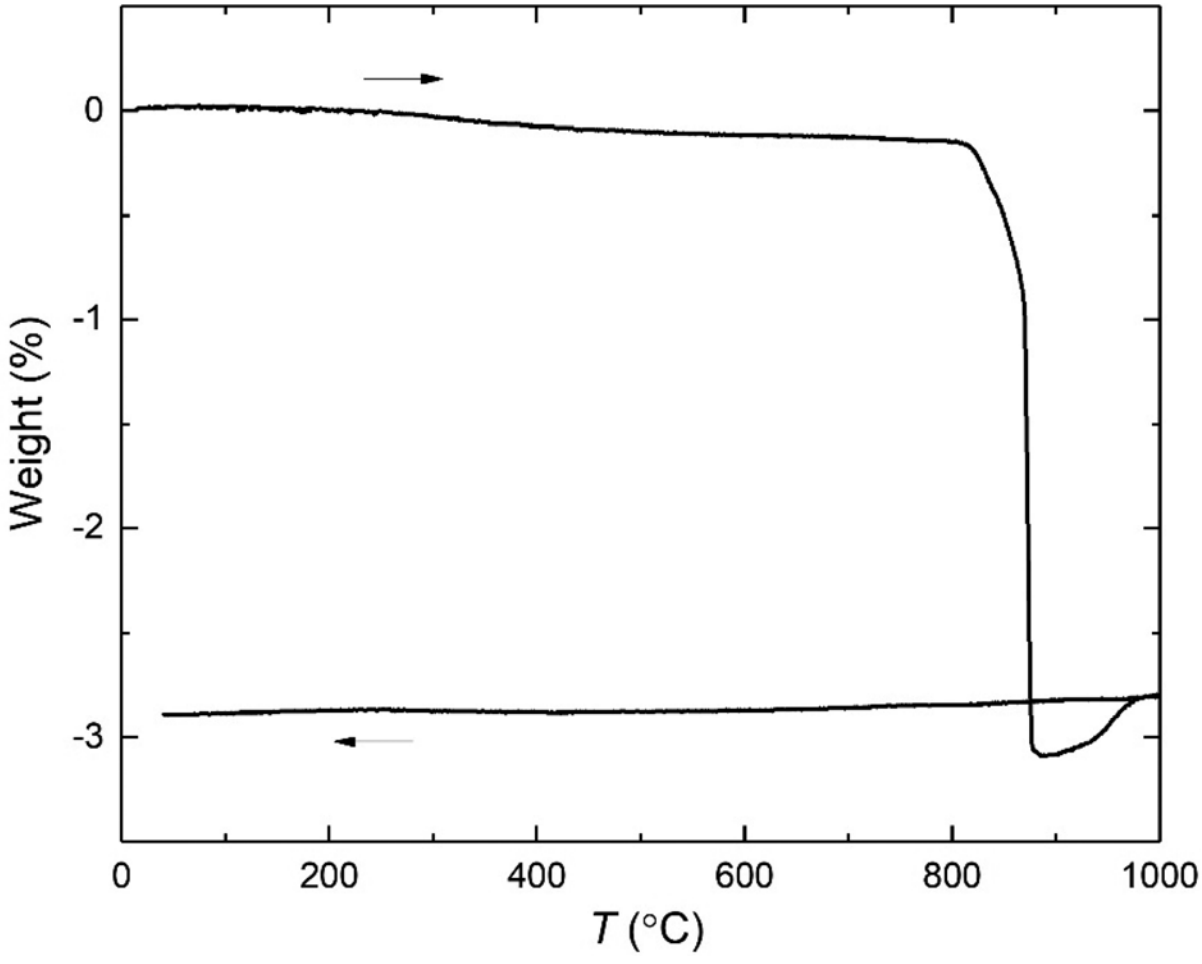

Figure 4.7. Thermogravimetric curve of $La_4(GeS_2O_2)_3$, in O_2 gas atmosphere.

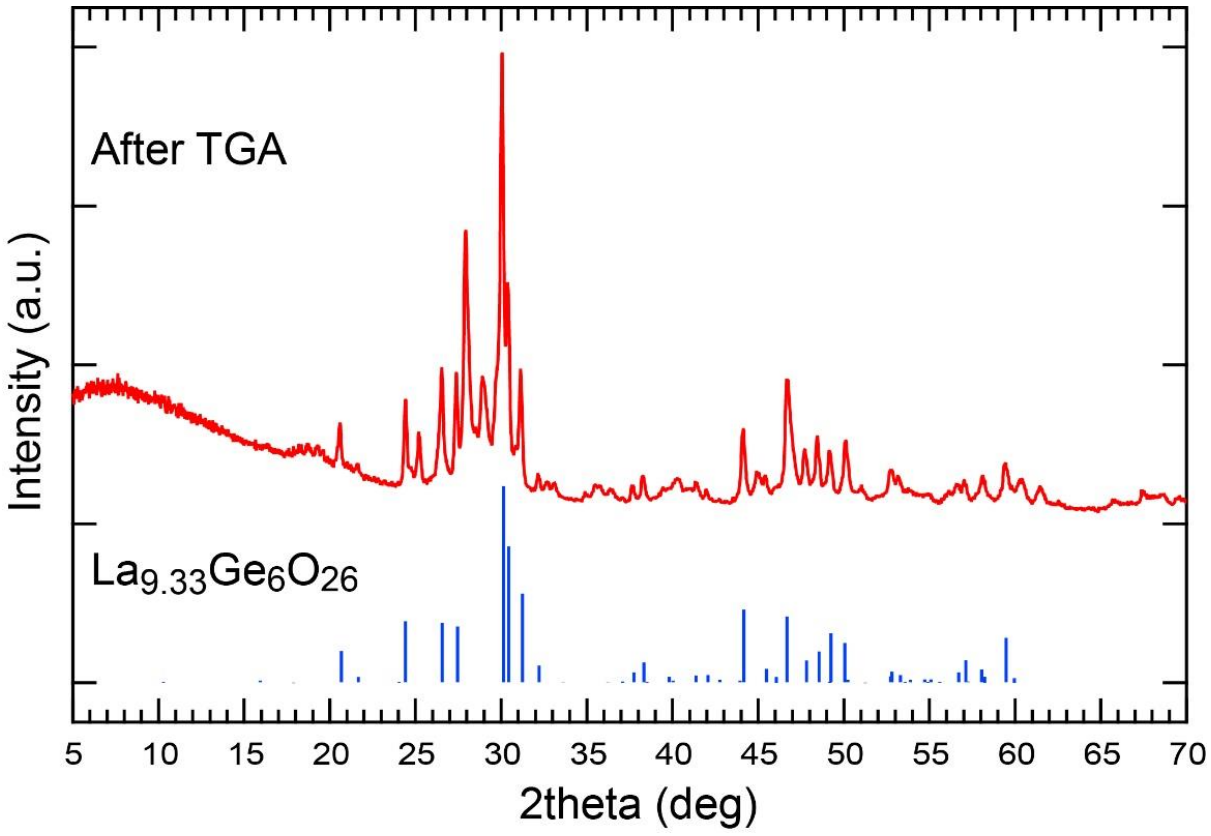

Figure 4.8. Room-temperature powder XRD pattern of the product after TG measurement. Major peaks could be assigned to a germanium oxyapatite, $La_{9.33}Ge_6O_{26}$, but many peaks with relatively low intensities, which are probably assigned to secondary phases, could not be identified.

4.3.3. Optical Property

Figure 4.9 shows the UV-vis absorption spectra of powder $La_4(GeS_2O_2)_3$. The absorption data were obtained by converting the reflection spectrum of the sample through Kubelka-Munk transformation.[43] The absorption curves showed two sharp increases near 2.5eV and 3.5eV, and the absorption edge energies obtained by extrapolating the linear part of the absorption curve to the X-axis were E_g1 = 2.23eV and E_g2 = 3.67eV, respectively. Given that the sample is ivory-white, absorption at E_g1 is likely due to defects caused by negative ion holes, although negative and cation holes cannot be detected by XRD analysis. The larger absorption edge at E_g2 corresponds to the intrinsic optical band gap, which is discussed below.

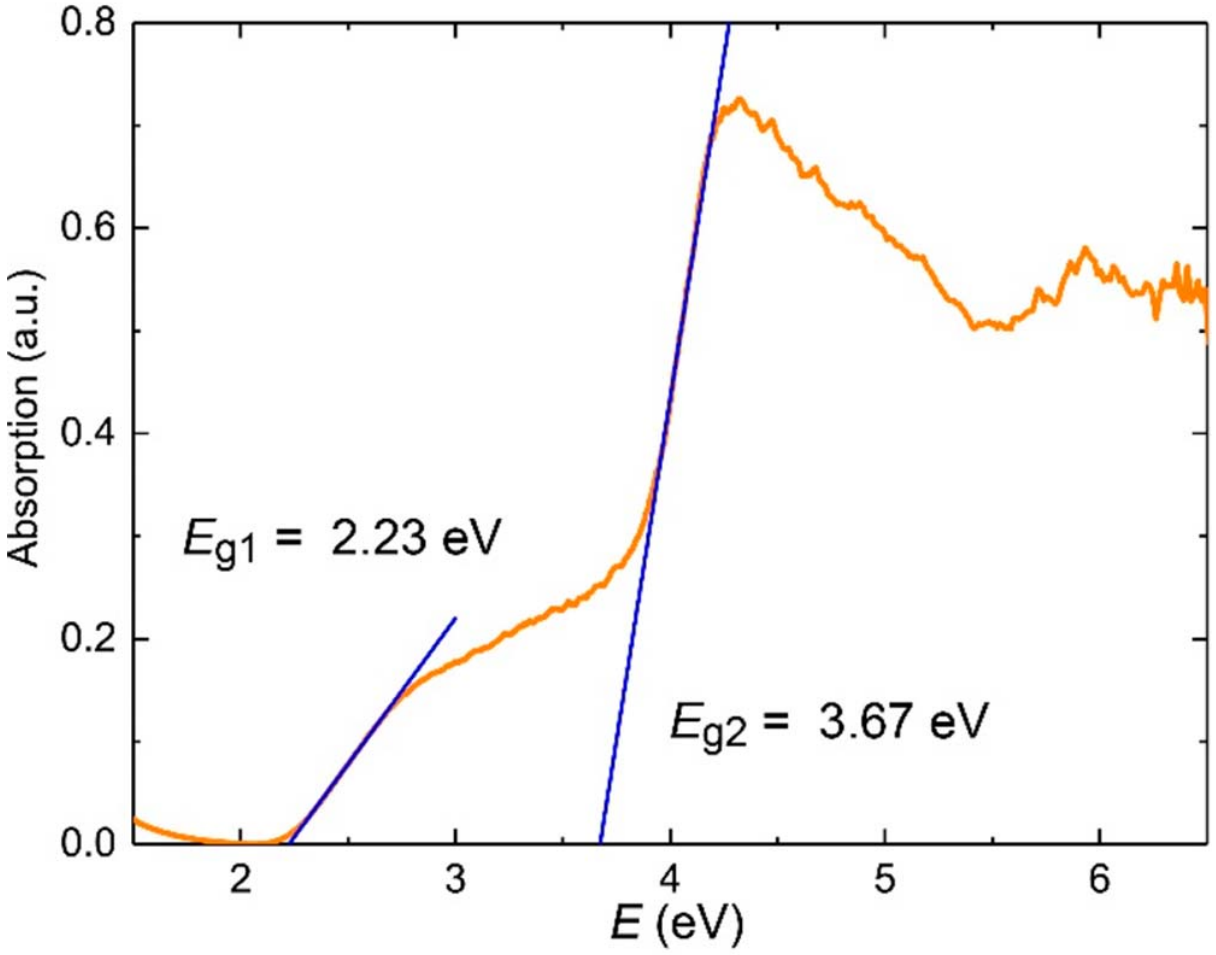

Figure 4.9. UV−vis optical absorption spectrum of $La_4(GeS_2O_2)_3$, which was converted from the diffuse reflectance data using the Kubelka−Munk function.

4.3.3. Theoretical Calculation.

In order to better understand the relationship between the electronic structure and optical properties of $La_4(GeS_2O_2)_3$, first-principles calculations were performed. The optimized lattice constants are a = 16.724 A and c = 8.291 A. The internal atomic coordinates of the optimized $La_4(GeS_2O_2)_3$ unit are listed in Table 4.6. Compared with the experimental values, the a and c axis of the lattice constants of $La_4(GeS_2O_2)_3$ are underestimated by 0.6% and 1.4%, respectively. The internal atomic positions of the relaxation units agree well with the refined crystal data shown in Table 4.2. The results show that the structure optimization calculation in this paper has sufficient precision. Figure 4.10 and 4.11 show total and partial state densities

(DOS) and electron band dispersion curves of sulfide. The electronic structure was calculated by using the original cell model of the optimized hexagonal cell transformation. The total DOS showed an energy gap of E_g = 4.01 eV, similar to E_g2 but significantly larger than E_g1. This result strongly suggests that the absorption edge observed at E_g2 is intrinsic to the electronic structure of the oxysulfide phase. The valence bands mainly come from O-2*p* and S-3*p* orbitals, which are weakly hybridized with La-3*p*, 3*d* and 4*f* orbitals. In the upper energy region of the maximum valence band (VBM), the S-3*p* band dominates, while in the lower energy region, the O-2*p* band dominates, which is often observed in oxysulfides. The minimum conduction band (CBM) is mainly composed of La-3*d* and 4*f* orbitals, Ge-4*s* and S-3*p* orbitals. As can be seen from the electron band dispersion curve shown in Figure 4.11, VBM is located at the Γ point and CBM is located between T and P. The light absorption above E_g2 in UV-Vis spectrum is the result of the transition from VBM to CBM. The Ge-4*s* and 4*s* orbitals are located in the narrow energy region between −8 to −7 eV and −6 to −4 eV, respectively, and are highly hybridized with the O-2*p* and S-3*p* orbitals. The locality of these Ge bands contrasts sharply with the wide dispersion of the La band in the valence band, which is caused by isolated connections between the GeS_2O_2 tetrahedra.

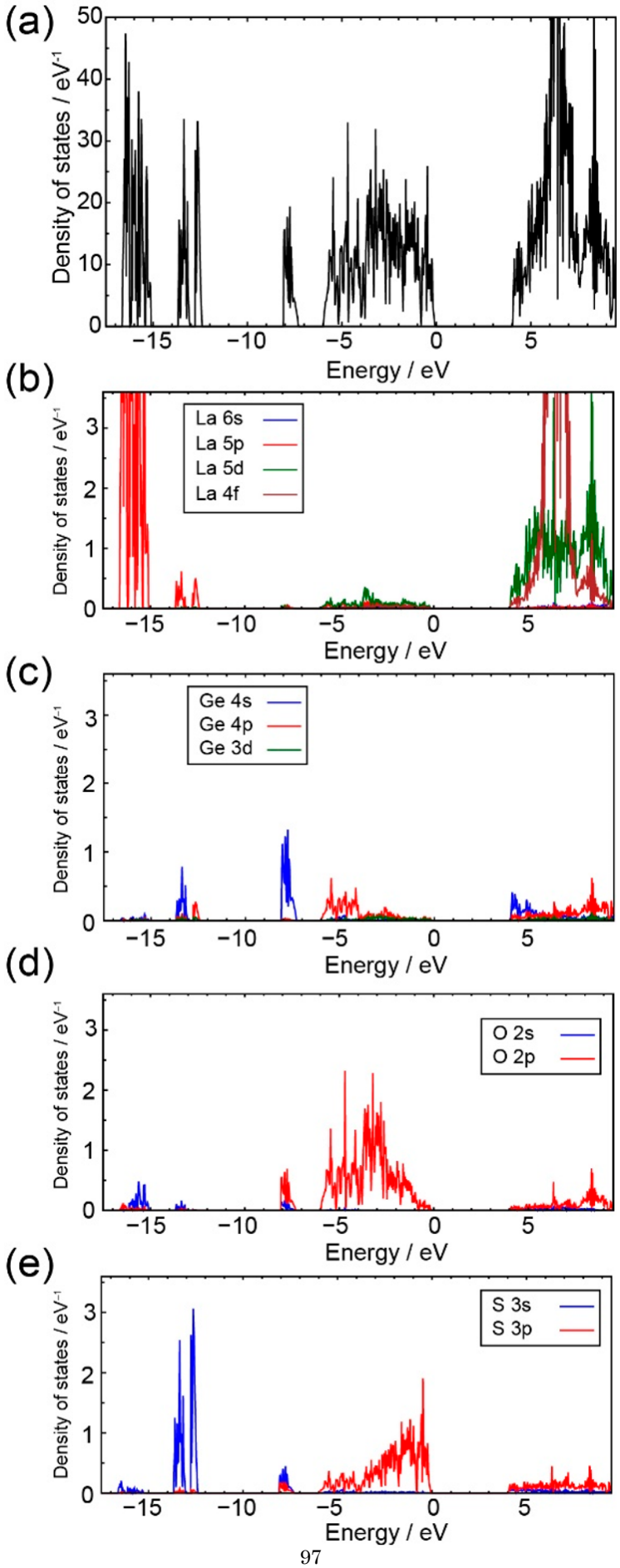
(a)
Density of states / eV-1
Energy / eV
(b)
La 6s
La 5p
La 5d
La 4f
(c)
Ge 4s
Ge 4p
Ge 3d
(d)
O 2s
O 2p
(e)
S 3s
S 3p

Figure 4.10. (a) Total and (b−e) partial density of states of $La_4(GeS_2O_2)_3$ obtained by first-principles calculations based on the HSEsol hybrid functional. In the horizontal axis, the energy level of the valence band maximum is set to be 0 eV.

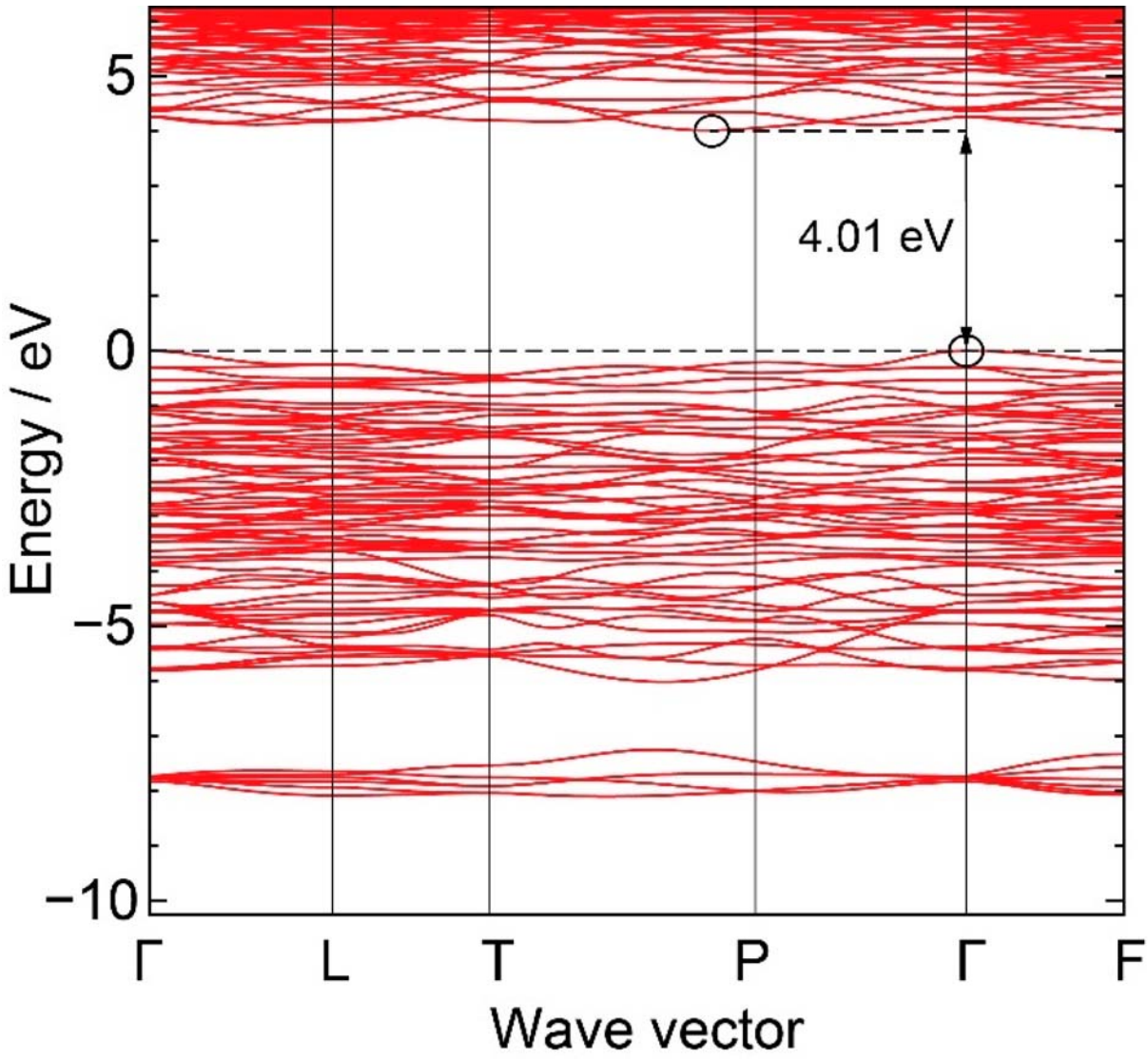

Figure 4.11. Electronic band dispersion curves of a primitive cell of $La_4(GeS_2O_2)_3$ obtained by first-principles calculations based on the HSEsol hybrid functional. In the vertical axis, the highest occupied band energy level is set to be 0 eV.

Table 4.6. Internal atomic coordinates of $La_4(GeS_2O_2)_3$ obtained by structure optimization based on the HSEsol hybrid functional calculations.

atom	site	*x*	*y*	*z*
La1	18*f*	0.186	0.240	0.159
La2	3*b*	0	0	1/2
La3	3*a*	0	0	0
Ge	18*f*	0.187	0.043	0.246
S1	18*f*	0.260	-0.029	0.190
S2	18*f*	0.228	0.149	0.427
O1	18*f*	0.068	-0.042	0.258
O2	18*f*	0.183	0.101	0.066

4.4. Summary of Chapter 4

A novel germanium oxysulfide $La_4(GeS_2O_2)_3$ with an indirect optical gap of 3.67 eV was synthesized from $BaCl_2$-$CaCl_2$ eutectic molten salt. Analysis of single crystal structure shows that the structure is formed by rare GeS_2O_2 tetrahedra and La-centered polyhedra connected by shared edges or conners. The connection between Ge- and La-centered polyhedra is similar observed in germanium oxapatite $La_{9.33}(GeO_4)_6O_2$, although the oxysulfide phase does not have the so-called "apatite channel" and oxidation ions at (0 0 z) are mobile at high temperatures. Recently, several new sulfide materials have shown their practical application as solid electrolytes for lithium-ion batteries. In the structure of these materials, highly polarized sulfur ions play an important role in improving the electrical conductivity of lithium ions. In $La_4(GeS_2O_2)_3$, each $La1S_6O_3$ polyhedron is connected to sulfide ions by shared edges, resulting in the formation of sulfide-rich regions outside alternating chains of LaO_{12} and LaS_6O_6 units on the shared planes. Future studies should attempt to determine whether this three-dimensional anion sequence in $La_4(GeS_2O_2)_3$ creates lithium ion paths by replacing La atoms with Li, as found in $La_{1-x}Li_yTiO_3$ perovskites.[44]

References in Chapter 4

1. Kageyama, H.; Hayashi, K.; Maeda, K.; Attfield, J. P.; Hiroi, Z.; Rondinelli, J. M.; Poeppelmeier, K. R. Expanding frontiers in materials chemistry and physics with multiple anions. *Nat. Commun*. **2018**, 9, 772.
2. Tsujimoto, Y.; Yamaura, K.; Takayama-Muromachi, E. Oxyfluoride Chemistry of Layered Perovskite Compounds. *Appl. Sci*. **2012**, 2, 206−219.
3. Keen, D. A.; Goodwin, A. L. The crystallography of correlated disorder. *Nature*. **2015**, 521, 303−309.
4. Clarke, S. J.; Adamson, P.; Herkelrath, S. J.; Rutt, O. J.; Parker, D. R.; Pitcher, M. J.; Smura, C. F. Structures, physical properties, and chemistry of layered oxychalcogenides and oxypnictides. *Inorg. Chem*. **2008**, 47, 8473−8486.
5. Valldor, M. Anion Ordering in Bichalcogenides. *Inorganics*. **2016**, 4, 23.
6. Broadley, S.; Gal, Z. A.; Cora, F.; Smura, C. F.; Clarke, S. J. Vertex-linked ZnO2S2 tetrahedra in the oxysulfide BaZnOS: a new coordination environment for zinc in a condensed solid. *Inorg. Chem*. **2005**, 44, 9092−9096.
7. Zhu, W. J.; Hor, P. H. Crystal Structure of New Layered Oxysulfides: Sr3Cu2Fe2O5S2and Sr2CuMO3S (M = Cr, Fe, In). *J. Solid State Chem*. **1997**, 134, 128−131.
8. Pearson, R. G. Hard and Soft Acids and Bases. *J. Am. Chem. Soc*. **1963**, 85, 3533−3539.
9. Goto, Y.; Seo, J.; Kumamoto, K.; Hisatomi, T.; Mizuguchi, Y.; Kamihara, Y.; Katayama, M.; Minegishi, T.; Domen, K. Crystal Structure, Electronic Structure, and Photocatalytic Activity of Oxysulfides: La2Ta2ZrS2O8, La2Ta2TiS2O8, and La2Nb2TiS2O8. *Inorg. Chem*. **2016**, 55, 3674−3679.
10. Yashima, M.; Ogisu, K.; Domen, K. Structure and electron density of oxysulfide Sm2Ti2S2O4.9, a visible-light-responsive photocatalyst. *Acta Crystallogr., Sect. B:*

Struct. Sci. **2008**, 64, 291−298.

11. Kabbour, H.; Sayede, A.; Saitzek, S.; Lefevre, G.; Cario, L.; Trentesaux, M.; Roussel, P. Structure of the water-splitting photocatalyst oxysulfide α-LaOInS2 and ab initio prediction of new polymorphs. *Chem. Commun*. **2020**, 56, 1645−1648.
12. Wang, Q.; Nakabayashi, M.; Hisatomi, T.; Sun, S.; Akiyama, S.; Wang, Z.; Pan, Z.; Xiao, X.; Watanabe, T.; Yamada, T.; Shibata, N.; Takata, T.; Domen, K. Oxysulfide photocatalyst for visible-lightdriven overall water splitting. *Nat. Mater*. **2019**, 18, 827−832.
13. Ogisu, K.; Ishikawa, A.; Teramura, K.; Toda, K.; Hara, M.; Domen, K. Lanthanum−Indium Oxysulfide as a Visible Light Driven Photocatalyst for Water Splitting. *Chem. Lett*. **2007**, 36, 854−855.
14. Tsujimoto, Y.; Juillerat, C. A.; Zhang, W.; Fujii, K.; Yashima, M.; Halasyamani, P. S.; zur Loye, H.-C. Function of Tetrahedral ZnS3O Building Blocks in the Formation of SrZn2S2O: A Phase Matchable Polar Oxysulfide with a Large Second Harmonic Generation Response. *Chem. Mater*. **2018**, 30, 6486−6493.
15. Sambrook, T.; Smura, C. F.; Clarke, S. J.; Ok, K. M.; Halasyamani, P. S. Structure and physical properties of the polar oxysulfide CaZnOS. *Inorg. Chem*. **2007**, 46, 2571−2574.
16. Nishioka, S.; Kanazawa, T.; Shibata, K.; Tsujimoto, Y.; Zur Loye, H. C.; Maeda, K. A zinc-based oxysulfide photocatalyst SrZn2S2O capable of reducing and oxidizing water. *Dalton Trans*. **2019**, 48, 15778−15781.
17. Fjellvag, O. S.; Nygard, K. H.; Vajeeston, P.; Sjastad, A. O. Advances in the LiCl salt flux method and the preparation of phase pure La2-xNdxLiHO3 (0 < /= x < /= 2) oxyhydrides. *Chem. Commun*. **2019**, 55, 3817−3820.
18. Hosono, A.; Masubuchi, Y.; Yasui, S.; Takesada, M.; Endo, T.; Higuchi, M.; Itoh, M.; Kikkawa, S. Ferroelectric BaTaO2N Crystals Grown in a BaCN2 Flux. *Inorg. Chem*. **2019**, 58, 16752−16760.

19. Zhong, C.; Kato, D.; Takeiri, F.; Fujii, K.; Yashima, M.; Nishiwaki, E.; Fujii, Y.; Koreeda, A.; Tassel, C.; Abe, R.; Kageyama, H. Single Crystal Growth of Sillén−Aurivillius Perovskite Oxyhalides Bi4NbO8X (X = Cl, Br). *Inorganics*. **2018**, 6, 41.

20. Juillerat, C. A.; Moore, E. E.; Morrison, G.; Smith, M. D.; Besmann, T.; Zur Loye, H. C. Versatile Uranyl Germanate Framework Hosting 12 Different Alkali Halide 1D Salt Inclusions. *Inorg. Chem*. **2018**, 57, 11606−11615.

21. Zhang, X.; Xiao, Y.; Wang, R.; Fu, P.; Zheng, C.; Huang, F. Synthesis, crystal structures and optical properties of noncentrosymmetric oxysulfides AeGeS2O (Ae = Sr, Ba). *Dalton Trans*. **2019**, 48, 14662−14668.

22. Blandy, J. N.; Liu, S.; Smura, C. F.; Cassidy, S. J.; Woodruff, D. N.; McGrady, J. E.; Clarke, S. J. Synthesis, Structure, and Properties of the Layered Oxide Chalcogenides Sr2CuO2Cu2S2 and Sr2CuO2Cu2Se2. *Inorg. Chem*. **2018**, 57, 15379−15388.

23. Lei, H.; Ryu, H.; Ivanovski, V.; Warren, J. B.; Frenkel, A. I.; Cekic, B.; Yin, W.-G.; Petrovic, C. Structure and physical properties of the layered iron oxychalcogenide BaFe2Se2O. *Phys. Rev. B: Condens. Matter Mater. Phys*. **2012**, 86, 195133.

24. Nagao, M.; Miura, A.; Urushihara, D.; Maruyama, Y.; Goto, Y.; Mizuguchi, Y.; Moriyoshi, C.; Kuroiwa, Y.; Wang, Y.; Watauchi, S.; Asaka, T.; Takano, Y.; Tadanaga, K.; Tanaka, I. Flux Growth and Superconducting Properties of (Ce,Pr)OBiS2 Single Crystals. *Front. Chem*. **2020**, 8, 44.

25. Krause, L.; Herbst-Irmer, R.; Sheldrick, G. M.; Stalke, D. Comparison of silver and molybdenum microfocus X-ray sources for single-crystal structure determination. *J. Appl. Crystallogr*. **2015**, 48, 3−10.

26. APEX3, ver. 2016.5-0; Bruker AXS: Madison, WI, USA, **2016**. SAINT+, ver. 8.37A; Bruker AXS: Madison, WI, USA, **2016**.

27. Sheldrick, G. M. Crystal structure refinement with SHELXL. *Acta Crystallogr., Sect.*

C: Struct. Chem. **2015**, 71, 3−8.

28. Hubschle, C. B.; Sheldrick, G. M.; Dittrich, B. ShelXle: a Qt graphical user interface for SHELXL. *J. Appl. Crystallogr*. **2011**, 44, 1281−1284.

29. Izumi, F.; Momma, K. Three-Dimensional Visualization in Powder Diffraction. *Solid State Phenom*. **2007**, 130, 15−20.

30. Blochl, P. E. Projector augmented-wave method. *Phys. Rev. B: Condens. Matter Mater. Phys*. **1994**, 50, 17953−17979.

31. Kresse, G.; Joubert, D. From ultrasoft pseudopotentials to the projector augmented-wave method. *Phys. Rev. B: Condens. Matter Mater. Phys*. **1999**, 59, 1758−1775.

32. Kresse, G.; Hafner, J. Ab initio molecular dynamics for liquid metals. *Phys. Rev. B: Condens. Matter Mater. Phys*. **1993**, 47, 558−561.

33. Kresse, G.; Furthmüller, J. Efficiency of ab-initio total energy calculations for metals and semiconductors using a plane-wave basis set. *Comput. Mater. Sci*. **1996**, 6, 15−50.

34. Kresse, G.; Furthmuller, J. Efficient iterative schemes for ab initio total-energy calculations using a plane-wave basis set. *Phys. Rev. B: Condens. Matter Mater. Phys*. **1996**, 54, 11169−11186.

35. Schimka, L.; Harl, J.; Kresse, G. Improved hybrid functional for solids: the HSEsol functional. *J. Chem. Phys*. **2011**, 134, No. 024116.

36. Shannon, R. D. Revised effective ionic radii and systematic studies of interatomic distances in halides and chalcogenides. *Acta Crystallogr., Sect. A: Cryst. Phys., Diffr., Theor. Gen. Crystallogr*. **1976**, 32, 751−767.

37. Brese, N. E.; O'Keeffe, M. Bond-valence parameters for solids. *Acta Crystallogr., Sect. B: Struct. Sci*. **1991**, 47, 192−197.

38. Teske, C. L. Über Oxidsulfide mit Åkermanitstruktur CaLaGa3S6O, SrLaGa3S6O, La2ZnGa2S6O und Sr2ZnGe2S6O. *Z. Anorg. Allg. Chem*. **1985**, 531, 52−60.

39. Endo, T.; Doi, Y.; Wakeshima, M.; Suzuki, K.; Matsuo, Y.; Tezuka, K.; Ohtsuki, T.;

Shan, Y. J.; Hinatsu, Y. Magnetic Properties of the Melilite-Type Oxysulfide Sr2MnGe2S6O: Magnetic Interactions Enhanced by Anion Substitution. *Inorg. Chem*. **2017**, 56, 2459−2466.

40. Krebs, B.; Wallstab, H.-J. Thio-hydroxo Anions of Germanium: Preparation, Structure and Properties of Na2GeS2(OH)2 · 5H2O. *Z. Naturforsch., B: J. Chem. Sci*. **1981**, 36, 1400−1406.

41. Berastegui, P.; Hull, S.; Garcı Garcı, F. J.; Grins, J. A Structural Investigation of La2(GeO4)O and Alkaline-Earth-Doped La9.33(GeO4)6O2. *J. Solid State Chem*. **2002**, 168, 294−305.

42. León-Reina, L.; Losilla, E. R.; Martínez-Lara, M.; Bruque, S.; Aranda, M. A. G. Interstitial oxygen conduction in lanthanum oxyapatite electrolytes. *J. Mater. Chem*. **2004**, 14, 1142−1149.

43. Kubelka, P.; Munk, F. Ein Beitrag Zur Optik Der Farbanstriche. *Z. Techn. Phys*. **1931**, 12, 593−601.

44. Inaguma, Y. Lithium ion conductivity in the perovskite-type LiTaO3-SrTiO3 solid solution. *Solid State Ionics*. **1995**, 79, 91−97.

Chapter 5. Flux Crystal Growth, Crystal Structure, and Optical Properties of New Germanate Garnet $Ce_2CaMg_2Ge_3O_{12}$

5.1 Introduction

The optical performances of garnet compounds have been widely investigated. As a host material for a variety of optical applications, gernet compounds have been developed for laser amplifiers, scintillators, and cathode ray phosphors.[1] For example, the Ce^{3+} doped $Y_3Al_5O_{12}$ garnet phosphor (YAG:Ce), which converts blue light to yellow, is one of the most interesting practical optical material for the application of white-emitting diodes. However, the efficiency of YAG:Ce decreases at high temperature, therefore, the improvements of quenching temperature and cool corelated colar temperature remain chanllenges for scientists.[2-4] In general, the variation of the light output was proved to be complicated, involving variations in the absorption intensity of the 5*d*-4*f* band and the temperature dependent transfer of energy to the defects. With regards to the host material, there are three types of cation sites as seeing from the general chemical formula of garnet structure $\{A\}_3[B]_2(C)_3O_{12}$: the {A} site with 8-fold dodecahedral coordination by 24*c* as Wyckoffposition, the [B] site with 6-fold octahedral coordination (16*a*), and the (C) site with 4-fold tetrahedral coordination (24*d*) (Figure 5.1). All the oxygen atoms occupy tetrahedral sites (96*h*). The dodecahedral {A} site can be occupied by Y^{3+}, Gd^{3+}, Lu^{3+}, Tb^{3+}, Ca^{2+}, Sr^{2+}, and Mg^{2+}; the octahedral [B] site can be occupied by Al^{3+}, Ga^{3+}, In^{3+}, Sc^{3+}, Y^{3+}, Mg^{2+}, Fe^{3+}, Cr^{3+}; and the tetrahedral (C) site canbe occupied by Al^{3+}, Ga^{3+}, Si^{4+}, Ge^{4+}. The cationic combinations at {A}, [B], (C) sites are different and limited by the relationship between ionic radius and valence state. The Ce^{3+} ion prefers to occupy the dodecahedral {A} site, which is conner and edge shared with the adjacent B and C sites. Therefore, understanding the local structure of {A}, [B], and (C) is of significance for the investigation of garnet optical performances.[5-7] Due to the wide range of cations contained in

the garnet structure, new garnet phosphor compositions have been successfully synthesized to compensate the above shortcomings of YAG:Ce.

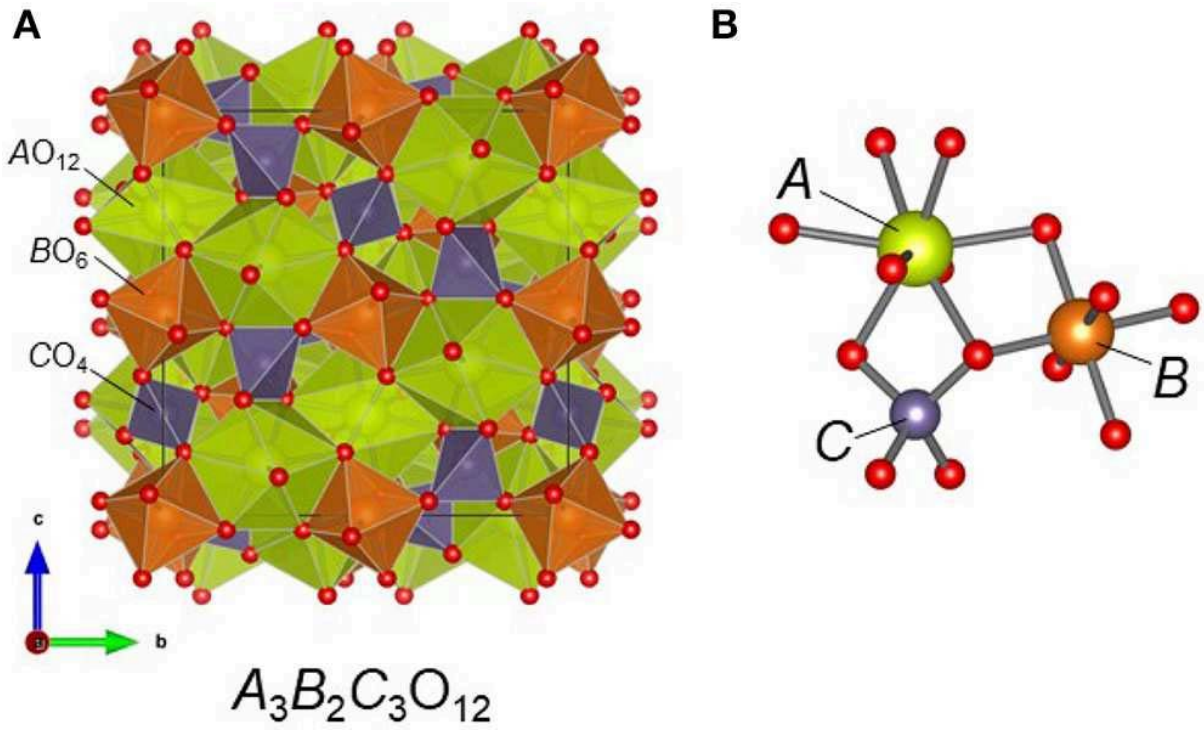

Figure 5.1. (A) Crystal structure of the garnet compound $A_3B_2C_3O_{12}$ and (B) the local coordination environment around the metal cations. In $Ce_2CaMg_2Ge_3O_{12}$, Ce/Ca, Mg, and Ge atoms occupy the A, B, and C sites, respectively.

When considering the crystal chemistry of the garnet family, the ability of the cation sites, especially the A site, to accommodate different elements, is an important factor.[8] A large number of garnet compounds have been previously reported but the variety of RE ions in the A site is typically limited to RE = Gd–Lu and Y,[9-11] all smaller than the desirable Eu3+ cation, because incorporation of larger cation causes markedly unfavorable lattice distortions around the dodecahedral sites. To the best of our knowledge, only very few garnet compositions that include early RE ions larger than Gd^{3+} have been synthesized (via various techniques such as the sol-gel method and hydrothermal reaction), and include: $Eu_3Al_5O_{12}$,[12] $RE_3Te_2Li_3O_{12}$ (RE = Pr–Eu),[13] $RE_3W_2Li_3O_{12}$ (RE = Pr, Nd),[13] $RE_3Fe_5O_{12}$ (RE = Pr–Eu),[14-17] $La_3Sc_2Ga_3O_{12}$,[18] $RE_3Ga_5O_{12}$ (RE = Pr–Eu),[19,20] $Li_7La_3Zr_2O_{12}$,[21] and $Li_5La_3Sb_2O_{12}$.[22] It is notable that even

among these, achieving a garnet composition with Ce^{3+} fully occupying the A site is challenging; however, Ce^{3+} doping as high as 56 at.% with respect to Y^{3+} has been achieved in YFe_5O_{12} via the glycothermal process.[23]

In this chapter, we report new germanate oxide single crystals $\{Ce_2Ca\}[Mg]_2(Ge)_3O_{12}$, which were obtained via flux growth method from a $BaCl_2$-$CaCl_2$ eutectic mixture. Although it is single anion oxide, which is different from the mixed-anion oxysulfides in the above two chapters, it is still an important product from the flux growth method, which Ce cation is stabilized in {A} site. The crystal structure, electronic structure, and optical properties will be given in this chapter.

5.2. Experimental details of Chapter 5

Reagents. CeO_2 (Aldrich, 4N), GeO_2 (Rare Metallic, 99.99%), S (High Purity Materials, 4N), $BaCl_2$ (Rare Metallic, 99.9%), and $CaCl_2$ (Rare Metallic, 99.99%) were used as received. Before use, two chlorides were heated overnight in a dry oven at 260°C. All the raw materials were stored in an argon-filled glove box.

Crystal Growth. $Ce_2CaMg_2Ge_3O_{12}$ single crystals were grown out of a $BaCl_2$-$CaCl_2$ eutectic flux.[24] CeO_2 (1.0 mmol), GeO_2 (1.0 mmol), S (1.0 mmol), $BaCl_2$ (3.1 mmol) and $CaCl_2$ (3.1 mmol) were placed into a magnesia crucible in an Ar-filled glove box. As described later, the magnesia crucible was found to act as a magnesium source. The crucible was fused in a vacuum of 1 Pa and sealed by flame in a quartz tube. The raw material was heated to 900℃ at 150℃/h in muffle furnace for 25 h and cooled to 500℃ at 5 ℃/h. Finally, the heater was turned off and cooled naturally to room temperature. The products were washed in distilled water, aided by sonication, before the reddish-orange transparent truncated spherical crystals of $Ce_2CaMg_2Ge_3O_{12}$, together with pale-purple transparent crystals of CeOCl, were collected via vacuum filtration. The typical dimensions of the single crystals of the garnet compound were 0.3 × 0.3 × 0.3 mm3. The structure of $Ce_2CaMg_2Ge_3O_{12}$ was determined by single-crystal

X-ray diffraction analysis.

Since our original target system was germanium-based oxysulfide, we inadvertently obtained $Ce_2CaMg_2Ge_3O_{12}$ single crystals. As described later, sulfur is not incorporated into the garnet structure, nor is oxysulfide available.

Single Crystal Structure Analysis. X-ray intensity data for the orange polyhedron were collected at 301(2)K using a Bruker D8 QUEST diffractometer equipped with a PHOTON 100 CMOS region detector and an Incoatec microfocusing source (Mo Kα radiation, λ = 0.71073 Å).[25] Data were collected covering 100% of the reciprocal space $2\theta_{max}$ = 75.2◦, with average reflection redundancy of 35.3 and R_{int} = 0.064 after absorption correction. SAINT+ and SADABS programs were used to reduce and correct the original region detector data frames to cope with absorption effects.[26,] The final cell cell parameters are determined by least square refinement of 3812 reflections on the dataset. The initial structural model was obtained using SHELXT.[27] Subsequent differential Fourier calculations and full matrix least-squares refinement of F2 were performed using SHELXL-2018 using the ShelXle interface.[28]

Solid State Synthesis. Polycrystalline powder sample $Ce_2CaMg_2Ge_3O_{12}$ was synthesized with CeO_2, $CaCO_3$(or CaO), MgO and GeO_2 according to stoichiometric ratio. The mixture was intimately ground, pelletized, and heated in a flowing N_2 or H_2 (20%) -Ar (80%) mixed gas atmosphere, or in a vacuum sealed tube using a tubular furnace at temperatures ranging from 900 to 1300 ◦C.

XRD, UV-vis, PL, PLE, and Magnetic Measurements. The single crystals of $Ce_2CaMg_2Ge_3O_{12}$ were pulverized with agate mortar to obtain fine powder, which was used to obtain synchronous X-ray powder diffraction (SXRD) pattern, UV-vis diffuse reflectance spectrum, photoluminescence (PL) and photoluminescence excitation (PLE) spectrum. The powder XRD analysis of the products obtained by solid reaction was performed with Rigaku MiniFlex X-ray diffractometer (Cu Kα radiation) in the 2θ range of 5-65◦ with step size of 0.04◦. SXRD measurements were made at room temperature using a one-dimensional detector

mounted on BL15XU, NIMS beamline at SPring-8 in Japan. Synchrotron radiation X-rays are monochrome with A wavelength of 0.65298 Å. The $Ce_2CaMg_2Ge_3O_{12}$ powder sample was packed into a 0.1mm diameter glass capillary. Diffraction data were recorded in 0.003◦ increments ranging from 2 to 60◦ and analyzed using the Rietveld refinement program Rietan-FP.[29] Diffuse reflection coefficients were measured at room temperature using a Shimadzu UV-2600 spectrophotometer equipped with an ISR-2600Plus integrating sphere. The diffuse reflection data were converted into absorbance within the instrument by the Kubelka-Munk function. A fluorescence spectrophotometer (Hitachi F-7000) was used to record the spectral lines and emission spectra. Magnetic susceptibility of $Ce_2CaMg_2Ge_3O_{12}$ was measured with a SQUID magnetometer (Quantum Design, MPMS-XL). The single crystals crushed by an external magnetic field (H) in the range of 10 ~ 300 K were measured under zero-field-cooling (ZFC) and field-cooling (FZ) conditions respectively.

First-Principles Calculations. First-principles total energy calculations of $Ce_2CaMg_2Ge_3O_{12}$ were performed using the projector augmented wave method (PAW) as implemented in the Vienna Ab-initio Simulation Package (VASP).[30-34] In this study, the cutoff energy of the plane wave basis is 550 eV. The commutation-related interaction potentials of electrons are handled within the framework of the Generalized Gradient approximation (GGA) of the PBEsol type.[35] The valence electron configurations of Ce-$5s^2$, $5p^6$, $4f^1$, $5d^1$, $6s^2$, Ca-$3s^2$, $3p^6$, $4s^2$, Mg-$2p^6$, $3s^2$, Ge-$3d^{10}$, $4s^2$, $4p^2$, and O-$2s^2$, $2p^4$, respectively. The spin polarization is calculated. For Ce ion, GGA+U method was adopted to deal with the strongly correlated interaction effect of 4*f* orbital.[36] The U value in this study was set as 5.4 eV. The structural optimization was carried out when the residual force was 0.02eV/Å.[37,38]

5.3. Results and discussion

5.3.1. Crystal Growth and Structure Determination.

After rinsing the products in the magnesium crucible with water to remove the solidified flux, we found red single crystals growing on the inner wall of the tube (Figure 5.2) alongside the plate-like mauve crystal CeOCl by-product. EDS analysis of red-orange crystals shows that the atomic ratios of Ce, Ca, Mg and Ge are about 1.9:1.1:2.1:2.6. The source of magnesium is a magnesium oxide crucible, which is apparently slightly dissolved by the flux during the reaction. Single crystal X-ray diffraction analysis showed that the product crystallized in cubic system, a = 12.5479(4) Å. Space group $Ia\bar{3}d$ (Space group No. 230) is uniquely determined by the systematic absences pattern in the intensity data and is determined by the structural solution. The product has a garnet-shaped structure in which the asymmetric unit consists of one hybrid Ce/Ca atomic site (Wyckoff site 24*c*), one Ge site (24*d*), one Mg site (16*a*), and one O site (96*h*). The composition of the 24*c* site was determined by an improved test of several models containing the cationic elements present in crystals determined by EDS (i.e. only Ce, Ca, Mg and Ge). The most reasonable model is modeled with mixed Ce/Ca occupying positions, and ion radii similar to them (r_{Ce}^{3+} = 1.143 Å, r_{Ca}^{2+} = 0.97 Å)[39] and their observed bond distances with O [2.427(4) and 2.547(4) Å]. To maintain the overall charge balance, the occupancy of Ce and Ca is fixed at 2/3 Ce and 1/3 Ca. All atoms are refined with anisotropic displacement parameters. The chemical composition was $Ce_2CaMg_2Ge_3O_{12}$, which was consistent with EDS analysis. Finally, R_1 and wR_2 converge to reasonable values of 3.83 and 5.51%, respectively. The goodness of fit value was 1.29. The incorporation of Ce^{3+} ions in the structure is consistent with the red-orange color of the sample. Table 5.1 lists the details of the structure refinements. Atomic coordinates and atomic displacement parameters are listed in Table 5.2 and Table 5.3 respectively. The selected key distances and key angles are listed in Table 5.4.

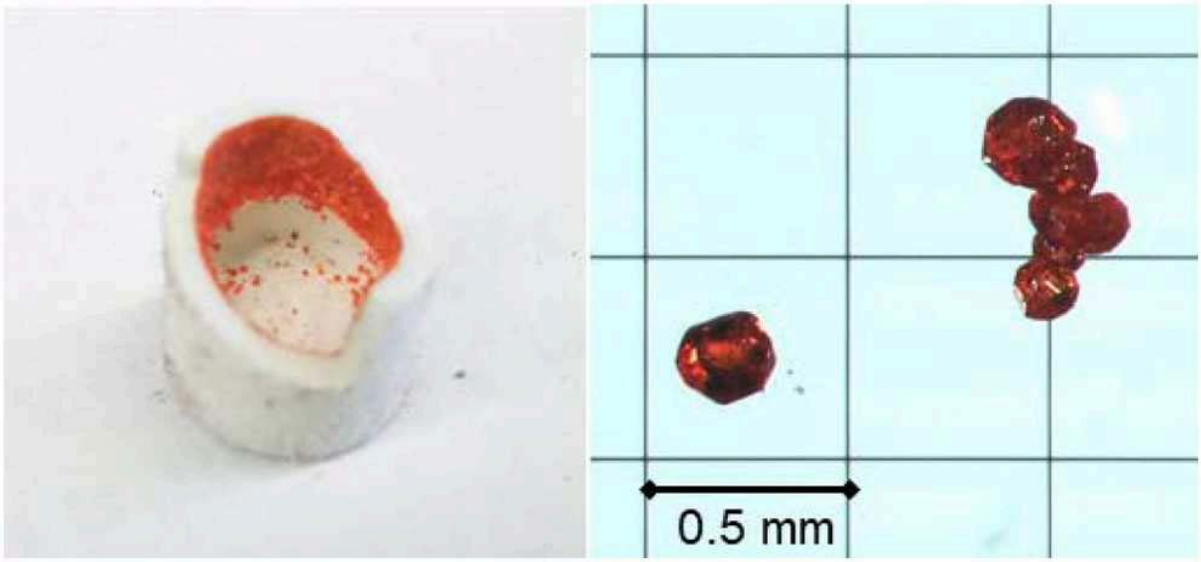

Figure 5.2. Photographs of single crystals of $Ce_2CaMg_2Ge_3O_{12}$ grown on the inner wall of a MgO crucible.

Table 5.1. Results of the Structure Refinement of $Ce_2CaMg_2Ge_3O_{12}$ Using Single-Crystal X-ray Diffraction.

Formula	$Ce_2CaMg_2Ge_3O_{12}$
Formula weight	778.83
Radiation	Mo Kα (λ = 0.71073 Å)
***T* (K)**	301(2)
Crystal system	Cubic
Space group	*Ia*-3*d*
***a* (Å)**	12.5487 (3)
***V* (Å^3)**	1976.04 (14)
Z	8
D_{calc} **(g/cm^3)**	5.235
no. of measured reflns	17162
no. of unique reflns	445
R_{int} **(%)**	6.45
$R[F^2 > 2\sigma(F^2)]/wR(F^2)$ **(%)**	3.83/5.51
GoF	1.286

Table 5.2. Crystallographic and Refinement Data Obtained from Single-Crystal Structure Analysis of $Ce_2CaMg_2Ge_3O_{12}$.

atom	site	*x*	*y*	*z*	occupancy	U_{iso}/ Å^2
Ce	24*c*	1/8	0	1/4	0.667	0.737 (15)
Ca	24*c*	1/8	0	1/4	0.333	0.737 (15)
Mg	16*a*	0	0	0	1	0.75 (5)
Ge	24d	3/8	0	1/4	1	0.0660 (18)
O	96h	0.0948 (2)	0.1976 (3)	0.2852 (3)	1	0.68 (5)

Table 5.3. Anisotropic displacement parameters U_{ij} ($10^2 \times$Å^2) for $Ce_2CaMg_2Ge_3O_{12}$ obtained from the structure refinement using single-crystal XRD data.

atom	U_{11}	U_{22}	U_{33}	U_{23}	U_{13}	U_{12}
Ce	0.63(2)	0.791(18)	0.791(18)	0.05(2)	0	0
Ca	0.63(2)	0.791(18)	0.791(18)	0.05(2)	0	0
Mg	0.75(5)	0.75(5)	0.75(5)	-0.05(8)	-0.05(8)	-0.05(8)
Ge	0.72(3)	0.63(2)	0.63(2)	0	0	0
O	0.52(11)	0.78(12)	0.75(12)	0	0.16(10)	0.12(9)

Table 5.4. Selected interatomic distances and bond angles of $Ce_2CaMg_2Ge_3O_{12}$ at 301 K.

bond distance (Å)			bond angle (°)
Ce/Ca–O × 4	2.427 (4)	Ce/Ca–O–Mg	97.48 (12)
Ce/Ca –O × 4	2.547 (4)	Ce/Ca–O–Mg	101.26 (15)
Mg–O × 6	2.102 (3)	Ce/Ca –O–Ge × 2	95.60 (13)
Ge–O × 4	1.766 (3)	Ce/Ca–O–Ce/Ca × 2	101.13 (14)

Figure 5.3 shows the room-temperature synchronous X-ray diffraction patterns collected from powder samples obtained from fine grinding of hand-selected single crystals. Rietveld refinement was carried out using the model determined by single crystal structure analysis. The model fits smoothly and the reliability index is reasonable, R_{wp} = 5.37, R_B = 3.45,

R_F = 2.92, which can reproduce the observation model well. The final refined crystal data, including atomic coordinates and isotropic displacement parameters, are listed in Table 5.5. The results are consistent with those of single crystal structure analysis.

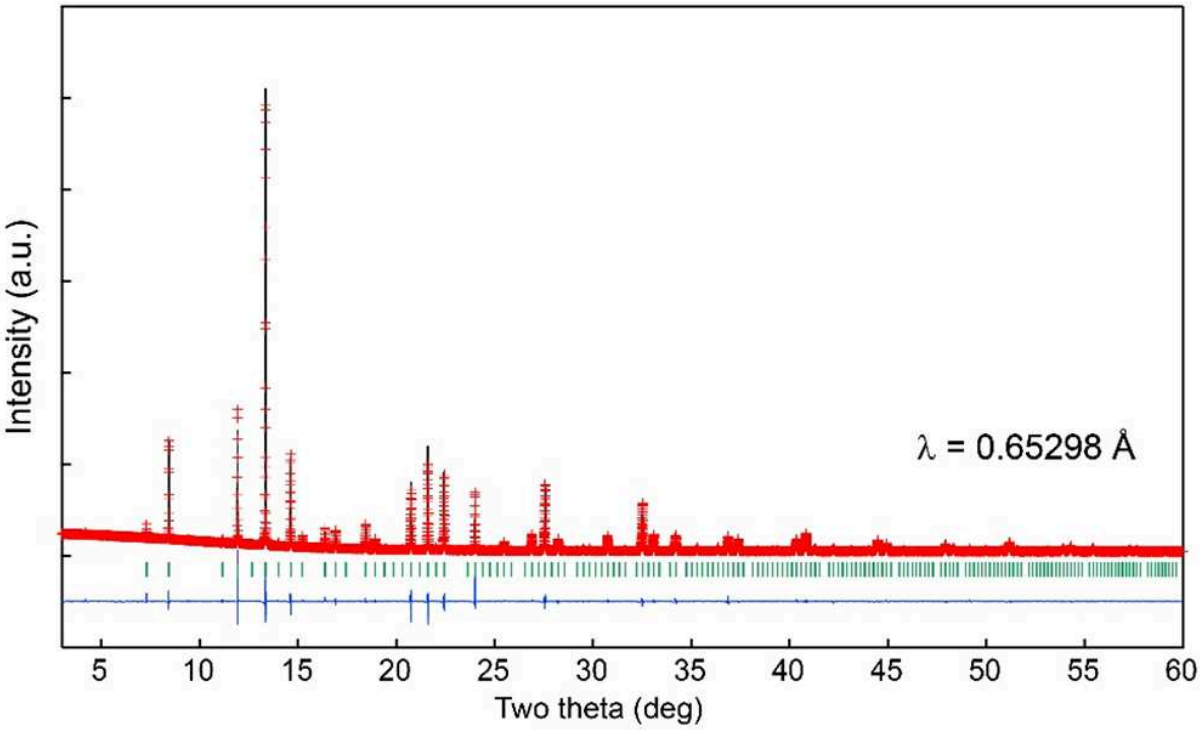

Figure 5.3. Observed (crosses), calculated (upper solid line), and difference (lower solid line) plots obtained from the Rietveld analysis of the room temperature synchrotron X-ray powder.

Table 5.5. Atomic coordinates and isotropic displacement parameters U_{iso} refined from SXRD data collected from $Ce_2CaMg_2Ge_3O_{12}$ at room temperature.

atom	site	*x*	*y*	*z*	occupancy	U_{iso}/ Å^2
Ce	24*c*	1/8	0	1/4	0.667	0.43(2)
Ca	24*c*	1/8	0	1/4	0.333	0.43(2)
Mg	16*a*	0	0	0	1	0.15(4)
Ge	24d	3/8	0	1/4	1	0.56(2)
O	96h	0.0944(2)	0.1966(2)	0.2880(2)	1	0.27(7)

5.3.2. Solid State Reaction.

A stoichiometric mixture of CeO_2, $CaCO_3$ (or CaO), MgO and GeO_2 was used to synthesize polycrystalline $Ce_2CaMg_2Ge_3O_{12}$ by solid state reaction. The reaction took place under vacuum, mixing H_2(20%) -Ar (80%) gas or N_2 gas at 900 and 1300◦C. Unfortunately, none of the reaction conditions we examined produced the target phase; However, large amounts of unreacted CeO_2 remain in the product throughout (Figure 5.4). Garnet structure as a secondary phase in 1300◦C in N_2 gas atmosphere; The lattice parameters of garnet phase are 0.5% smaller than those of $Ce_2CaMg_2Ge_3O_{12}$, and the product is dark gray. Therefore, if Ce atoms are added to the lattice, the Ce concentration of the garnet phase obtained in the solid phase should be lower than $Ce_2CaMg_2Ge_3O_{12}$. After further heating at the same temperature, the garnet phase partially decomposed and CeO2 content increased, indicating that the garnet phase was in metastable state under this reaction condition.

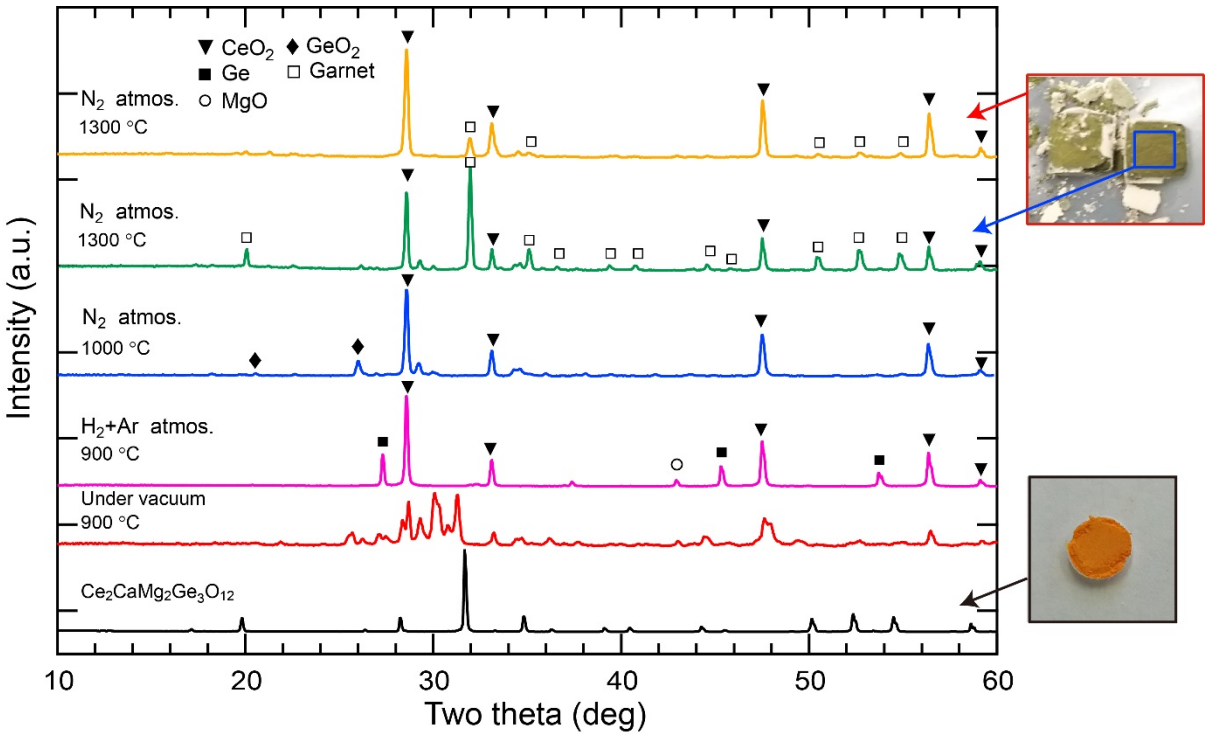

Figure 5.4. Powder XRD patterns of the products obtained from the solid-state reactions. For comparison, the PXRD data of the powder sample of $Ce_2CaMg_2Ge_3O_{12}$ which was obtained by

crushing the single crystals is plotted together. The reaction at 900 °C in an evacuated tube resulted in a complex powder pattern. GeO_2 was reduced to Ge metal in H_2(20%)+Ar(80%) mixture gas atmosphere. Several peaks which could be assigned to the garnet structure were observed from the product heated at 1300 °C in N_2 gas atmosphere, but the lattice constant was smaller by 0.5% than that for $Ce_2CaMg_2Ge_3O_{12}$. The sample color was also different from the reddish-orange color of $Ce_2CaMg_2Ge_3O_{12}$.

5.3.3. Stability of the Garnet Structure.

As mentioned above, garnet structures can accommodate a wide range of elements at three different cation locations, but the potential stability of garnet structures, including their tolerance to rare earth ions, is unknown. Our current garnet germaniate shows that two thirds of site A is occupied by Ce^{3+} ions at concentrations much higher than 56 at.% Ce^{3+} doping concentration is found in $Y_{1-x}Ce_xFe_5O_{12}$ (x = 1.7). More recently, Song et al. have formulated the tolerance factor (τ) for garnet structure[40], which is similar to the Goldschmidt tolerance factor for the relationship between chemical composition and structural stability in perovskite.[41] The τ expression of garnet structure is

$$\tau = \frac{\sqrt[3]{(r_{B+}r_0)^2+\frac{4}{9}(r_{A+}r_0)^2}}{2(r_{C+}r_0)}$$

where r_A, r_B, r_C and r_O are the ionic radii of cations at A, B and C sites and O^{2-} ions, respectively. The tolerance coefficients for more than 100 garnet compounds are in the range 0.75-1.33. For $RE_3B_2C_3O_{12}$. (RE = La-Lu, Y; B = C= Fe, Al, Ga) and τ values increase systematically with the decrease of the size of RE ions, such as 0.76-0.93 for $RE_3Al_5O_{12}$ from La to Lu and 0.89-1.02 for $RE_3Fe_5O_{12}$. This is consistent with the general trend of structural stability observed in the presence of rare earth ions. The formula $RE_2CaMg_2Ge_3O_{12}$ (RE = La-lu, Y), including hypothetical components, shows a similar tolerance factor size dependence, but τ values range from 1.06 for La, to 1.07 for Ce, to 1.15 for Lu. The stability of $Ce_2CaMg_2Ge_3O_{12}$ at τ values

close to uniform seems to meet the geometric requirements of garnet structure. However, good tolerance factors do not guarantee the successful formation of the target phase of chemical synthesis. In fact, the solid reaction we detected to yield $Ce_2CaMg_2Ge_3O_{12}$ was not successful. At present, it is not clear why a large number of Ce ions enter the lattice of garnet. However, under flux reaction conditions, the molten salts used in this study may play a crucial role in stabilizing the phase. According to the PXRD data of the products obtained from the solid phase reaction, CeO_2 was not completely consumed in the reaction, indicating that its reaction activity was low and atomic diffusion was slow even at high temperature. In flux reactions, $BaCl_2$−$CaCl_2$ salts are likely to dissolve CeO_2 powders at lower temperatures while the raw materials are in solution, which greatly reduces the activation energy of the reaction between the raw materials, resulting in the formation of the target garnet phase. It is speculated that the Ca-Cl melt acts as a reducing agent for Ce ion at high vacuum and high temperature and is likely to form Cl_2. The formation of Ce^{3+} in halide melt is beneficial to the stability of $Ce_2CaMg_2Ge_3O_{12}$ and the by-product CeOCl. Sulfur, as the initial substance of flux reaction, has no significant contribution to the reduction of Ce ion and the formation of $Ce_2CaMg_2Ge_3O_{12}$. When the flux crystal is grown without sulfur, the same mixture will be produced.

5.3.4. Optical and Magnetic Properties.

Figure 5.5A shows the UV-Vis absorption spectrum of $Ce_2CaMg_2Ge_3O_{12}$, with a clear absorption edge near 560nm. Extrapolating the linear part of the absorption curve to the X-axis shows that the optical band gap is E_g = 2.22 eV. With the rapid increase of absorption, two broad subbands centered at 458 nm and 305 nm also appear in the UV-visible absorption curve of YAG:Ce. These two absorption peaks can be attributed to optical transitions from the ground state of Ce-4*f* to the lowest and second lowest excited states ($5d^1$ and $5d^2$, respectively) of the Ce-5*d* orbit. A third weak peak near 250 nm may be due to defects or impurities. The lowest

absorption is in the blue region of the spectrum, which results in a red-orange garnet compound. The photoluminescence (PE) and excitation (PLE) spectra of $Ce_2CaMg_2Ge_3O_{12}$ are shown in Figure 5.5B. The PE spectrum excited at 519 nm contains a wide band centered at 600 nm, which may be a transition from the $5d^1$ energy level to two $4f$ energy levels, which split into $^2F_{5/2}$ and $^2F_{7/2}$ by spin-orbital coupling. The maximum emission band of $Ce_2CaMg_2Ge_3O_{12}$ is redshifted compared with $Y_2Mg_3Ge_3O_{12}$:Ce(2%)[42], but compared with $Gd_2Mg_3Ge_3O_{12}$:Ce(2%)[43].

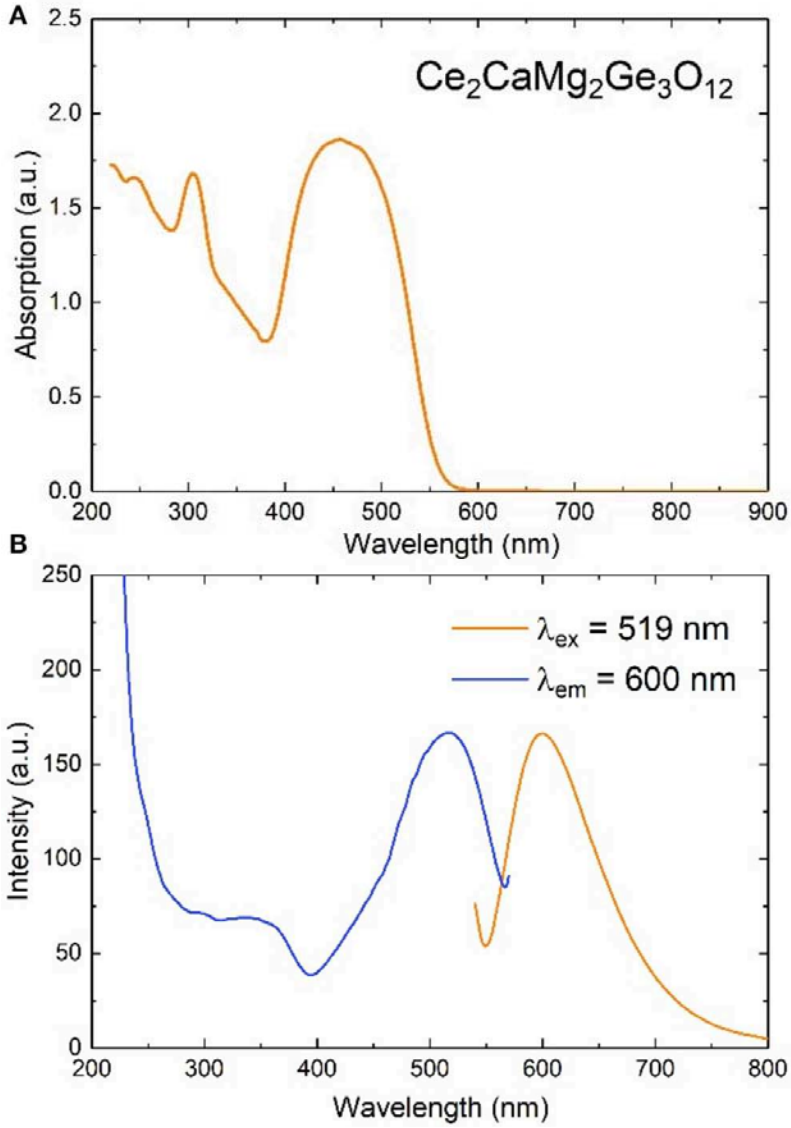

Figure 5.5. (A) UV–vis absorption spectrum, and (B) photoluminescence emission (λ_{ex} = 519 nm) and excitation (λ_{em} = 600 nm) spectra for $Ce_2CaMg_2Ge_3O_{12}$, collected at room temperature.

Figure 5.6 shows the temperature evolution of magnetic susceptibility χ (= M/H) in H = 1 kOe magnetic field. Both ZFC and FC data increase steadily with the decrease of temperature, indicating that the paramagnetic state is still maintained at low temperature. There is no significant difference between ZFC and FC data in the temperature range of 10-300 K. Fitting the Curie-Weiss law with χ (T) yields C = 1.407(4) (emu K/mol) and θ = −59.9(9) K, where C and θ represent the Curie and Weiss constant, respectively. The C value of two moles of Ce^{3+} is slightly less than the theoretical value, and the unit of each formula is $^2F_{5/2}$. Negative θ values indicate antiferromagnetic coupling between Ce^{3+} ions. The absence of long-range magnetic sequence may be due to the random distribution of Ce and Ca atoms at the 24*c* position.

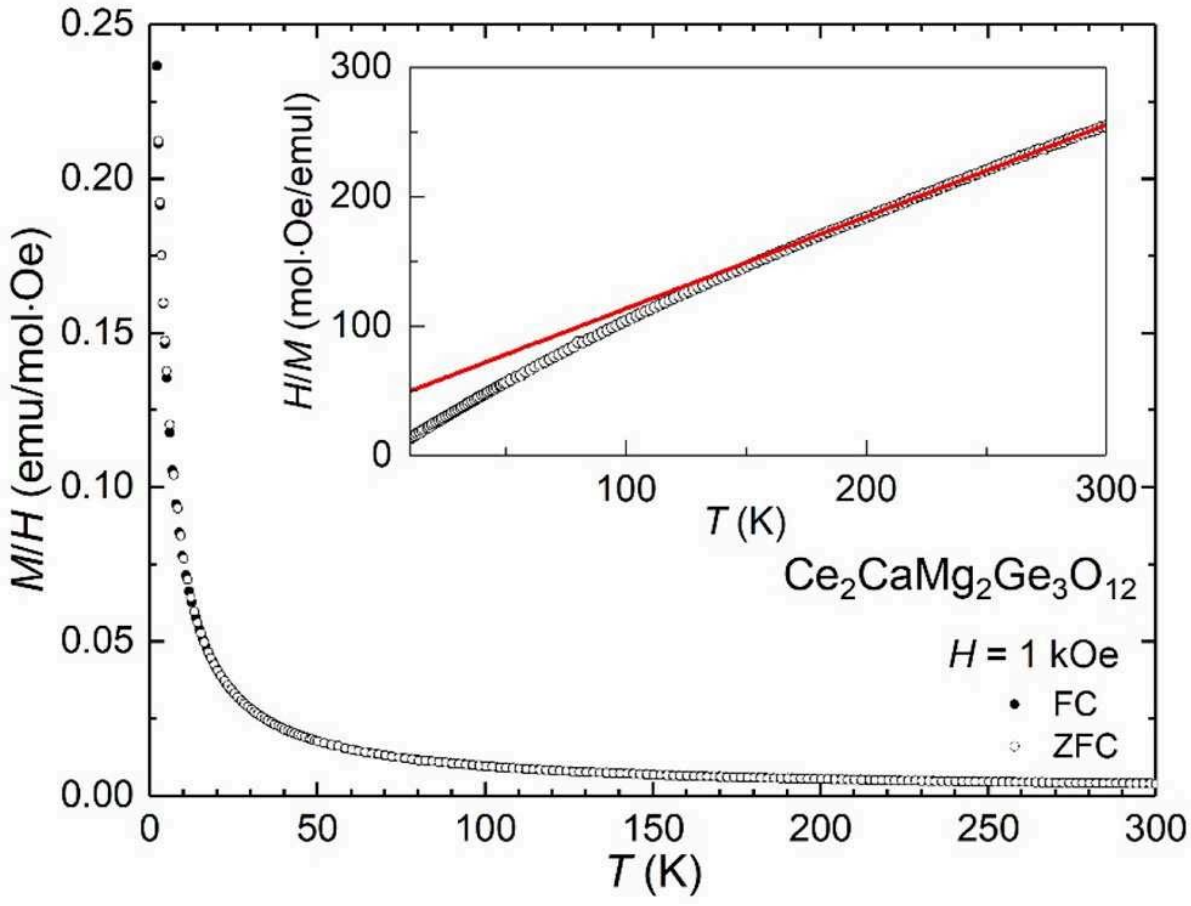

Figure 5.6. Magnetic susceptibility of $Ce_2CaMg_2Ge_3O_{12}$, measured in a magnetic field of 1

kOe. The inset shows its inverse χ vs. T plot. The red solid line is the fit to the Curie-Weiss law.

5.3.5. Theoretical Calculations.

Through the experimental analysis of the crystal structure of $Ce_2CaMg_2Ge_3O_{12}$, it was found that Ce and Ca ions occupy the A position of the structure of $A_3B_2C_3O_{12}$ garnet. In the first-principles calculation of structural models with periodic boundary conditions, the mixed occupation of atomic sites cannot be calculated directly. Therefore, in A fixed-size model of garnet structure, we have preliminatively identified the preferred distribution of Ce and Ca ions at site A in a 2:1 ratio. We chose the original unit cell of garnet structure as the basic model. The structural models of Ce and Ca with symmetric non-equivalent configurations are established. In the basic model using CLUPAN code,[44] a total of 20 independent configurations of Ce and Ca ions at site A were found. In the Brillouin region of the input structure model, the grid size of k-point sampling is 3 × 3 × 3. The total energy of the model calculated by structural optimization is compared.

From a series of calculations of the total energy of the $Ce_2CaMg_2Ge_3O_{12}$ model, we found that the most stable configuration is shown in Figure 5.7. We analyze the electronic structure of the model. Figure 5.8 shows the total state density (tDOS) and the projected partial density of states (pDOS) for each component. In Figure 5.8, the energy level at the top of the valence band is set to 0 eV on the horizontal axis. Positive and negative values on the vertical axis represent DOS for upper and lower spins, respectively. The tDOS values show that the calculated band gap is about 2.2 eV, which is in good agreement with the estimated band gap value of UV-VIS absorption spectrum. It is clear that there is a very sharp DOS spike at the highest energy level of the occupied state. Such sharp DOS peaks indicate that electron orbitals are highly localized. As can be seen from the pDOS values, these peaks originate from the 4*f* orbital of Ce^{3+} ions being occupied. DOS near the bottom of the conduction band appears to consist mainly of the 5*d* orbital of the Ce^{3+} ion and the 4*s* orbital of the Ge^{4+} ion.[45,46]

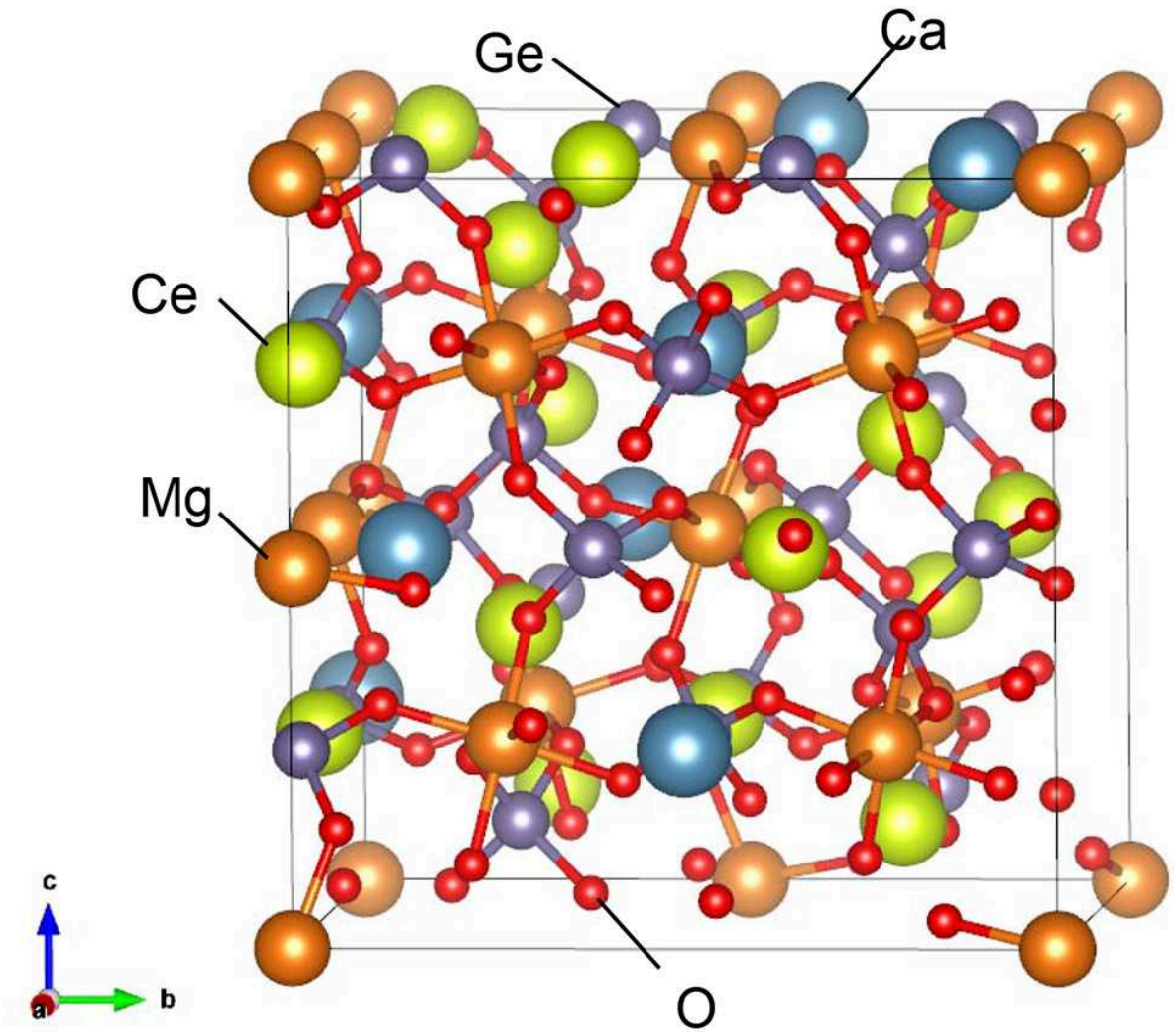

Figure 5.7. Most stable configurations of $Ce_2CaMg_2Ge_3O_{12}$ found by a series of first principles calculations in the present study. Search conditions are described in the main text.

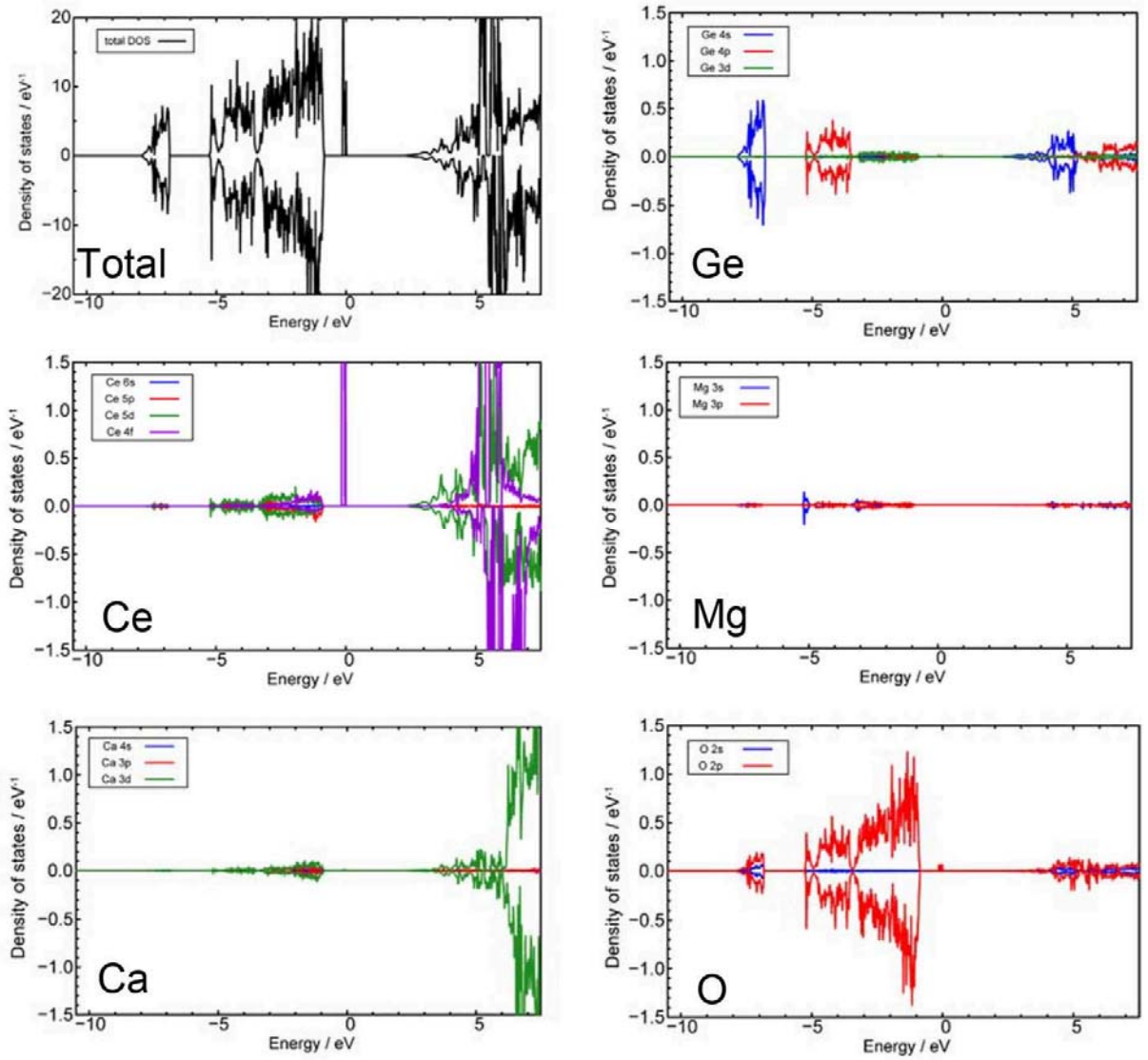

Figure 5.8. Total and projected partial density of states calculated from the model shown in Figure 5.7. The energy level of a valence band top is set to be 0 eV on the horizontal axes. Positive and negative values of the vertical axes indicate the DOS of up-spin and down-spin, respectively. Blue, red, green, and purple lines indicate the s, p, d, and f orbitals of each element, respectively.

5.4. Summary of Chapter 5

A new metastable germaniate garnet $Ce_2CaMg_2Ge_3O_{12}$was synthesized by flux crystal growth method. Red orange single crystal was grown in reactive MgO crucible. However, polycrystalline samples cannot be prepared by solid phase reaction. Flux reactions have clearly

helped to expand the garnet family to include elements of early lanthanide metals, especially those larger than Gd, which are less explored. PL intensity is too weak to be intuitively confirmed, which may be due to the quenching effect of the concentration of Ce^{3+} or photoionization involving charge transfer between Ce^{3+} and Ge^{4+}.

References in Chapter 5

1. Zhiguo, X., and Meijerink, A. Ce3+-doped garnet phosphors: composition modification, luminescence properties and applications. *Chem. Soc. Rev*. **2017**, 46, 275–299.
2. Bachmann, V. M., Ronda, C., and Meijerink, A. Temperature quenching of yellow Ce3+luminescence in YAG:Ce. *Chem. Mater*. **2009**, 21, 2077–2084.
3. Shao, Q., Dong, Y., Jiang, J., Liang, C., and He, J. Temperaturedependent photoluminescence properties of (Y, Lu)3Al5O12:Ce3+ phosphors for white LEDs applications. *J. Luminescence*. **2011**,131, 1013–1015.
4. Ueda, J., Dorenbos, P., Bos, A. J. J., Meijerink, A., and Tanabe, S. Insight into the thermal quenching mechanism for Y3Al5O12:Ce3+ through thermoluminescence excitation spectroscopy. *J.Phys. Chem. C*. **2015**, 119, 25003–25008.
5. Setlur, A. A., Heward, W. J., Gao, Y., Srivastava, A. M., Chandran, R. G., Shankar, M. V., et al. Crystal chemistry and luminescence of Ce3+-doped Lu2CaMg2(Si,Ge)3O12 and its use in LED based lighting. *Chem. Mater*. **2006**, 18, 3314–3322.
6. Muñoz-García, A. B., and Seijo, L. Structural, electronic, and spectroscopic effects of Ga codoping on Ce-doped yttrium aluminum garnet: first-principles study. *Phys. Rev. B*. **2010**, 82:184118.
7. Muñoz-García, A. B., Pascual, J. L., Barandiarán, Z., and Seijo, L. Structural effects and 4f−5dtransition shifts induced by La codoping in Cedoped yttriumaluminumgarnet: first-principles study. *Phys. Rev. B*. **2010**, 82:064114.
8. Geller, S. Crystal chemistry of the garnets. *Zeitschrift für Kristallographie - Crystalline*

Mater. **1967**, 125, 1–47.

9. Tauber, A., Banks, E., and Kedesdy, H. Synthesis of germanate garnets. *Acta Crystallogr*. **1958**, 11, 893–894.

10. Reinen, D. Die Lichtabsorption des Co2+ und Ni2+ in oxidischen Festkörpern mit Granatstruktur. *I. Zeitschrift für anorganische und allgemeine Chemie*. **1964**, 327, 238–252.

11. Lévy, D., and Barbier, J. Normal and inverse garnets: Ca3Fe2Ge3O12, Ca3Y2Ge3O12 and Mg3Y2Ge3O12. *Acta Crystallogr. Sect. C Cryst. Struct. Commun*. **1999**, 55, 1611–1614.

12. Garskaite, E., Sakirzanovas, S., Kareiva, A., Glaser, J., and Meyer, H.-J. Synthesis and structure of europium aluminium garnet (EAG). *Zeitschrift für anorganische und allgemeine Chemie*. **2007**, 633, 990–993.

13. Kasper, H.M. Series of rare earth garnets Ln3+3M2Li+3O12 (M=Te,W). *Inorgan. Chem*. **1969**, 8, 1000–1002.

14. Dukhovskaya, E. L., Saksonov, Y. G., and Titova, A. G. Oxygen parameters of certain compounds of the garnet structure. *Izvestiya Akademii Nauk SSSR Neorganicheskie Mater*. **1973**, 9, 809–813.

15. Komori, T., Sakakura, T., Takenaka, Y., Tanaka, K., and Okuda, T. (). Tripraseodymium penta-iron(III) dodeca-oxide, Pr3Fe5O12: a synchrotron radiation study. *Acta Crystallogr. Sect. E Struct. Rep. Online*. **2009**, 65:i73.

16. Komori, T., Sakakura, T., Takenaka, Y., Tanaka, K., and Okuda, T. Trineodymium(III) penta-iron(III) dodeca-oxide, Nd3Fe5O12. *Acta Crystallogr. Sect. E Struct. Rep. Online*. **2009**, 65:i72.

17. Guo, L., Huang, K., Chen, Y., Li, G., Yuan, L., Peng, W., et al. Mild hydrothermal synthesis and ferrimagnetism of Pr3Fe5O12 and Nd3Fe5O12 garnets. *J. Solid State Chem*. **2011**, 184, 1048–1053.

18. Malysa, B., Meijerink, A., and Jüstel, T. Temperature dependent Cr3+ photoluminescence in garnets of the type X3 Sc2 Ga3 O12 (X = Lu, Y, Gd, La). *J. Luminescence*. **2018**, 202:523–531.

19. Sawada, H. Electron density study of garnets:Z3Ga5O12;Z=Nd, Sm, Gd, Tb. *J. Solid State Chem*. **1997**, 132, 300–307.

20. Sawada, K., Nakamura, T., and Adachi, S. Europium gallium garnet (Eu3Ga5O12) and Eu3GaO6: synthesis and material properties. *J. Appl. Phys*. **2016**, 120:143102.

21. Awaka, J., Kijima, N., Hayakawa, H., and Akimoto, J. Synthesis and structure analysis of tetragonal Li7La3Zr2O12 with the garnet-related type structure. *J. Solid State Chem*. **2009**, 182, 2046–2052.

22. Murugan, R., Weppner, W., Schmid-Beurmann, P., and Thangadurai, V. Structure and lithium ion conductivity of garnet-like Li5La3Sb2O12 and Li6SrLa2Sb2O12. *Mater. Res. Bulletin*. **2008**, 43, 2579–2591.

23. Rongjin, J., Wenhui, Y., Caixiang, F., and Yanwei, Z. Glycothermal synthesis of heavily Ce-doped YIG nanocrystals and their microstructures and magnetic properties. *J. Mater. Chem. C*. **2013**, 1:1763.

24. Bugaris, D. E., and zur Loye, H. C. Materials discovery by flux crystal growth: quaternary and higher order oxides. *Angew. Chem. Int. Ed. Engl*. **2012**, 51, 3780–3811.

25. Bruker AXS Inc. APEX3 Version 2016.5-0 and SAINT+ Version 8.37A. Madison,WI: Bruker AXS Inc. **2016**.

26. Krause, L., Herbst-Irmer, R., Sheldrick, G. M., and Stalke, D. Comparison of silver and molybdenummicrofocus X-ray sources for single-crystal structure determination. *J. Appl. Crystallogr*. **2015**, 48, 3–10.

27. Sheldrick, G. M. SHELXT - integrated space-group and crystalstructure determination. *Acta Crystallogr. A Found Adv*. **2015**, 71, 3–8.

28. Hübschle, C. B., Sheldrick, G. M., and Dittrich, B. ShelXle: a Qt graphical user

interface for SHELXL. *J. Appl. Crystallogr*. **2011**, 44, 1281–1284.

29. Izumi, F., and Momma, K. Three-dimensional visualization in powder diffraction. *Solid State Phenomena*. **2007**, 130, 15–20.

30. Blöchl, P. E. Projector augmented-wave method. *Phys. Rev. B Condens. Matter*. **1994**, 50, 17953–17979.

31. Kresse, G., and Joubert, D. From ultrasoft pseudopotentials to the projector augmented-wave method. *Phys. Rev. B*. **1999**, 59, 1758–1775.

32. Kresse, G., and Hafner, J. Ab initio molecular dynamics for liquid metals. *Phys. Rev. B Condens. Matter*. **1993**, 47, 558–561.

33. Kresse, G., and Furthmüller, J. Efficient iterative schemes for ab initio total-energy calculations using a plane-wave basis set. *Phys. Rev. B Condens. Matter*. **1996**, 54, 11169–11186.

34. Kresse, G., and Furthmüller, J. Efficiency of ab-initio total energy calculations for metals and semiconductors using a plane-wave basis set. *Comput. Mater. Sci*. **1996**, 6, 15–50.

35. Perdew, J. P., Ruzsinszky, A., Csonka, G. I., Vydrov, O. A., Scuseria, G. E., Constantin, L. A., et al. Restoring the density-gradient expansion for exchange in solids and surfaces. *Phys. Rev. Lett*. **2008**, 100:136406.

36. Dudarev, S. L., Botton, G. A., Savrasov, S. Y., Humphreys, C., and Sutton, A. P. Electron-energy-loss spectra and the structural stability of nickel oxide: an LSDA+U study. *Phys. Rev. B*. **1998**, 57, 1505–1509.

37. Jiang, H., Rinke, P., and Scheffler, M. Electronic properties of lanthanide oxides from theGWperspective. *Phys. Rev. B*. **2012**, 86:125115.

38. Jiang, H., Gomez-Abal, R. I., Rinke, P., and Scheffler, M. Localized and itinerant states in lanthanide oxides united by GW @ LDA+U. Phys. Rev. Lett. **2009**, 102:126403.

39. Shannon, R. D. Revised effective ionic radii and systematic studies of interatomic

distances in halides and chalcogenides. *Acta Crystallogr. Sect. A*. **1976**, 32, 751–767.

40. Song, Z., Zhou, D., and Liu, Q. Tolerance factor and phase stability of the garnet structure. *Acta Crystallogr. C Struct. Chem*. **2019**, 75, 1353–1358.

41. Goldschmidt, V. M. Die gesetze der krystallochemie. Die Naturwissenschaften. **1926**, 14, 477–485.

42. Jiang, Z., Wang, Y., and Wang, L. Enhanced yellow-to-orange emission of Si-Doped Mg 3Y2Ge3O12:Ce3+ garnet phosphors for warm white lightemitting diodes. *J. Electrochem. Soc*. **2010**, 157:J155.

43. Wu, J. L., Gundiah, G., and Cheetham, A. K. Structure–property correlations in Ce-doped garnet phosphors for use in solid state lighting. *Chem. Phys. Lett*. **2007**, 441, 250–254.

44. Seko, A., Koyama, Y., and Tanaka, I. Cluster expansion method for multicomponent systems based on optimal selection of structures for density-functional theory calculations. *Phys. Rev. B*. **2009**, 80:165122.

45. Blasse, G., Schipper, W., and Hamelink, J. J. On the quenching of the luminescence of the trivalent cerium ion. *Inorganica Chimica Acta*. **1991**, 189, 77–80.

46. Pinelli, S., Bigotta, S., Toncelli, A., Tonelli, M., Cavalli, E., and Bovero, E. Study of the visible spectra of Ca3Sc2Ge3O12 garnet crystals doped with Ce3+ or Pr3+. *Optic. Mater*. **2004**, 25, 91–99.

Chapter 6. General conclusions and future prospects

6.1. General conclusions

In this thesis, two Ga/Ge-based oxysulfides with heteroleptic coordiantions and one Ge-based oxide with homoleptic coordiantion are investigated. The crystal structures, optical properties, and theoretical computations are discussed in detail.

Novel non-linear optical oxysulfide $La_3Ga_3Ge_2S_3O_{10}$ was obtained by flux growth method via a $BaCl_2$-NaCl molten salt. The crystal structure crystalizes in noncentrosymmetric space group *P*-62*c* with lattice constants *a* = 10.1701(4) Å and *c* = 7.5198(3) Å. $La_3Ga_3Ge_2S_3O_{10}$ possesses 1D $^1_\infty[(Ga_{3/5}Ge_{2/5})_3S_3O_3]$ triangular tubes and 0D $(Ga_{3/5}Ge_{2/5})_2O_7$ dimers in the structure forming both homoleptic and heteroleptic coordination environments around Ga/Ge, which contributes to the exceptionally wide band gap of 4.70 eV. SHG measurement reveals that it is phase-matchable with twice the SHG coefficient of KDP. The theoretical calculations suggest that the strong SHG intensity is mainly attributed to the existance of S-3*p* and O-2*p* orbitals.

New germanium oxysulfide single crystals $La_4(GeS_2O_2)_3$ were collected from a $BaCl_2$-$CaCl_2$ eutectic molten salt. Single-crystal structure analysis demonstrated the centrosymmetric space group *R*-3 with lattice constants *a* = 16.8283(3) Å and *c* = 8.4140(2) Å. It exhibits complex three-dimensional framework consisting of GeS_2O_2 tetrahedra linked with La-centered polyhedra through corneror edge-sharing. Moreover, the triangular arrangement of the GeS_2O_2 tetrahedra around a columnar structure of alternating facesharing LaO_{12} and LaS_6O_6 units resembles that of GeO_4 tetrahedra in the apatite germanate $La_{9.33}(GeO_4)_6O_2$, which features facesharing LaO_9 columns. The band gap of $La_4(GeS_2O_2)_3$ is 3.67 eV, which is consistent with first-principles calculations.

New metastable germanate garnet $Ce_2CaMg_2Ge_3O_{12}$ was obtained using a flux growth method from the $BaCl_2$-$CaCl_2$ eutectic melt. Truncated spherical, reddish-orange single crystals with a typical size of 0.1–0.3 mm were collected. $Ce_2CaMg_2Ge_3O_{12}$ crystallizes in a cubic garnet-type structure with a = 12.5487(3) Å in the space group $Ia\bar{3}d$. Based on the typical formula of garnet structure $A_3B_2C_3O_{12}$, Ce/Ca, Mg, and Ge occupy the A, B, and C sites, respectively. UV-vis spectroscopy reveals the band gap of 2.21 eV. Theoretical calculations indicate the contribution of Ce-4*f* and Ce-5*d* orbitals, which explains the absorption edge through the 4*f* to 5*d* absorption. PLE specta also exhibit a very broad peak centered at 600 nm, which proves the transition from the lowest energy *d* level to the 4*f* levels.

6.2. Future prospects

$La_3Ga_3Ge_2S_3O_{10}$ exhibits attractive SHG property in the UV region. The SHG intensity and cut-off edge blue-shift can be further enhanced by the utilization of other functional building block units, such as $[NO_3]^-$, $[CO_3]^{2-}$, and $[BO_3]^{3-}$ with π conjugated molecular configuration, instead of [Ga/GeQ$_4$]. However, the combination of chalcogenides and borates is not expected to form heteroleptic borate-chalcogenides, which usually yields to the thioborates or borate with homoleptic coordination environments. To the best of our knowledge, $Zn_4B_6O_{12}S$, $RE_6Ta_2MgQB_8O_{26}$ (RE = Sm, Eu, Gd; Q = S, Se), and $YSeBO_2$ have the special borate and chalcogenide structure.[1-3] Encouraged by the above advances, we have strong interests in developing novel chalcogenides combined with nitride, carbonate, and borate structure.

$La_3Ga_3Ge_2S_3O_{10}$ shows a disordered structure model at Ga and Ge sites. The influence of the order-disorder model to the optical property is not clear. The order-disorder transformation is commonly observed in rare earth compounds.[4] In order to find Ga and Ge site ordered compound, rare earth cation substitutions will be investigated. Lanthanum has no *f* orbital, the substitutions of other rare earth elements will introduce *f* electrons into the

structures will be focused.[5]

References in chapter 6

1. Wenfeng Zhou, Wen-Dong Yao, Ru-Ling Tang, Huaiguo Xue, and Sheng-PingGuo. Second-order nonlinear optical and photoelectric properties of Zn4B6O12S. *Journal of Alloys and Compounds*. **2021**, 867, 158879.
2. Zhi-Hui Shi, Yang Chi, Mei Yang, Wenlong Liu, and Sheng-Ping Guo. A Series of Chalcogenide Borates RE6Ta2MgQB8O26 (RE = Sm, Eu, Gd; Q = S, Se) Featuring a B4O10 Cluster. *Inorg. Chem*. **2020**, 59, 3532–3536.
3. Zhen-Tao Lu, Wen-Jing Fan, Zhi-Qian Wang, Ning Gu, Zeng-Hao Yue, Huai-Guo Xue, and Sheng-Ping Guo. Second-Order Nonlinear-Optical-Active Selenide Borate YSeBO2: Featuring a [YSeBO2]n Planar Belt. *Inorg. Chem*. **2020**, 59, 7905–7909.
4. S. C. Parida, S. K. Rakshit, and Ziley Singh. Heat capacities, order–disorder transitions, and thermodynamic properties of rare-earth orthoferrites and rare-earth iron garnets. *Journal of Solid State Chemistry*. **2008**, 181, 101–121.
5. Jin Chen, Chun-Li Hu, Fei-Fei Mao, Bing-Ping Yang, Xiao-Han Zhang, and Jiang-Gao Mao. REI5O14 (RE = Y and Gd): Promising SHG Materials Featuring the Semicircle-Shaped $I_5O_{14}^{3-}$ Polyiodate Anion. *Angew. Chem. Int. Ed*. **2019**, 58, 11666 –11669.

List of appended publications

This thesis is based on the following publications.

1. Scientific papers

1. **Hong Yan**, Yoshitaka Matsushita, Kazunari Yamaura, and Yoshihiro Tsujimoto. La3Ga3Ge2S3O10: A Novel Ultraviolet Nonlinear Optical Oxysulfide Designed by Anion-Directed Band Gap Engineering. *Angew. Chem*. **2021**. (DOI: 10.1002/anie.202112692).

2. **Hong Yan**, Yoshitaka Matsushita, Akira Chikamatsu, Tetsuya Hasegawa, Kazunari Yamaura, and Yoshihiro Tsujimoto. Flux Crystal Growth, Crystal Structure, and Magnetic Properties of a Ternary Chromium Disulfide Ba9Cr4S19 with Unusual Cr4S15 Tetramer Units. *ACS Omega*. **2021**, 6, 6842−6847.

3. **Hong Yan**, Akihide Kuwabara, Mark D. Smith, Kazunari Yamaura, Yoshihiro Tsujimoto, and Hans-Conrad zur Loye. Flux Crystal Growth, Structure, and Optical Properties of the New Germanium Oxysulfide La4(GeS2O2)3. *Crystal Growth & Design*. **2020**, 20, 4054-4061.

4. Jie Chen, **Hong Yan**, Akihide Kuwabara, Mark D. Smith, Yuki Iwasa, Hiraku Ogino, Yoshitaka Matsushita, Yoshihiro Tsujimoto, Kazunari Yamaura, and Hans-Conrad zur Loye. Flux Crystal Growth, Crystal Structure, and Optical Properties of New Germanate Garnet Ce2CaMg2Ge3O12. *Frontiers in Chemistry*. **2020**, 8, 91.

2. Verbal presentation

1. **Hong Yan**, Yoshihiro Tsujimoto, Hans-Conrad zur Loye and Kazunari Yamaura. Flux crystal growth approach toward non-centrosymmetric materials. The 11th nternational

Conference on the Science and Technology for Advanced Ceramics, Jul. 9-11, 2019, Tsukuba, Japan.

2. **Hong Yan**, Yoshihiro Tsujimoto, Hans-Conrad zur Loye and Kazunari Yamaura. Synthesis of new germanium-based oxysulfide compounds and optical properties. 29th Annual Meeting of MRS-J (2019), Nov. 27-29, 2019, Yokohama, Japan.

3. **Hong Yan**, Yoshihiro Tsujimoto, Hans-Conrad zur Loye and Kazunari Yamaura. La3Ga3Ge2S3O10 as a Possible Ultraviolet Nonlinear Optical Material. The 12th International Conference on the Science and Technology for Advanced Ceramics. Jul. 6-8, 2021, Online.

Acknowledgement

I would like to express my gratitude to all those who helped me during the PhD study. My deepest gratitude goes first and foremost to my supervisor, Professor Tsujimoto Yoshihiro, who has offered me valuable suggestions in the academic studies. During the past years，he has spent much time reading through each draft and provided me with inspiring advice. Without his patient instruction, insightful criticism and expert guidance, the completion of my PhD study would not have been possible.

Second, I would like to express my heartfelt gratitude to Professor Yamaura Kazunari, Professor Matsushita Yoshitaka, and Professor Alexei Belik for guidance on the experiment, especially in the structural analysis. I am also greatly indebted to Mrs. Sakai Etsuko for the academic and daily affairs. I would like to give my gratitude to Dr. Chen Jie, Dr. Liu ran, and Dr. Xing Lei for the help of lab-facilities and data process. I would like to thank Ms. Kang Xun, Mr. Hayashi Hiroaki, and Mr. Li Shaoxuan for their supports.

Last my thanks would go to my parents for their loving considerations and great confidence in me all through these years. None of this would have been possible with their support.